Engineering Journal

Smarter.
Stronger.
Steel.

Engineering Journal

American Institute of Steel Construction

Dedicated to the development and improvement of steel construction, through the interchange of ideas, experiences, and data.

The articles contained herein are not intended to represent official attitudes, recommendations or policies of the Institute. The Institute is not responsible for any statements made or opinions expressed by contributors to this Journal.

The opinions of the authors herein do not represent an official position of the Institute, and in every case the officially adopted publications of the Institute will control and supersede any suggestions or modifications contained in any articles herein.

The information presented herein is based on recognized engineering principles and is for general information only. While it is believed to be accurate, this information should not be applied to any specific application without competent professional examination and verification by a licensed professional engineer. Anyone making use of this information assumes all liability arising from such use.

Manuscripts are welcomed, but publication cannot be guaranteed. All manuscripts should be submitted in duplicate. Authors do not receive a remuneration. Guidelines for authors are printed on the inside back cover.

Buckling of Conventional and High-Strength Vanadium Steel Single- and Double-Angle Compression Members and Truss Subassemblies: Experimental and Computational Correlation Study

AHMET CITIPITIOGLU, MOHAMED M. TALAAT, RONALD L. MAYES, MARK D. WEBSTER,
and FRANK W. KAN

ABSTRACT

High-strength, low-alloy vanadium (HSLA-V) steel offers higher strength and toughness than conventional steel. The resulting lighter weight and more slender structural members are more susceptible to buckling in compression. This study establishes an understanding of buckling in this material and the ability to predict it analytically. A series of conventional ASTM A572 Grade 50 steel and HSLA-V (nominal Grade 80) steel angle compression members were tested at Lehigh University's Advanced Technology for Large Structural Systems (ATLSS) laboratory. A general-purpose finite element (FE) software was used in this study to simulate the buckling and post-buckling behavior of the structural members. The objective of these simulations was to establish confidence in the ability to accurately predict buckling response. The influence of the following modeling parameters on the accuracy of the compression angle member simulation results was investigated: variation in material stress-strain relationship, residual stresses, and the shape and magnitude of geometric imperfections. For the truss subassembly simulations, the influence of the following parameters was also investigated: bracing and boundary element stiffness and design code assumptions of end conditions.

Keywords: high-strength vanadium steel, compression, finite element analysis, buckling analysis, geometric imperfection, steel truss.

INTRODUCTION

Vanadium is a soft, ductile, silver-gray metal, similar in many properties to chromium. It is corrosion-resistant at normal temperature but oxidizes above 600°C. Vanadium is typically found combined with minerals. In the United States, the primary source of vanadium is spent catalyst from chemical processing plants. Recycling spent catalysts from oil refineries for vanadium reduces or eliminates the need for land-filling up to 6 million pounds of hazardous waste annually. It also reduces energy and waste requirements associated with processing virgin vanadium ores.

The principal use of vanadium is in metallic alloys, especially steels. In tool and spring steels, a small amount (less than 1%) adds strength, toughness, and heat resistance. Vanadium compounds are also used in the ceramics, glass, and dye industries and are important as catalysts in the chemical industry. Civil engineering applications include higher strength; lighter, and more ductile, structures, which offer special advantage to resistance of blasts or seismic shocks; as well as large-span and high-rise structures, which mainly support self-weight loads.

The experimental component of this study is based on a laboratory test program carried out in the Advanced Technology for Large Structural Systems (ATLSS) laboratory at Lehigh University. The detailed results of these experimental tests are documented in ATLSS Report No. 08-07, "An Experimental Study on Buckling of Vanadium Steel Members with Single- or Double-Angle Cross-Sections," (Candas et al., 2008). Single- and double-angle members were loaded under monotonic compression loading in the experimental program. The experimental program also included truss subassemblies fabricated using double-angle members and loaded under constant and gradient (moment-couple) loading, both monotonic and cyclic. The full report on this study is documented by Simpson, Gumpertz & Heger Inc. in SGH 2011. A follow-up study is documented in SGH 2012. In SGH 2011, the experimental results were compared to the design equations found in the 2010 AISC *Specifications*

Ahmet Citipitioglu, Director of Engineering and Design, TAV Construction, Istanbul, Turkey. Email: AhmetC@tavc.com.tr

Mohamed M. Talaat, Senior Project Manager, Simpson Gumpertz & Heger Inc., Oakland, Calif. Email: MTalaat@sgh.com (corresponding)

Ronald L. Mayes, Staff Consultant, Simpson Gumpertz & Heger Inc., Oakland, Calif. Email: RLMayes@sgh.com

Mark D. Webster, Senior Consulting Engineer, Simpson Gumpertz & Heger Inc., Waltham, Mass. Email: MDWebster@sgh.com

Frank W. Kan, Principal, Simpson Gumpertz & Heger Inc., Waltham, Mass. Email: FWKan@sgh.com

for Structural Steel Buildings, hereafter referred to as the AISC *Specification* (AISC, 2010), and the 2010 "Standard Specification" for open-web steel joists, published by SJI (2010). The purpose of the experimental program was to evaluate the buckling behavior of HSLA-V single- and double-angle members compared to conventional steel members. The research aimed to evaluate the ability to predict the correct failure mode and load capacity for a range of section element local slenderness (width-thickness ratios) and member slenderness (*L/r* ratios) and to evaluate the effects of end restraint and design assumptions (*K*-factors) on the overall buckling load of constructed subassemblies.

The analytical component of this study consists of FE simulations of experimental angle compression member tests. The objective of these simulations is to establish confidence in the ability to accurately predict buckling response, to investigate the sensitivity of the analytical simulations to a range of modeling and design assumptions, and to identify key modeling parameters and make corresponding recommendations for a subsequent analytical parametric study. Analysis sensitivity to the following parameters was investigated:

- Variability in material stress-strain relationships.

- Residual stresses.

- Magnitude of geometric imperfections.

- Superposition method to obtain initial imperfection shape.

- Member end restraint assumptions.

- Flexibility of boundary elements.

The following section presents a brief review of the treatment of compressive buckling in U.S. design codes.

TREATMENT OF BUCKLING IN U.S. DESIGN CODES

U.S. design codes use Euler's elastic column buckling equation as its basis to determine compression capacity. This equation is valid for slender members with pinned end conditions:

$$F_{e,i} = \frac{\pi^2 E}{(KL/r)_i^2} \quad \text{where} \quad i = x, y \quad (1)$$

where F_e is the theoretical elastic buckling stress, E is the material's modulus of elasticity, L is the length on the compression member, and r is the radius of gyration of the cross section. Subscript i reflects the two buckling axes: strong and weak axis.

Members with restrained end conditions typically result in higher buckling capacity. For members with differing boundary conditions, the member L/r ratio is modified by an effective length factor, also known as the *K*-factor to define the member slenderness (*KL/r*). The effective length is equal to the distance between inflection points in the compression member where the moment and curvature values are zero (i.e., between "pins") and the member curvature reverses direction. *K*-factors and corresponding effective lengths for various end conditions are shown in Figure 1.

If the compression member's cross-section elements (e.g., column flange, angle leg, etc.) are slender, local buckling of these elements may occur due to local instabilities before the overall member can buckle. Slenderness is related to both the width-to-thickness (*b/t*) ratio of the member cross-section elements (e.g., of the angle leg) and the material strength. This determines whether the section is a nonslender-element or a slender-element section. In nonslender-element sections, local buckling will occur long after the section has yielded; in slender-element sections, local buckling will occur before yielding and significantly reduce the compression member capacity. For members subject to flexure, sections are classified as compact, non-compact, or slender-element sections.

Members with Slender Elements

The AISC treatment of compression members with slender elements has changed with the 2016 AISC *Specification* (AISC, 2016). In previous AISC *Specifications*, the effect of element slenderness was accounted for according to the section geometry and considered to be independent of the stress level at which buckling occurs.

The 2010 AISC *Specification* defines a slenderness reduction factor, *Q*, that is introduced into the buckling equations as a multiplier to the material yield strength. The more slender the compression member cross-section elements (greater *b/t* ratio), the lower the *Q*-factor value, which typically ranges from 1.0 to 0.7. Figure 2 shows the slenderness reduction factor equations for angles. The current SJI Specification (SJI, 2020) uses the AISC 2010 *Specification* approach to determine the compressive buckling strength for members with slender elements.

The 2016 AISC *Specification* defines an effective area of the element cross section to account for element slenderness while calculating the member compressive strength. This effective area is based on the summation of the effective widths. For slender angle elements, the effective width for each leg is determined based on the width-to-thickness ratio, λ, with respect to the limiting width-to-thickness ratio, $λ_r$, which is defined as $λ_r = b/t = 0.45\sqrt{E/F_y}$ for

angles. Figure 3 shows the effective width equations for angles.

Flexural Buckling Strength

The member compression flexural buckling strength is calculated by determining the critical buckling stress. The change in the critical stress in relation to the member slenderness is shown in Figure 4. "Elastic buckling" occurs when slender compression members buckle at stresses lower than the material's elastic limit. It is characterized by the ability of the buckled compression member to regain its initial shape once the load is removed. On the other hand, "inelastic buckling" occurs when less slender members develop plastic deformations prior to reaching their buckling capacities. This results in unrecoverable permanent deformations.

The 2010 AISC *Specification* and the 2020 SJI Specification calculate the nominal compressive flexural buckling strength as follows:

$$P_n = F_{cr}A_g \tag{2}$$

The critical flexural buckling stress including slenderness effects, F_{cr}, is calculated as follows:

$$\text{when } \left(\frac{KL}{r}\right)_i \leq 4.71 \sqrt{\frac{E}{QF_y}} \quad \left(or \ \frac{QF_y}{F_e} \leq 2.25\right)$$

$$F_{cr} = \left(0.658^{\frac{QF_y}{F_{e,i}}}\right)QF_y \tag{3}$$

$$\text{when } \left(\frac{KL}{r}\right)_i > 4.71 \sqrt{\frac{E}{QF_y}} \quad \left(or \ \frac{QF_y}{F_e} > 2.25\right)$$

$$F_{cr} = 0.877F_{e,i} \tag{4}$$

where A_g is the section gross area, F_e is the theoretical elastic buckling stress given in Equation 1, Q is the slenderness reduction factor for compression members with slender cross-section elements shown in Figure 2, and $(KL/r)_i = 4.71\sqrt{E/QF_y}$ demarcates elastic and inelastic buckling.

The 2016 AISC *Specification* calculates the nominal compressive flexural buckling strength as follows:

$$P_n = F_{cr}A_e \tag{5}$$

The critical flexural buckling stress, F_{cr}, is calculated as follows:

$$\text{when } \left(\frac{KL}{r}\right)_i \leq 4.71 \sqrt{\frac{E}{F_y}} \quad \left(or \ \frac{F_y}{F_e} \leq 2.25\right)$$

$$F_{cr} = \left(0.658^{\frac{F_y}{F_{e,i}}}\right)F_y \tag{6}$$

$$\text{when } \left(\frac{KL}{r}\right)_i > 4.71 \sqrt{\frac{E}{F_y}} \quad \left(or \ \frac{F_y}{F_e} > 2.25\right)$$

$$F_{cr} = 0.877F_{e,i} \tag{7}$$

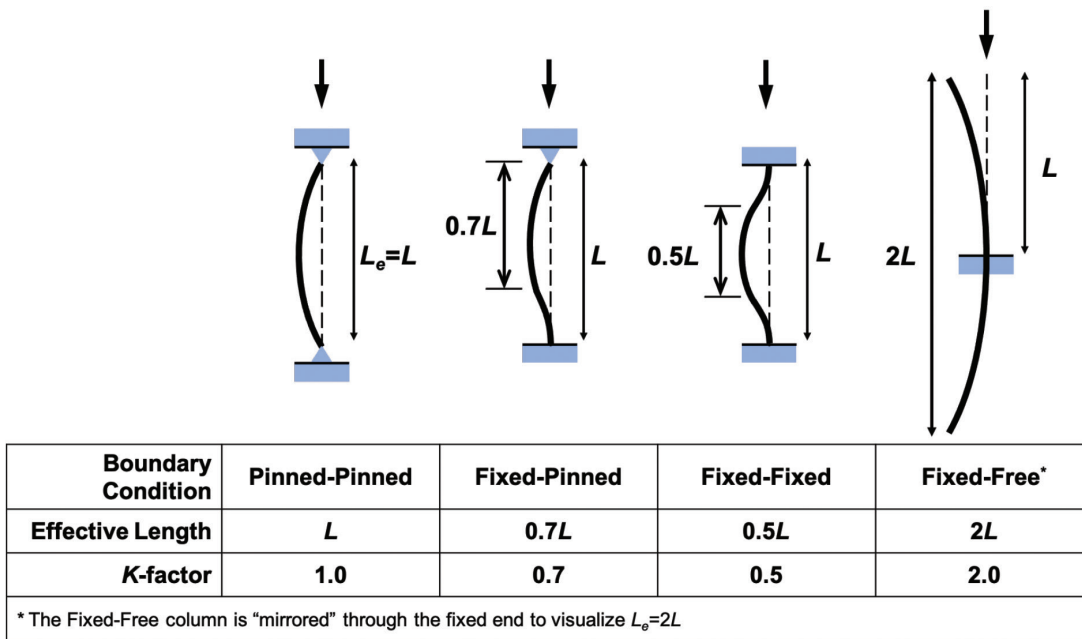| Boundary Condition	Pinned-Pinned	Fixed-Pinned	Fixed-Fixed	Fixed-Free*
Effective Length	L	0.7L	0.5L	2L
K-factor	1.0	0.7	0.5	2.0
* The Fixed-Free column is "mirrored" through the fixed end to visualize $L_e=2L$				

Fig. 1. Effective length factor, K*, for typical member end conditions.*

This is the same relation given in Equations 3 and 4 without the slenderness reduction factor, Q. The determination of the effective member cross section area, A_g, to account for slenderness is shown in Figure 3.

Built-Up Members

Compression strength of members built up from two or more shapes interconnected by bolted or welded elements are influenced by the stiffness and relative displacement of the connectors between the individual shapes forming the member. In both versions of the AISC *Specifications* (2010, 2016) and the 2020 SJI Specification, the slenderness ratio about the major axis is modified as follows for double angles:

when $a/r_i \leq 40$

$$\left(\frac{L_c}{r}\right)_m = \left(\frac{L_c}{r}\right)_y \tag{8}$$

when $a/r_i > 40$

$$\left(\frac{L_c}{r}\right)_m = \sqrt{\left(\frac{L_c}{r}\right)_y^2 + \left(\frac{0.5a}{r_i}\right)^2} \tag{9}$$

where a is distance between connectors along the length of the member and r_i is the minimum radius of gyration for a single angle. The definition of local axes in double-angle member cross sections is shown in Figure 5. The effective length of the built-up member, L_c, is equivalent to KL: the effective length factor, K, times the unbraced length, L. It
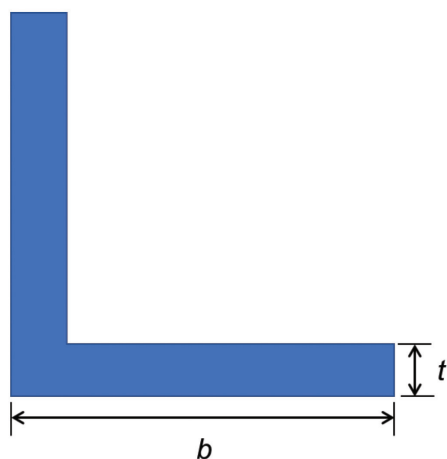
when $\dfrac{b}{t} \leq 0.45\sqrt{\dfrac{E}{F_y}}$

$$Q_s = 1.0$$

when $0.45\sqrt{\dfrac{E}{F_y}} < \dfrac{b}{t} \leq 0.91\sqrt{\dfrac{E}{F_y}}$

$$Q_s = 1.34 - 0.76\left(\frac{b}{t}\right)\sqrt{\frac{F_y}{E}}$$

when $\dfrac{b}{t} < 0.91\sqrt{\dfrac{E}{F_y}}$

$$Q_s = \frac{0.53E}{F_y(b/t)^2}$$

Fig. 2. Reduction factor, Q*, for angles per AISC* Specification *(2010).*
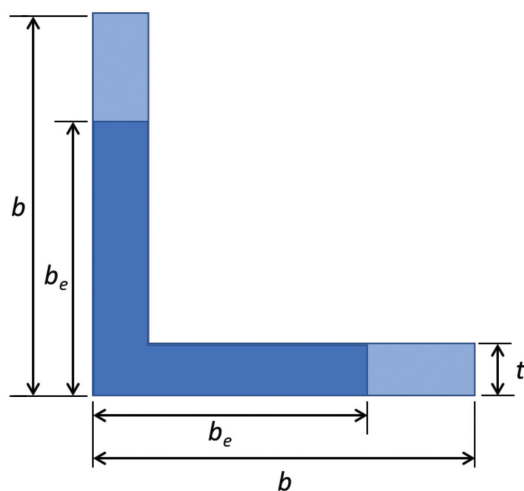
when $\lambda \leq \lambda_r\sqrt{\dfrac{F_y}{F_{cr}}}$

$$b_e = b$$

when $\lambda > \lambda_r\sqrt{\dfrac{F_y}{F_{cr}}}$

$$b_e = b\left(1 - c_1\sqrt{\frac{F_{el}}{F_{cr}}}\right)\sqrt{\frac{F_{el}}{F_{cr}}}$$

Fig. 3. Effective width, b$_e$*, for angles per AISC* Specification *(2016).*

is worth noting that the different modification factors given in the 2005 and 2010 AISC *Specifications* were evaluated in SGH (2011) and concluded that using either modification factor results in similarly better correlation with experimental results than not using either.

For built-up (i.e., double-angle) compression members, both versions of the AISC *Specification* (2010 and 2016) and of the SJI Specifications (2010 and 2020) apply the flexural buckling equation about both member axes, and the lower critical buckling stress governs the overall member strength. The AISC *Specifications* also consider the flexural-torsional buckling strength, which is not considered by the SJI Specifications.

Flexural Torsional Buckling Strength

The 2016 AISC *Specification* calculates the nominal compressive flexural-torsional buckling strength for double angles as follows:

$$P_n = F_{cr}A_e \tag{10}$$

where the critical stress, F_{cr}, is determined using Equations 6 and 7 with the elastic buckling stress, F_e, calculated using the following equations. The calculation of A_e is shown Figure 3.

$$F_e = \frac{F_{ey} + F_{ez}}{2H} \left[1 - \sqrt{1 - \frac{4F_{ey}F_{ez}H}{\left(F_{ey} + F_{ez}\right)^2}} \right] \tag{11}$$
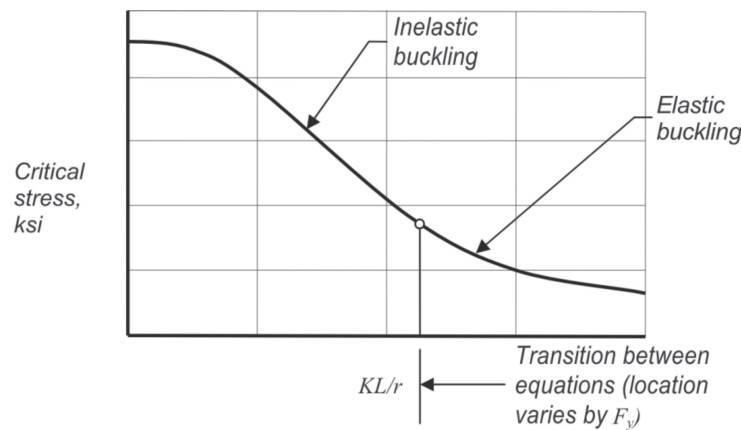

Fig. 4. Standard flexural buckling critical stress curve.
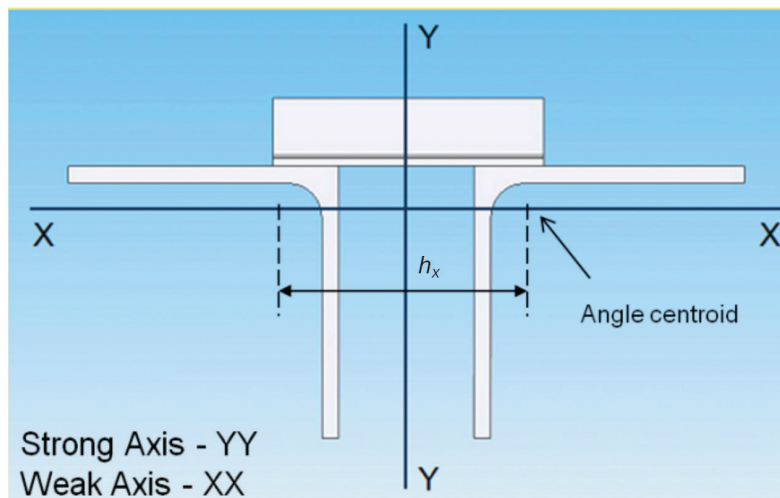
Fig. 5. Definition of local axes in double-angle member cross section.

$$F_{ez} = \frac{GJ}{A\overline{r}_o^2} \qquad (12)$$

$$H = 1 - \frac{x_o^2 + y_o^2}{\overline{r}_o^2} \qquad (13)$$

$$\overline{r}_o^2 = x_o^2 + y_o^2 + \frac{I_x + I_y}{A_g} \qquad (14)$$

$$J = \frac{At^3}{3} \qquad (15)$$

where F_{ey} is the elastic buckling stress about the strong axis (*y*-axis) calculated using Equation 1, including the modified member slenderness of Equations 8 and 9; J is the torsional moment of inertia; A is the double angle cross-sectional area; t is the angle leg thickness; G is the shear modulus of elasticity; x_o and y_o are the distances from the composite centroid to the angle shear center; and $\overline{r}_o$ is the polar radius of gyration about the double-angle section shear center.

Governing Buckling Strength

Due to the additional flexural-torsional buckling provisions mentioned previously, the AISC *Specifications* can result in more conservative estimates of buckling strength than the SJI Specifications. The nominal buckling load strength to member slenderness, L/r, curves calculated using both SJI (SJI, 2020) and the AISC *Specification* (AISC, 2016) are compared for double-angle cross section members with and without slender section elements in Figures 6 and 7, respectively. These curves are calculated for the member end conditions pinned about the strong axis and fixed about the weak axis and for the two angles connected by a single spacer element. The following buckling modes are calculated:

- Sum of the nominal buckling strength of the two individual single angles over the unbraced length between spacers, $P_{n-L\,flex\,z}$.

- Nominal double-angle flexural buckling strength about both weak and strong axis, $P_{n-LL\,flex\,x}$ and $P_{n-LL\,flex\,y}$.
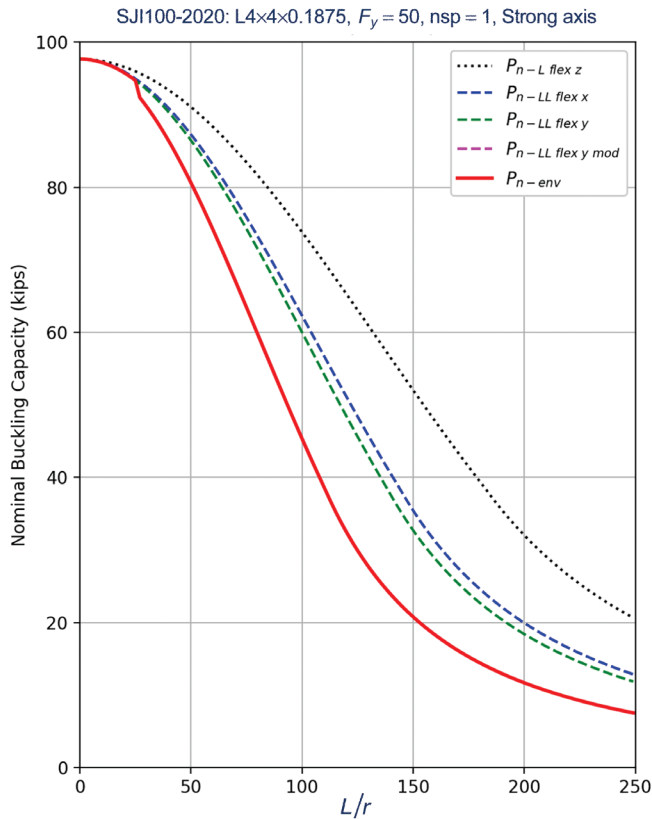
(a) 2020 SJI 100 (Q = 0.7)
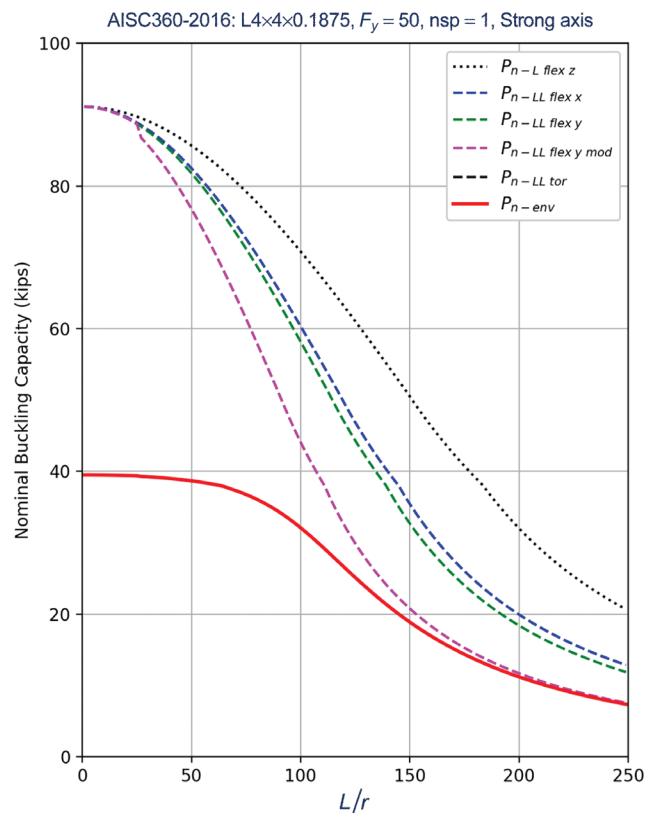
(b) AISC 2016 Specification (A_e = 0.62A to 0.95A)

Fig. 6. Example multi-mode nominal buckling strength curves for double-angle members with slender section elements.

- Nominal double-angle flexural buckling strength with the modified member slenderness ratio, which accounts for the influence of the connector between the angles, $P_{n-LL\ flex\ y\ mod}$. (The kink in the curve at low L/r values is due to the change in conditions that dictate using Equation 8 instead of Equation 9.)

- Nominal double-angle flexural-torsional buckling strength per the 2016 AISC *Specification* (AISC, 2016), $P_{n-LL\ tor}$.

The solid red line represents the lower-bound nominal strength envelope, P_{n-env}, of all the buckling modes listed.

Effect of Residue Stresses and Initial Imperfections

The critical buckling stress within the inelastic buckling range (Figure 4) is sensitive to residual stresses and initial imperfections. Galambos (1998) compares experimental tests and AISC critical load estimates for flexural buckling of I-shaped columns, which suggests that a larger spread of experimental results from the analytical prediction takes place in the inelastic buckling range. Adluri and Madugula

(1996) measured residual stress distributions in angle specimens, which reflect a wide dispersion within the cross section (Figure 8). Design equations typically account for the effects of residual stresses and initial imperfections empirically. In analytical studies, these effects need to be properly accounted for in the simulation models in order to obtain accurate results.

REVIEW OF EXPERIMENTAL PROGRAM

The analytical studies make use of a two-part experimental study: tests of individual compression single- and double-angle compression members and tests on truss subassemblies. The test programs are reviewed in the following sections.

Single- and Double-Angle Compression Member Tests

The size, length, nominal strength, compactness, slenderness ratios, and experimental buckling loads for the 6 single-angle compression test specimens are listed in Table 1. The same properties, with the addition of the

(a) 2020 SJI100 (Q = 1)
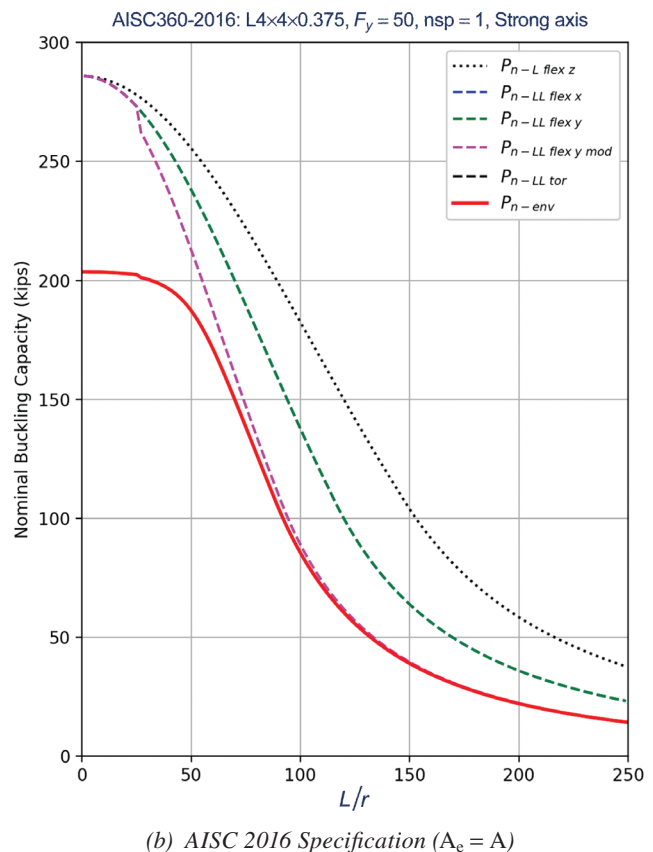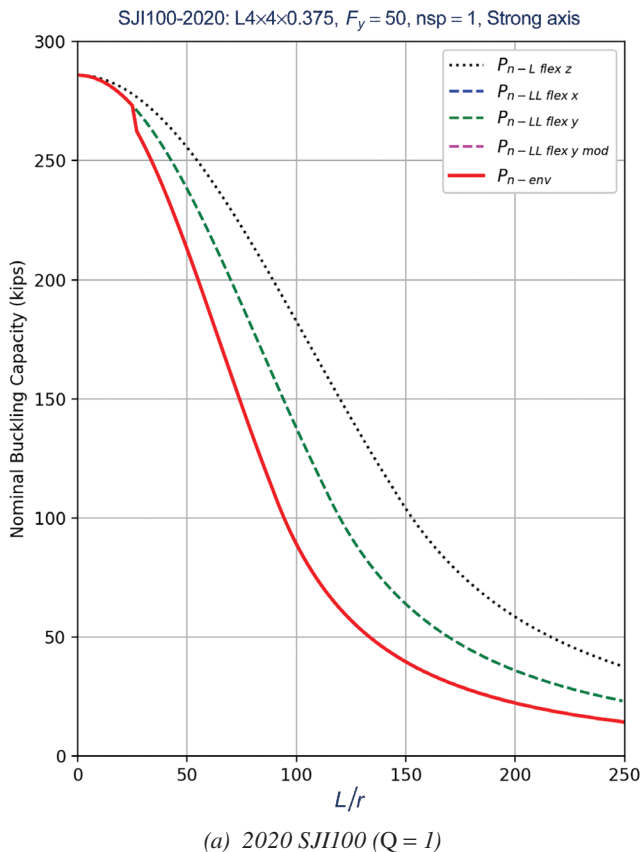
(b) AISC 2016 Specification (A_e = A)

Fig. 7. Example multi-mode nominal buckling strength curves for double-angle members without slender section elements. [Note that the two curves for $P_{n-LL\ flex\ x}$ and $P_{n-LL\ flex\ y}$ are overlapping in the plots as $(L_{cx}/r_x) = (L_{cy}/r_y)$ for this member section.]

Table 1. Single-Angle Test Variables						
Test No.	Size	Material	Length (in.)	Q	L/r	Buckling Load (kips)
SA1	L3.5×3.5×⅜	80 ksi	24	0.97	18	188
SA2	L3.5×3.5×⅜	80 ksi	50	0.97	44	162
SA3	L3.5×3.5×⅜	50 ksi	24	1.00	18	159
SB1	L3×3×³⁄₁₆	80 ksi	24	0.70	20	67.7
SB2	L3×3×³⁄₁₆	80 ksi	48	0.70	40	56.6
SB3	L3×3×³⁄₁₆	50 ksi	24	0.83	20	55.9

number of spacers, are listed for the 20 double-angle com-pression test specimens in Table 2.

Of the total of 26 compression specimens, 21 were fabri-cated using HSLA-V material, with a nominal 80-ksi yield stress, while the remaining 5 specimens were of Grade 50 steel material (test results for specimen DC5 were not reported). For all tests, the range of weak-axis member slenderness ratios, L/r, varied from 18 to 102, and slender-ness reduction factors, Q, ranged from 0.7 to 1.0. For the double-angle members tested, DA test series double angles were spaced 1 in. apart, while DB and DC test series double angles were spaced 1.5 in. apart. Spacers are used to control the flexural failure of a single angle prior to the flexural buckling strength of the member as a whole.

The test setup used cylindrical bearings, which allowed rotation about the strong axis while restraining rotation about the weak axis. Thus, the K-factor for weak-axis flex-ural buckling for all the test specimens is 0.5.

Tensile yield tests performed on coupons taken from the tested specimens show variabilities in the stress-strain response. Figure 9 shows plots of the individual coupon test results, for L3.5×3.5×⅜ angle size, and the best-fit curve used in the FE analyses.

The average measured out-of-straightness imperfection magnitude of the tested specimens was $L/1514$, where L is the nominal specimen length.

Truss Subassembly Tests

The truss subassembly tests performed at Lehigh (Candas et al., 2008) included two different types of tests: constant moment (CM) tests and gradient moment (GM) tests. Only the CM test setup, shown schematically in Figure 10(a), is addressed in this study. The CM test setup is intended to evaluate the performance near the truss midspan, where the bending moment is high and the shear is low. The speci-mens were loaded with a moment couple [Figure 10(b)].

(a) Sample distribution in cross section

(b) Measured and fitted values across angle leg
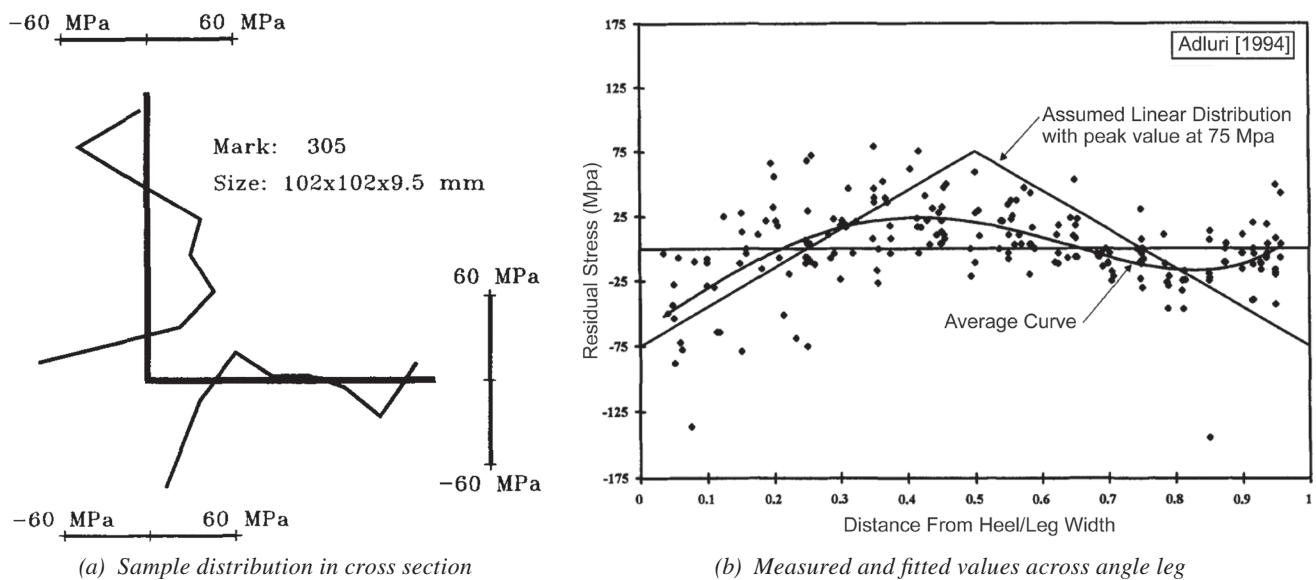
Fig. 8. Measurements and idealizations of residual stresses in steel angles (Adluri and Madugula, 1996).

Table 2. Double-Angle Test Variables							
Test No.	Size	Number of Spacers	Material	Length (in.)	Q	L/r	Buckling Load (kips)
DA1	LL3.5×3.5×⅜	2	80 ksi	30	0.970	28	361
DA12	LL3.5×3.5×⅜	2	80 ksi	30	0.970	28	360
DA2	LL3.5×3.5×⅜	2	80 ksi	48	0.970	45	344
DA22	LL3.5×3.5×⅜	2	80 ksi	48	0.970	45	362
DA3	LL3.5×3.5×⅜	2	80 ksi	66	0.970	61	342
DA4	LL3.5×3.5×⅜	2	80 ksi	84	0.970	78	339
DA42	LL3.5×3.5×⅜	2	80 ksi	84	0.970	78	301
DA5	LL3.5×3.5×⅜	2	50 ksi	48	1.00	45	314
DB1	LL3×3×³⁄₁₆	2	80 ksi	24	0.700	26	143
DB2	LL3×3×³⁄₁₆	2	80 ksi	48	0.700	51	127
DB3	LL3×3×³⁄₁₆	2	80 ksi	72	0.700	77	118
DB4	LL3×3×³⁄₁₆	2	80 ksi	96	0.700	102	86.2
DB5	LL3×3×³⁄₁₆	2	50 ksi	48	0.830	51	99.1
DC1	LL1.75×1.75×⅛	3	80 ksi	24	0.780	44	63.6
DC2	LL1.75×1.75×⅛	3	80 ksi	33	0.780	60	58.4
DC3	LL1.75×1.75×⅛	3	80 ksi	42	0.780	77	52.3
DC32	LL1.75×1.75×⅛	3	80 ksi	42	0.780	77	47.3
DC4	LL1.75×1.75×⅛	3	80 ksi	51	0.780	94	47.9
DC42	LL1.75×1.75×⅛	3	80 ksi	51	0.780	94	42.5
DC5[a]	LL1.75×1.75×⅛	3	50 ksi	24	0.900	44	NA
[a] Results not reported in Candas et al. (2008).							

Table 3. Truss Subassembly Member and Weld Sizes			
Member Type	Size	Yield/Ultimate Stress (ksi)	Web-to-Chord Fillet Weld (in.)
Chord	LL3.5×3.5×⅜	73.7/97.5	NA
Diagonal web	LL1.75×1.75×⅛	78.5/101	⅛ (⅛)
Vertical web	LL1×1×⅛	60.2/83.4	⅛ (⅛)
Vertical web at loaded end	LL2×2×³⁄₁₆	76.9/100	NA (³⁄₁₆)

The truss assemblies consisted of three panels each and were tested in a horizontal position. The panel points P3 and P5 were braced against truss out-of-plane buckling. The bracing detail is shown in Figure 10(c). The dominant failure mode of the CM specimens was buckling of the compression chord in the relatively longer middle panel. The three-dimensional displacement responses measured at the double-angle mid-spacers were recorded at working points P2, P4, and P6, as shown in Figure 10(a). Initial imperfections were not measured prior to testing.

Table 3 lists the truss subassembly member sizes and material strengths determined from coupon tests. Table 4 describes the differences between the truss specimen configurations. Specimens C1 through C3 were tested under a monotonic load application until the West chord buckled.

Specimens C4 and C5 were loaded in one direction until the West chord buckled (Phase 1), unloaded (Phase 2), and then subjected to a reversed load application until the East chord buckled (Phase 3). Phase 1 and Phase 3 loading refer to loading regimes causing buckling in the West and East chords, respectively.

Main Observations

The major experimental test findings reported in SGH 2011 are summarized as follows:

• The post-buckling deformed shapes of both individual single- and double-angle test specimens included both flexural and torsional modes, but it is not clear whether the buckling initiated as flexural-torsional or flexural
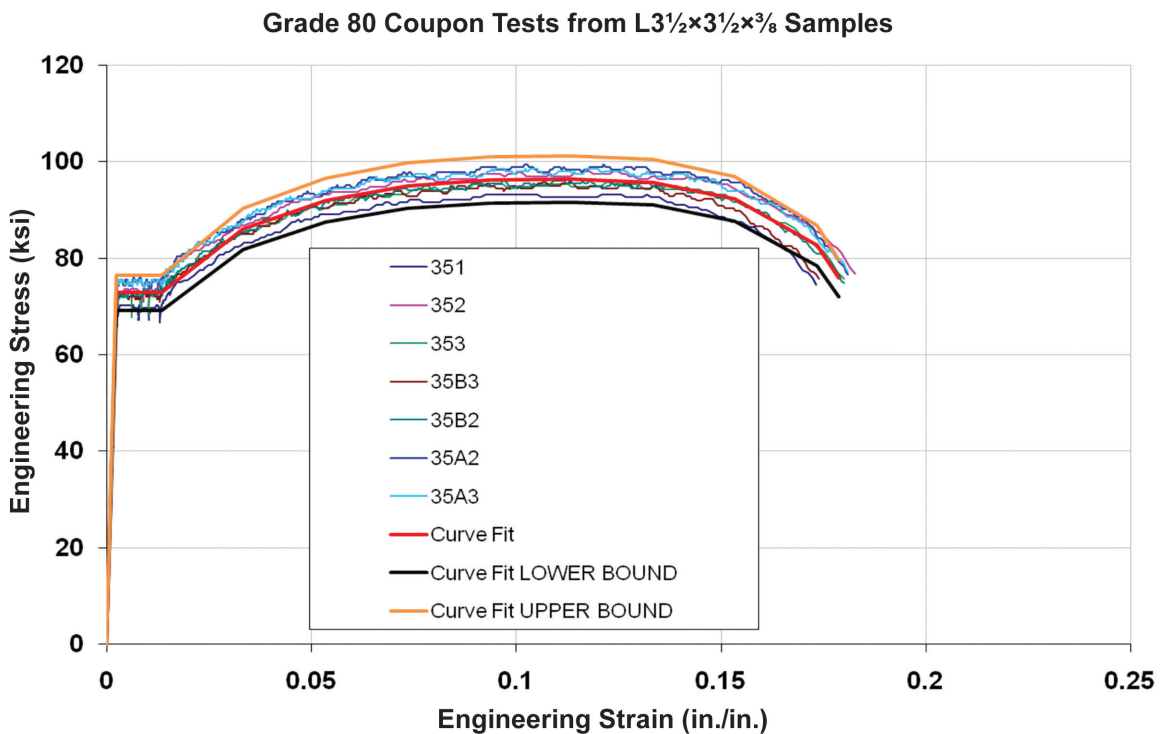
Fig. 9. Material stress-strain response from coupon tests compared to curve-fitted relationship used in FE analyses.

		Table 4. Truss Subassembly Specimen Information	
Spec.	Number of Spacers	Description	Observed Buckling Mode and Location
C1	3	Base case, designed per SJI procedures	Out of plane, Middle, and North panels
C2	3	Remove vertical web members to permit chord in-plane buckling	In-plane, North panel
C3	3	Use rotational restraints at panel points	Out of plane, Middle panel
C4	1	Use fewer chord-spacers	Out of plane, Middle panel
C5	5	Use more chord-spacers	Out of plane, Middle panel
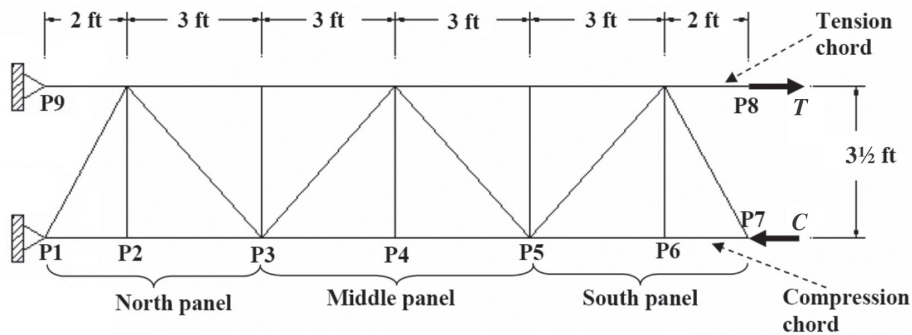
(a) Structural system and dimensions
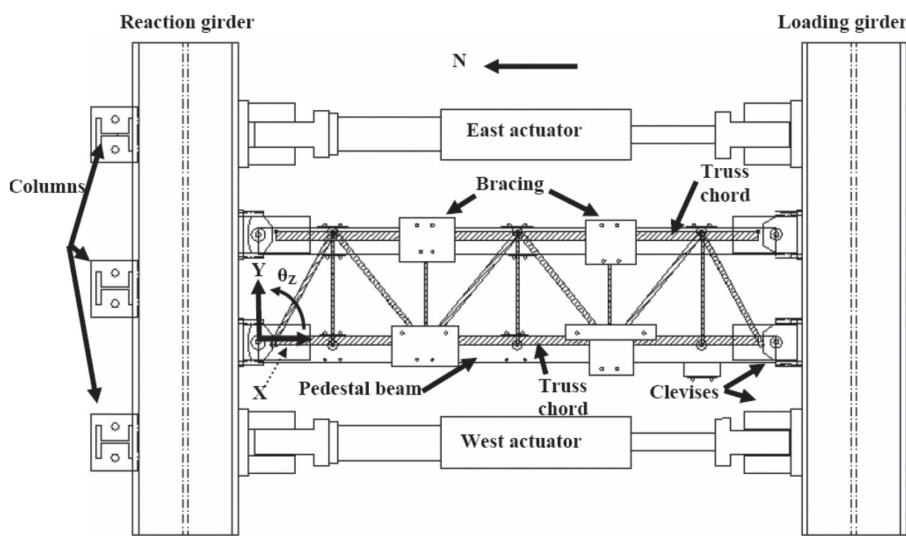
(b) Test setup
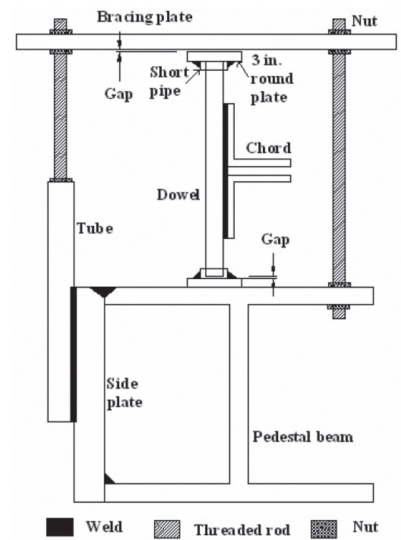
(c) Chord bracing detail

Fig. 10. Truss subassembly-constant moment (CM) test (Candas et al., 2008).

buckling. The measured capacities of the specimens were in closer agreement with the AISC-predicted flexural buckling strength about the strong axis (i.e., y-axis).

- The 2010 AISC *Specification* was significantly more conservative in predicting the strength of test specimens with smaller *Q*-values (more slender angle legs) than in predicting the strength of specimens with larger *Q*-values.

- The buckling strengths predicted using the 2010 AISC *Specification* were equally conservative for both the individual double-angle test specimens and the double-angle members in the truss subassemblies.

COMPUTATIONAL SIMULATION OF SINGLE- AND DOUBLE-ANGLE MEMBERS

FE Model Description and Analytical Sensitivity Study Matrix

The computational simulation software ABAQUS (2007) was used in this study. The FE models used four-node shell elements for the angle surfaces and eight-node continuum elements for bar spacers in modeling the double-angle specimens. A preliminary mesh sensitivity study concluded that the use of ~0.15-in. element size was sufficient to capture the displacement modes. The model boundary conditions reproduced those in the experimental setup. The load was applied by displacement control using the arc-length method (also called the Modified Riks algorithm) available in ABAQUS for loading regimes with geometrically unstable phases.

Sensitivity to Material Response

The modeling of the single- and double-angle specimens and investigation of sensitivity to modeling parameters was initiated by establishing a base-case geometry for each specimen. The base case was constructed using imperfections measured in the laboratory and interpolated by splines to create fitted surfaces along the specimen length. The best-fit material stress-strain curve shown in Figure 9 was used in the base-case analyses. (The stress-strain curve was converted to true stress-strain quantities to satisfy ABAQUS input requirements.)

The sensitivity to variability in the material stress-strain relationship was investigated by constructing two additional simulation cases for each specimen. These cases used the base-case geometry but adopted lower- and upper-bound stress-strain relationships obtained by multiplying the best-fit response by 0.95 and 1.05, respectively (Figure 9). The base-case simulation results compared to those using the

upper- and lower-bound material response curves are listed in Tables 5 and 9 for single and double angles, respectively.

Sensitivity to Initial Imperfection

The sensitivity to initial imperfection was investigated by constructing 12 additional simulation cases for each specimen. First, a geometrically perfect model was constructed from nominal geometry. An elastic buckling analysis was used to compute the buckling loads and shapes. Geometric imperfections were introduced by combining a number of buckling mode shapes that fall within a given multiple of the fundamental elastic load and scaling them so that the maximum imperfection magnitude meets a specified target. Example imperfect shapes are shown in Figure 11 for a short single-angle specimen and in Figure 12 for a slender double-angle specimen. The sensitivity study matrix included the following variables:

- Maximum imperfection magnitude: $L/500$ and $L/1500$. $L/1500$ is the assumption used in developing code equations. $L/500$ is used to investigate the effects of lower manufacturing quality control.

- Number of mode shapes to superimpose: modes within 2, 5, and 10 times the elastic buckling load, F_b.

- Combination of mode shapes: superimposed uniformly and inversely proportional to elastic buckling loads.

These results are listed in Tables 6 and 7 for single angles and Tables 10 and 11 for double angles.

Sensitivity to Residual Stress

The sensitivity to residual stresses was investigated by constructing six additional simulation cases for each specimen. An initial imperfection magnitude of $L/1500$, distributed using inversely proportional weights of mode shapes within twice the elastic buckling load was assigned to these six simulations. The number of shell element strips per angle leg was set to 20 in order to obtain a fixed resolution of the residual stress distribution. The residual stress was imposed as an initial load step. The sensitivity study matrix included the following variables:

- Maximum residual stress magnitude: $0.2F_y$ and $0.3F_y$.

- Residual stress profile: symmetric, half-symmetric, and asymmetric (Figure 13). These profiles are referred to in the results as "all," "half," and "v," respectively. These profiles are intended to bound the wide dispersion of data reported in (Adluri and Madugula, 1996).

These results are listed in Tables 8 and 12 for single and double angles, respectively.

Discussion of Results

The experimental and analytical initial stiffness, peak load, buckling mode, and post-buckling behavior were examined for each specimen. On average, the analytical initial stiffness was slightly higher than the experimental value. The analytical peak loads for the base cases (Tables 5 and 9) were higher for all L3½×3½×⅜ and L1¾×1¾×⅛ angle tests, and lower for most L3×3×³⁄₁₆ angle tests. The reasons for this pattern are not evident. The differences between analytical and experimental capacities were larger for specimens with higher slenderness. The analytical deformed shapes were in agreement with those observed in the laboratory tests, suggesting that the underlying mechanisms leading to buckling are captured. The analytical post-buckling behavior was generally in agreement with laboratory observations, although the softening curve exhibited a more sharply descending shape just after the peak load, which is common in such numerical simulations due to numerical localization of inelasticity and the absence of a physical loading mechanism (hydraulics, control, etc.) in the simulation. Figure 14 illustrates the comparison for specimen DA22.

Figure 15 shows the effect of analytically generated

*(a) 5*F$_b$ *(b) 10*F$_b$
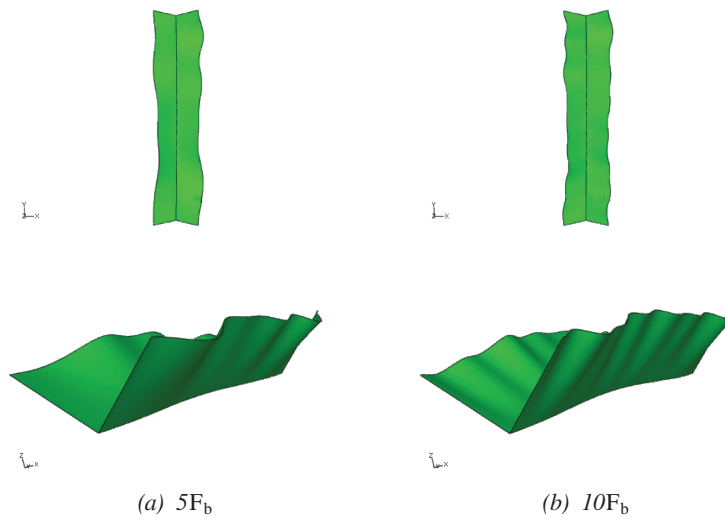
Fig. 11. Generated (magnified) geometric imperfection shapes of Specimen SA1 using uniform weights for modes within 5 and 10 times the elastic buckling load.

*(a) 5*Fb   *(b) 10*Fb
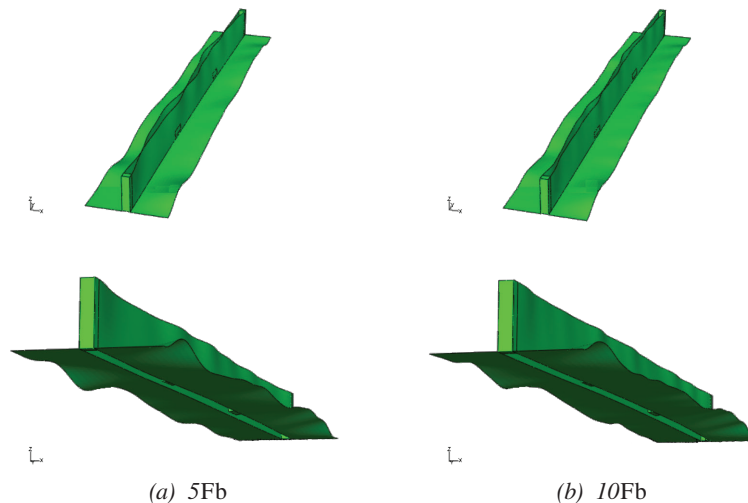
Fig. 12. Generated (magnified) geometric imperfection shapes of Specimen DA22 using inversely proportionate weights for modes within 5 and 10 times the elastic buckling load.

imperfections on the buckling response for specimen DA22. Comparing plots (a) and (b) suggests that the effect of the mode combination method is not significant for this specimen. In both plots, the base cases have analytical buckling loads (capacities) higher than the experimental values. The cases with analytically generated imperfections all have closer-matching capacities equal to or smaller than the experimental values. The sensitivity to the maximum imperfection magnitude and number of modes are within 5%.

Figure 16 shows the effect of residual stresses for specimen DA22. For this specimen, the cases with residual stress modeled all have closer-matching capacities equal to or smaller than the experimental values. The sensitivity to the different residual stress profile is small.

The analytical buckling loads from all simulations are summarized in Tables 5 to 8 (for single-angle specimens) and Tables 9 to 12 (for double-angle specimens). The following provides a summary of the analytical results:

• The ratio of analytical to experimental buckling loads for the single-angle base cases ranges from 0.86 to 1.11 (Table 5), with an average of 0.99. For double-angle specimens, the range is 0.90 to 1.17, with an average of 1.07 (Table 9).

| (a) Full symmetric [all] | (b) Half symmetric [half] | (c) Asymmetric [v] |
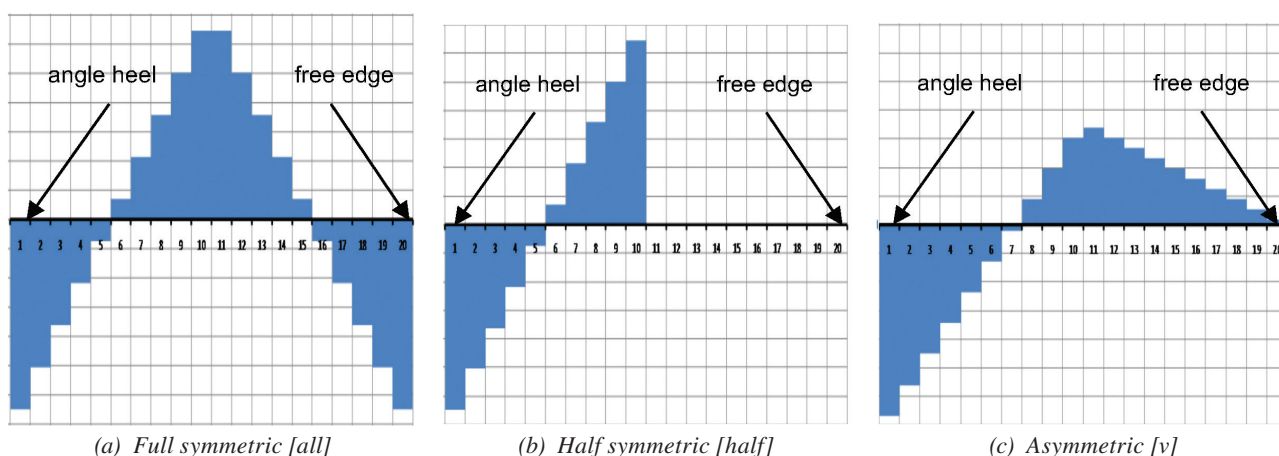
Fig. 13. Residual stress profiles across the angle leg. Vertical axis is the relative residual stress magnitude; positive residual stress is tension.

| (a) Experimental and analytical shape (showing von Mises stress) | (b) Load-displacement response (base case and stress-strain bounds) |
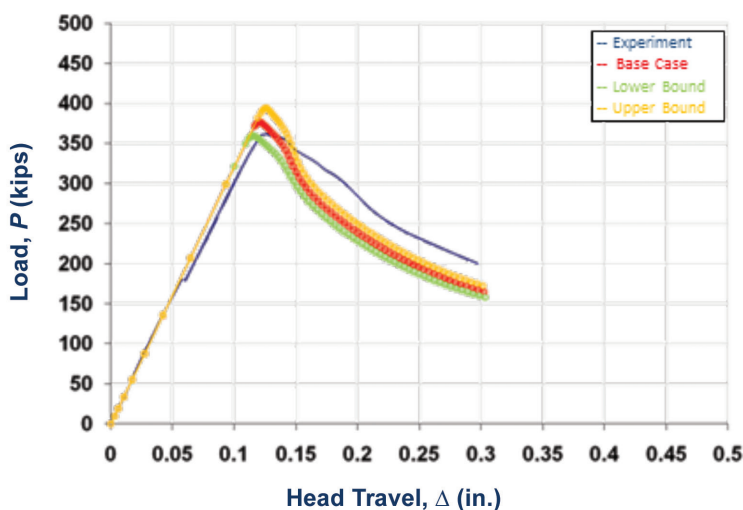
Fig. 14. Experimental and analytical behavior of specimen DA22.

- The sensitivity to stress-strain variability (Tables 5 and 9) is within 6% of the base case.

- The sensitivity to geometric imperfection magnitude increases with slenderness ratio. For single-angle specimens, the sensitivity to imperfection magnitude is higher for the more slender SB specimens than SA specimens (Tables 6 and 7). For double-angle specimens, the sensitivity is highest for the more slender DC specimens than it is for the less slender DB and DA specimens, respectively (Tables 10 and 11).

- Using geometric imperfection magnitudes of $L/1500$ shows better correlation, and agrees with laboratory measurements (Tables 6, 7, 10, and 11).

- Generating geometric imperfections using mode shapes within $2F_b$ and $L/500$ magnitude consistently underpredicts the strength (Tables 6, 7, 10, and 11). The use of $2F_b$ is not recommended.

- Comparing the corresponding ratios in Tables 6 and 7 (single angles) and in Tables 10 and 11 (double angles), the sensitivity to mode shape combination weighting method is within 4%, with smaller differences for imperfection magnitudes of $L/1500$.

- The sensitivity to increasing the number of mode shapes from within $5F_b$ to $10F_b$ is within 5% (Tables 6, 7, 10, and 11). This sensitivity is smaller when using inversely proportional weights, which may enable the use of fewer mode shapes with more reliability.
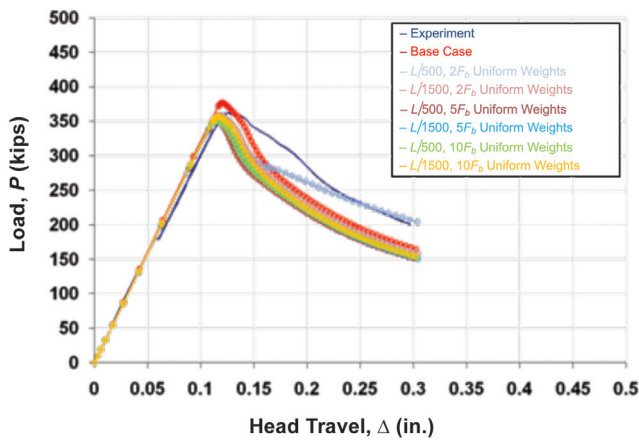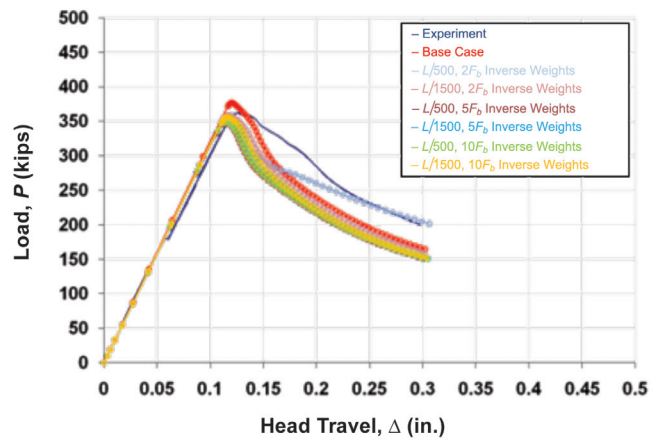
(a) Uniformly weighted mode shapes   (b) Inversely weighted mode shapes

Fig. 15. Effect of analytically generated imperfections on specimen DA22 buckling response.
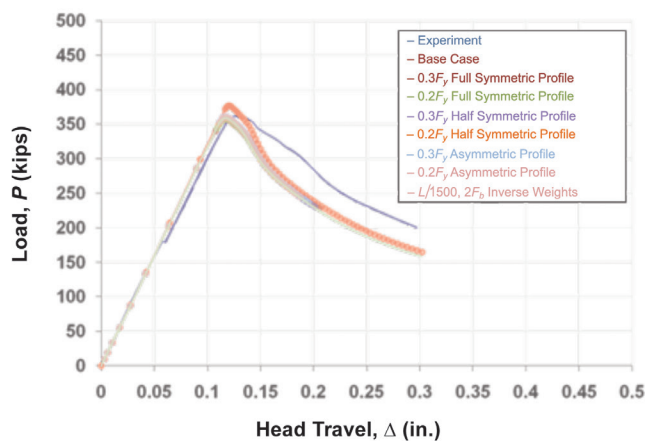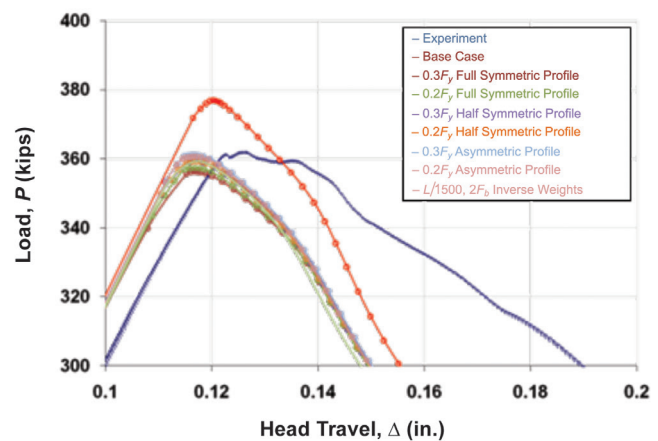
(a) Full response   (b) Close-up at peak response

Fig. 16. Effect of residual stresses on specimen DA22 buckling response.

Table 5. Analytical Single-Angle Buckling Strength and Effect of Stress-Strain Variability							
	Buckling Load (kips)						
Specimen ID	P_{exp}	Base P	P/P_{exp}	Upper-Bound P	P/P_{exp}	Lower-Bound P	P/P_{exp}
SA1	188	190	1.01	200	1.06	181	0.96
SA2	162	180	1.11	188	1.16	173	1.06
SA3	159	170	1.07	178	1.12	161	1.01
Mean for SA			1.06		1.11		1.01
SB1	67.7	62.2	0.92	63.3	0.94	61.3	0.91
SB4	56.6	48.9	0.86	49.2	0.87	48.6	0.86
SB5	55.9	54.6	0.98	54.9	0.98	54.2	0.97
Mean for SB			0.92		0.93		0.91
Overall mean			0.99		1.02		0.96

Table 6. Summary of Single-Angle Analytically Generated Geometric Imperfections with Uniform Weights												
Specimen	SA				SB				All			
	P_{case}/P_{base}				P_{case}/P_{base}				P_{case}/P_{base}			
Case[a,b]	Avg	Std	Max	Min	Avg	Std	Max	Min	Avg	Std	Max	Min
$5F_b, L/500$	0.99	0.01	0.99	0.98	0.96	0.03	0.99	0.94	0.98	0.02	0.99	0.94
$10F_b, L/500$	0.98	0.02	1.00	0.96	0.97	0.03	0.99	0.94	0.98	0.02	1.00	0.94
$5F_b, L/1500$	1.01	0.02	1.03	1.00	1.00	0.01	1.01	0.99	1.01	0.01	1.03	0.99
$10F_b, L/1500$	1.01	0.01	1.02	1.00	1.03	0.05	1.09	0.99	1.02	0.04	1.09	0.99
	P_{base}/P_{exp}				P_{base}/P_{exp}				P_{base}/P_{exp}			
	Avg	Std	Max	Min	Avg	Std	Max	Min	Avg	Std	Max	Min
Base case	1.06	0.05	1.11	1.01	0.92	0.06	0.98	0.86	0.99	0.09	1.11	0.86

[a] F_b refers to first-mode elastic buckling load based on perfect geometry.
[b] The $2F_b$ cases were not implemented for uniformly weighted mode shapes.

Table 7. Summary of Single-Angle Analytically Generated Geometric Imperfections Combined with Inverse Weights												
Specimen	SA				SB				All			
	P_{case}/P_{base}				P_{case}/P_{base}				P_{case}/P_{base}			
Case[a]	Avg	Std	Max	Min	Avg	Std	Max	Min	Avg	Std	Max	Min
$2F_b, L/500$	0.97	0.03	0.99	0.94	0.94	0.02	0.95	0.92	0.95	0.03	0.99	0.92
$5F_b, L/500$	0.98	0.02	0.99	0.96	0.96	0.02	0.98	0.94	0.97	0.02	0.99	0.94
$10F_b, L/500$	0.98	0.03	1.00	0.95	0.96	0.02	0.99	0.94	0.97	0.03	1.00	0.94
$2F_b, L/1500$	1.01	0.01	1.01	1.00	0.97	0.03	0.98	0.94	0.99	0.03	1.01	0.94
$5F_b, L/1500$	1.02	0.02	1.04	1.00	0.99	0.00	1.00	0.99	1.01	0.02	1.04	0.99
$10F_b, L/1500$	1.02	0.02	1.04	1.00	0.99	0.01	1.00	0.99	1.01	0.02	1.04	0.99
	P_{base}/P_{exp}				P_{base}/P_{exp}				P_{base}/P_{exp}			
	Avg	Std	Max	Min	Avg	Std	Max	Min	Avg	Std	Max	Min
Base case	1.06	0.05	1.11	1.01	0.92	0.06	0.98	0.86	0.99	0.09	1.11	0.86

[a] F_b refers to first-mode elastic buckling load based on perfect geometry.

Table 8. Summary of Single-Angle Effect of Residual Stresses												
Specimen	SA				SB				All			
	P_{case}/P_{cont}				P_{case}/P_{cont}				P_{case}/P_{cont}			
Case[a]	Avg	Std	Max	Min	Avg	Std	Max	Min	Avg	Std	Max	Min
Full symmetric $0.2F_y$	0.99	0.01	1.00	0.97	0.99	0.00	0.99	0.98	0.99	0.01	1.00	0.97
Full symmetric $0.3F_y$	0.98	0.02	1.00	0.95	0.98	0.01	0.98	0.97	0.98	0.02	1.00	0.95
Half symmetric $0.2F_y$	1.00	0.00	1.00	0.99	1.01	0.00	1.01	1.01	1.00	0.01	1.01	0.99
Half symmetric $0.3F_y$	0.99	0.01	1.00	0.97	1.00	0.02	1.02	0.98	1.00	0.02	1.02	0.97
Asymmetric (v) $0.2F_y$	1.00	0.00	1.00	0.99	1.02	0.01	1.03	1.02	1.01	0.01	1.03	0.99
Asymmetric (v) $0.3F_y$	0.99	0.01	1.00	0.98	1.03	0.01	1.04	1.02	1.01	0.02	1.04	0.98
	P_{cont}/P_{exp}				P_{cont}/P_{exp}				P_{cont}/P_{exp}			
	Avg	Std	Max	Min	Avg	Std	Max	Min	Avg	Std	Max	Min
Control case[b]	1.07	0.06	1.13	1.01	0.89	0.06	0.96	0.85	0.98	0.11	1.13	0.85

[a] Refer to Figure 13.
[b] Geometry set to inversely weighted mode shapes within twice the elastic buckling load with $L/1500$ imperfection magnitude.

Table 9. Analytical Double-Angle Buckling Strength and Effect of Stress-Strain Variability							
	Buckling Load (kips)						
Specimen ID	P_{exp}	Base P	P/P_{exp}	Upper-Bound P	P/P_{exp}	Lower-Bound P	P/P_{exp}
DA1	361	406	1.12	426	1.18	385	1.07
DA2	344	389	1.13	409	1.19	371	1.08
DA3	342	395	1.16	413	1.21	376	1.10
DA4	339	380	1.12	395	1.17	364	1.07
DA5	314	315	1.00	331	1.05	299	0.95
DA12	360	399	1.11	419	1.16	380	1.05
DA22	362	377	1.04	394	1.09	359	0.99
DA42	301	351	1.17	362	1.20	339	1.12
Mean for DA			1.11		1.16		1.05
DB1	143	138	0.96	140	0.98	135	0.94
DB2	127	114	0.90	116	0.91	113	0.89
DB3	118	113	0.96	113	0.96	112	0.95
DB4	86.2	90.1	1.05	90.1	1.05	90.1	1.05
DB5	99.1	100	1.01	101	1.02	99.2	1.00
Mean for DB			0.98		0.98		0.97
DC1	63.6	66.3	1.04	69.2	1.09	63.3	1.00
DC2	58.4	62.8	1.07	64.2	1.10	60.1	1.03
DC3	52.3	58.4	1.12	59.8	1.14	57.2	1.09
DC4	47.9	51.2	1.07	51.6	1.08	50.7	1.06
DC32	47.3	51.2	1.08	51.4	1.09	51.0	1.08
DC42	42.5	48.0	1.13	48.0	1.13	48.0	1.13
Mean for DC			1.19		1.11		1.07
Overall mean			1.07		1.09		1.03

Table 10. Summary of Double-Angle Analytically Generated Imperfections Combined with Uniform Weights

Specimen	DA				DB				DC				All			
	P_{case}/P_{base}				P_{case}/P_{base}				P_{case}/P_{base}				P_{case}/P_{base}			
Case[a]	Avg	Std	Max	Min	Avg	Std	Max	Min	Avg	Std	Max	Min	Avg	Std	Max	Min
$2F_b$, $L/500$	0.95	0.03	0.99	0.91	0.90	0.03	0.95	0.87	0.84	0.03	0.88	0.81	0.90	0.06	0.99	0.81
$5F_b$, $L/500$	0.95	0.04	1.00	0.87	0.95	0.03	0.99	0.92	0.91	0.02	0.96	0.89	0.94	0.04	1.00	0.87
$10F_b$, $L/500$	0.96	0.03	1.01	0.90	0.99	0.03	1.02	0.94	0.96	0.04	1.00	0.91	0.97	0.04	1.02	0.90
$2F_b$, $L/1500$	1.00	0.03	1.06	0.95	0.95	0.02	0.99	0.93	0.94	0.04	1.00	0.91	0.97	0.04	1.06	0.91
$5F_b$, $L/1500$	0.99	0.03	1.04	0.94	1.00	0.05	1.05	0.92	1.01	0.03	1.06	0.97	1.00	0.03	1.06	0.92
$10F_b$, $L/1500$	1.00	0.03	1.05	0.94	1.01	0.05	1.06	0.93	1.02	0.04	1.08	0.98	1.01	0.04	1.08	0.93
	P_{base}/P_{exp}				P_{base}/P_{exp}				P_{base}/P_{exp}				P_{base}/P_{exp}			
	Avg	Std	Max	Min	Avg	Std	Max	Min	Avg	Std	Max	Min	Avg	Std	Max	Min
Base case	1.11	0.06	1.17	1.00	0.97	0.06	1.05	0.90	1.09	0.03	1.13	1.04	1.07	0.07	1.17	0.90

[a] F_b refers to first-mode elastic buckling load based on perfect geometry.

Table 11. Summary of Double-Angle Analytically Generated Imperfections Combined with Inverse Weights

Specimen	DA				DB				DC				All			
	P_{case}/P_{base}				P_{case}/P_{base}				P_{case}/P_{base}				P_{case}/P_{base}			
Case[a]	Avg	Std	Max	Min	Avg	Std	Max	Min	Avg	Std	Max	Min	Avg	Std	Max	Min
$2F_b$, $L/500$	0.91	0.09	0.99	0.71	0.90	0.04	0.95	0.86	0.83	0.03	0.87	0.81	0.88	0.07	0.99	0.71
$5F_b$, $L/500$	0.95	0.04	0.99	0.86	0.95	0.05	1.00	0.90	0.88	0.03	0.92	0.85	0.93	0.05	1.00	0.85
$10F_b$, $L/500$	0.95	0.04	0.99	0.87	0.96	0.05	1.01	0.90	0.89	0.03	0.93	0.86	0.93	0.05	1.01	0.86
$2F_b$, $L/1500$	0.99	0.05	1.04	0.90	0.94	0.03	0.98	0.92	0.93	0.04	0.99	0.90	0.96	0.04	1.04	0.90
$5F_b$, $L/1500$	0.99	0.03	1.03	0.94	1.00	0.04	1.06	0.97	0.98	0.04	1.04	0.92	0.99	0.04	1.06	0.92
$10F_b$, $L/1500$	1.00	0.03	1.03	0.94	1.01	0.04	1.06	0.97	0.99	0.04	1.05	0.92	1.00	0.04	1.06	0.92
	P_{base}/P_{exp}				P_{base}/P_{exp}				P_{base}/P_{exp}				P_{base}/P_{exp}			
	Avg	Std	Max	Min	Avg	Std	Max	Min	Avg	Std	Max	Min	Avg	Std	Max	Min
Base case	1.11	0.06	1.17	1.00	0.97	0.06	1.05	0.90	1.09	0.03	1.13	1.04	1.07	0.07	1.17	0.90

[a] F_b refers to first-mode elastic buckling load based on perfect geometry.

Table 12. Summary of Double-Angle Effect of Residual Stresses

Specimen	DA				DB				DC				All			
	P_{case}/P_{cont}				P_{case}/P_{cont}				P_{case}/P_{cont}				P_{case}/P_{cont}			
Case[a]	Avg	Std	Max	Min	Avg	Std	Max	Min	Avg	Std	Max	Min	Avg	Std	Max	Min
Full symmetric $0.2F_y$	0.99	0.01	1.00	0.97	0.98	0.01	1.00	0.97	0.95	0.01	0.96	0.94	0.97	0.02	1.00	0.94
Full symmetric $0.3F_y$	0.98	0.02	1.00	0.95	0.98	0.01	0.99	0.96	0.94	0.01	0.96	0.92	0.97	0.02	1.00	0.92
Half symmetric $0.2F_y$	1.00	0.00	1.00	0.99	1.00	0.01	1.02	0.99	0.96	0.02	1.00	0.95	0.99	0.02	1.02	0.95
Half symmetric $0.3F_y$	1.00	0.01	1.00	0.99	1.00	0.01	1.01	0.99	0.96	0.02	1.00	0.95	0.99	0.02	1.01	0.95
Asymmetric (v) $0.2F_y$	1.00	0.00	1.01	1.00	1.02	0.01	1.04	1.00	0.97	0.03	1.02	0.91	1.00	0.03	1.04	0.91
Asymmetric (v) $0.3F_y$	1.00	0.01	1.01	1.00	1.01	0.01	1.03	1.00	0.97	0.02	1.01	0.96	1.00	0.02	1.03	0.96
	P_{cont}/P_{exp}				P_{cont}/P_{exp}				P_{cont}/P_{exp}				P_{cont}/P_{exp}			
	Avg	Std	Max	Min	Avg	Std	Max	Min	Avg	Std	Max	Min	Avg	Std	Max	Min
Control case[b]	1.09	0.09	1.22	0.97	0.92	0.06	0.99	0.85	1.01	0.05	1.07	0.96	1.02	0.10	1.22	0.85

[a] Refer to Figure 13.
[b] Geometry set to inversely weighted mode shapes within twice the elastic buckling load with $L/1500$ imperfection magnitude.

- The sensitivity to residual stress in Tables 8 and 12 is within 5% except for the DC series (9%), which has smallest cross-section size (LL1¾×1¾×⅛).

- The full symmetric residual stress profile consistently predicts buckling capacities lower than the control cases in Tables 8 and 12. The other two residual stress profiles predict buckling capacities both lower than and higher than the control cases.

COMPUTATIONAL SIMULATION OF TRUSS SUBASSEMBLIES

FE Model Description

Shell elements are used in the FE models to represent the steel angles used for the chords, the web, and the web spacers, as well as the end gusset plates [Figure 17(a)]. Welds were modeled using nodal degrees of freedom (DOF) constraints between elements along the weld length. The model used multipoint constraints to link the nodes in contact with the end clevises to a master node at the center of the hole in the corresponding gusset plates. A preliminary mesh sensitivity study considered mesh sizes of 4, 8, and 12 rows of quadrilateral shell elements per angle leg. The difference in estimated buckling loads was within 1% among the three cases. Hence, a typical mesh of four rows of elements per angle leg was used. Near joint locations, the chord member mesh was refined to eight rows of elements per leg. A linear DOF constraint was imposed between nodes along the transition line from four to eight element rows. Where diagonal and chord members intersected, an

irregular mesh of smaller element size was used to capture the stress and deformations occurring within the connection [Figure 17(b)].

An initial imperfection profile was assigned by superposing a number of buckling mode shapes as previously described, using uniform weights. The number of modes to include was selected to constitute a "complete set" whose buckling mode shape deformations are not biased toward any portion or panel(s) of the structure. Such a mode shape set is usually characterized by a noticeable shift in the elastic buckling load following the addition of a group of closely spaced buckling modes. Five values of maximum imperfection magnitudes were explored: 0.05, 0.075, 0.10, 0.20, and 0.40 in.

The loading sequence consisted of self-weight, followed by proportional loading at the end clevises up to the displacement level recorded in the laboratory. Specimens C4 and C5 were unloaded gradually, then proportionally loaded in the opposite direction. The Modified Riks algorithm was used in the analyses (ABAQUS, 2007). The base case analyses considered the stiffness of the loading girder and out-of-plane bracing to be effectively rigid. The sensitivity to this assumption was investigated, as discussed later.

For comparison of analytical and experimental behavior, the model in-plane and out-of-plane load-deflection responses and strain measurements were recorded at several points.

Discussion of Results

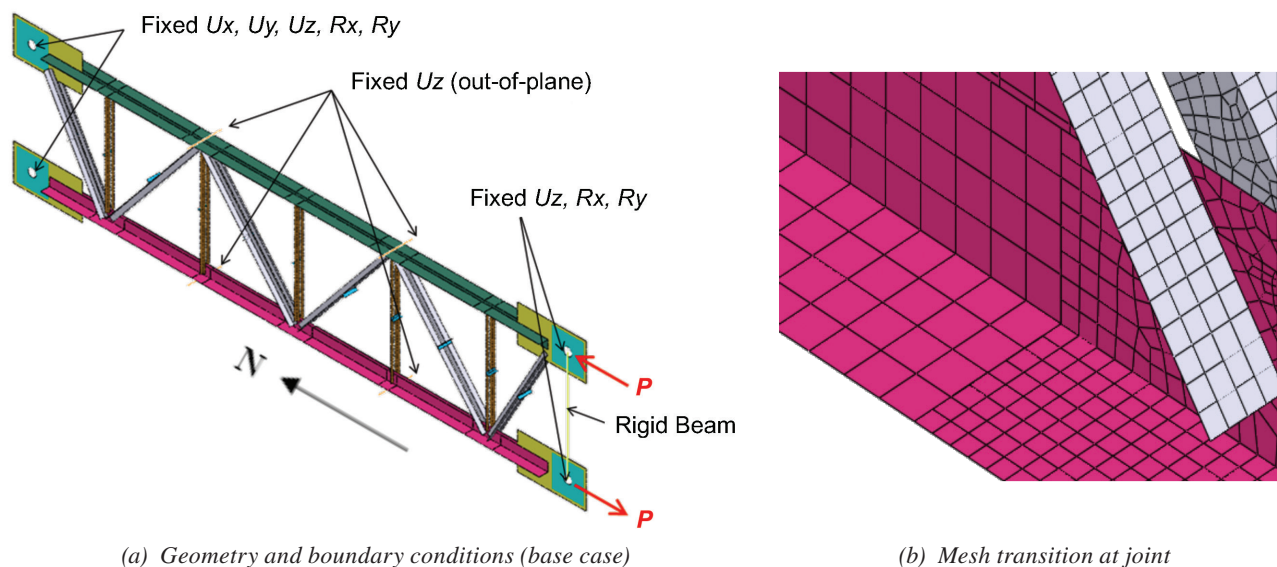The analytical load-displacement response is consistently stiffer than those observed in the laboratory experiments.

(a) Geometry and boundary conditions (base case)

(b) Mesh transition at joint

Fig. 17. ABAQUS FE model geometry and mesh for truss subassembly C4.

Table 13. Compression Chord Load Capacity for CM Base Cases (kips)						
		FE Simulations with Maximum Geometric Imperfection (in.)				
Specimen	Test	0.05	0.075	0.10	0.20	0.40
C1	308	347	344	342	330	305
C2	268	332	327	322	303	269
C3	350	350	347	346	337	316
C4, Phase 1[a]	332	346	343	339	329	302
C5, Phase 1[a]	341	351	349	347	336	304
C4, Phase 3[a]	334	344	340	336	314	277
C5, Phase 3[a]	347	350	349	347	332	299
[a] Phase 1 and Phase 3 refer to loading regimes causing buckling in the West and East chords, respectively.						

This is attributed to fit-up tolerances of the actuators and elimination of initial gaps in the test setup during early loading. Figure 18(a) shows the analytical load-displacement response at the center of the clevis attached to the West chord for specimen C1. The experimental load capacity is bounded by the analytical capacities for imperfection magnitudes of 0.20 and 0.40 in (about 1/1000 to 1/500 of the truss length). Figure 18(b) and Figure 18(c) compare the experimental and analytical deformed shapes, respectively (shown for 0.40-in. geometric imperfection magnitude, which resulted in the closest match with the experimental load capacity). The comparison indicates a similar deformed shape, although it is mirror-imaged to buckle in the South panel instead of the North panel (the specimen is symmetric). The following observations are summarized from all specimens:

- All FE simulations for Phase 1 result in primary buckling of the West chord taking place in the South panel; in some cases, the buckling zone extends to the Center panel. The FE component buckling modes are out-of-plane (strong axis) combined with local plate buckling, except for specimen C2, which, as expected, exhibits in-plane (weak-axis) buckling in the Center and South panels.

- The Phase 1 experimental tests resulted in primary buckling taking place in the Center panel, with members buckling locally and out of plane, except for two specimens: C1, where premature gusset plate rotation at the North clevis resulted in buckling initiating in the North panel before the Center panel, and C2, where the absence of vertical web members resulted in members buckling in-plane in the Center and South panels.

- The FE deformed shapes for Phase 3 have primary buckling at the East chord taking place in either the North panel (C4 specimen) or the South panel (C5 specimen), with buckling in both cases extending to the Center panel.

- The Phase 3 experimental test resulted in primary buckling in the Center panel of the East chord in both specimens C4 and C5.

The analytical maximum loads in the compression chord prior to buckling are compared to the test results in Table 13 for the range of maximum imperfections considered. The experimental load capacity is bounded by the FE simulation results, but the location of the buckling member is not always identical to the experiment. Except for specimen C3, all Phase 1 experimental load capacities fall within the bounds of the FE simulation results with 0.10- to 0.40-in. initial geometric imperfection magnitudes. The difference in analytical load capacity values between FE simulations of the different specimens increases with the magnitude of initial imperfection. In addition, the difference in load capacity from one specimen to another is larger in the experimental test results than in any of the FE simulations for any fixed value of assumed imperfection magnitude.

Sensitivity to Loading Girder Stiffness

The loading setup in the CM specimen tests (Figure 10) is such that the loading girder has to undergo significant motion at its connections to the actuators, including both translation and rotation, in order to transfer the imposed displacement pattern on the clevises attached to the specimen at points P7 and P8. The deformation in the loading girder was ignored in the base cases. Consideration for finite stiffness of the loading girder has two main effects on the analytical response:

- The flexural flexibility of the loading girder affects the overall flexibility of the system and in particular the flexibility associated with the in-plane rotation of truss panels and chord members.

- The torsional flexibility of the loading girder affects the elastic buckling loads and mode shapes, introducing
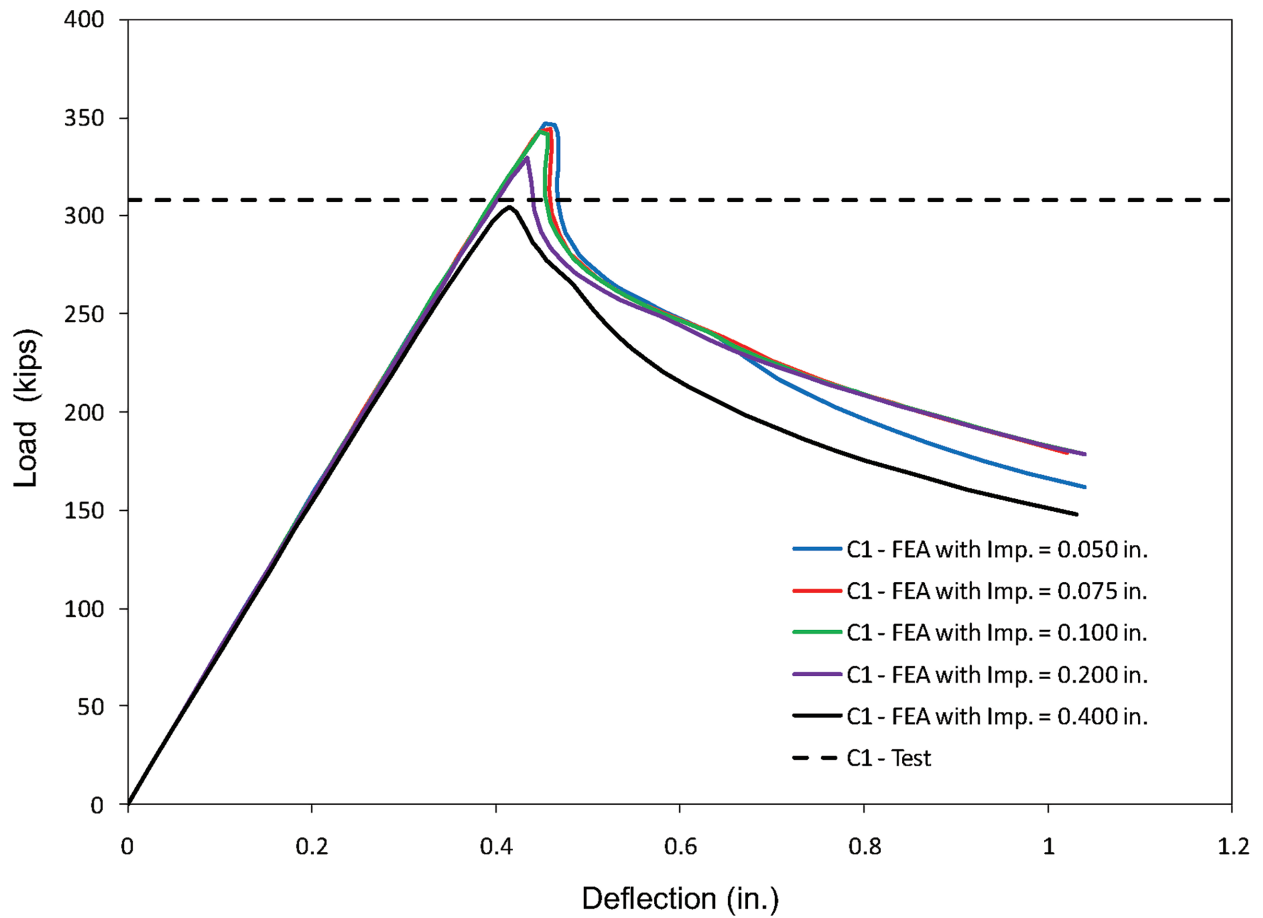
(a) Load-axial shortening
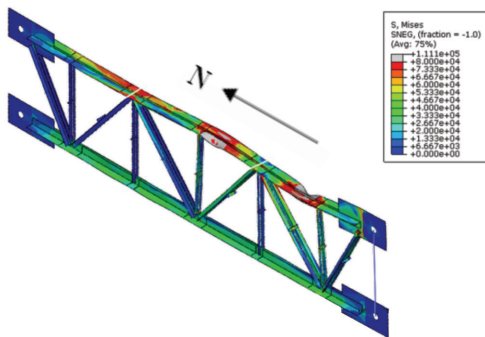
(b) FE simulation (0.40-in. imperfection)
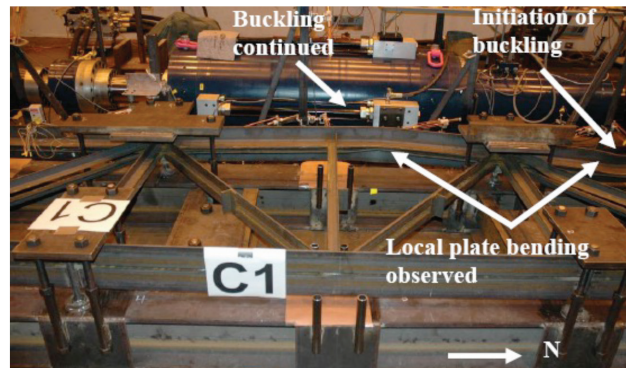
(c) Test photo (West chord up)

Fig. 18. Analytical and experimental behavior capacity for specimen C1.

two modes not previously observed with lower critical loads than the original first mode. These modes and the deformed shapes associated with their mode shapes when included in the calculation of initial geometric imperfection affect the initial geometry of the specimen in each simulation.

The behavior of the loading girder showed no evidence of nonlinearity throughout the experimental tests. Given the low span-to-depth ratio of the loading girder, six beam elements with shear-deformable (Timoshenko) formulation and a W30×326 cross section acting at the centerline of the loading girder were used between the actuator connection points, including two elements between P7 and P8. The boundary conditions are shown in Figure 19(a), where the out-of-plane translation of the loading girder at both ends and mid-span is restrained. The clevises were modeled using rigid offsets from the loading girder centerlines with allowance (release) for relative rotation at the clevis pin center. The modeled length of the loading girder is equal to the distance between the actuator axes. The loads at the ends of the loading girder were designated as follower loads so that they remain perpendicular to the girder. Only imperfection magnitudes of 0.10, 0.20, and 0.40 in. were considered.

Figure 19(b) shows the analytical deformed shape (with 0.4-in. initial geometric imperfection magnitude), which exhibits closer correlation to the experiment [Figure 18(c)] than the corresponding base-case simulation [Figure 18(b)]. Similar to the base case, the experimental load capacity is bounded by the analytical capacities for initial geometrical imperfection magnitudes of 0.20 and 0.40 in (Table 14). Including the loading girder stiffness in the FE models

resulted in better correlation with the experimental results because the simulations correctly predicted the deformed shapes and buckling initiation for all five specimens. The analytical and experimental maximum loads are listed in Table 14 for all specimens. Comparison with Table 13 leads to the following observations:

- The modeling of loading girder stiffness results in a slight reduction in the estimated monotonic load capacity (Phase 1 loading).

- Except for specimen C3, all Phase 1 experimental load capacities fall within the bounds of the FE simulation results with 0.1- to 0.4-in. initial geometric imperfection magnitudes.

- In the base cases, analytical load capacities of Phase 3 loading were always lower than those of Phase 1 loading. Upon modeling the loading girder stiffness, Phase 3 estimated load capacities were higher than Phase 1 for specimen C4 and lower for C5. In the experimental results, load capacities for Phase 3 were slightly higher than Phase 1 for both specimens.

Sensitivity to Out-of-Plane Bracing Stiffness

The out-of-plane bracing detail [Figure 10(c)] included initial gaps between the welded dowel and the bracing plates at each end, estimated at ⅛ in. combined between top and bottom sides. Under laboratory conditions, the self-weight and erection loads can close the initial gap on the lower side and increase the gap on the upper side. During loading, after contact between the welded dowel and the bracing system, the out-of-plane stiffness of the bracing system at
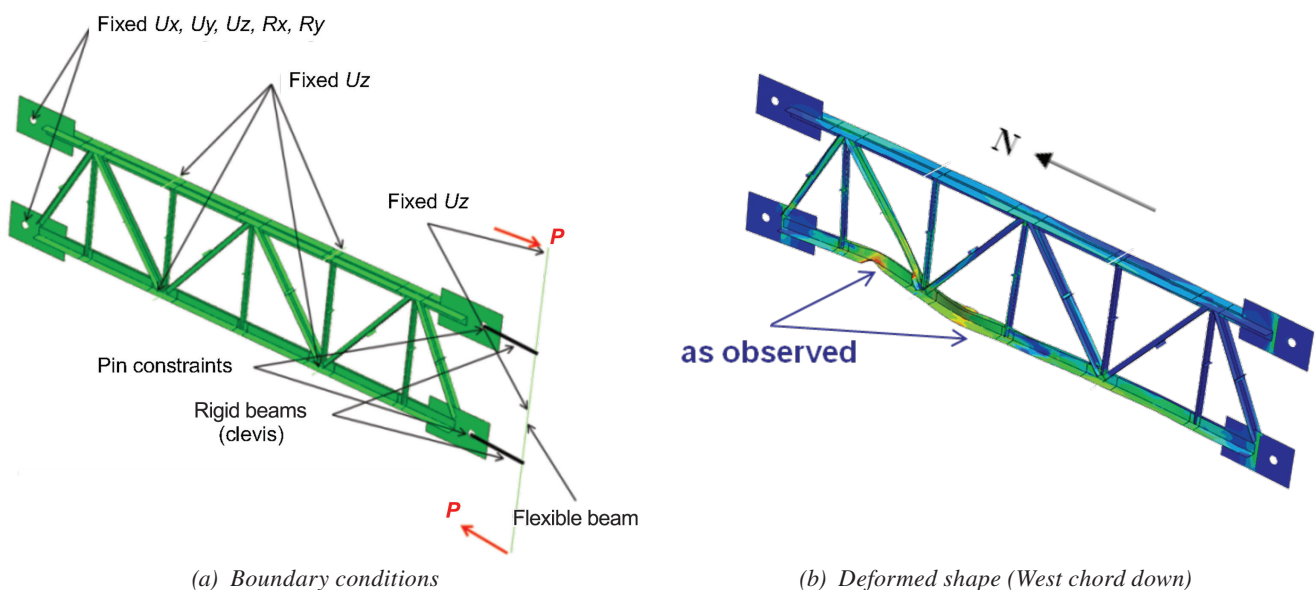

(a) Boundary conditions

(b) Deformed shape (West chord down)

Fig. 19. FE model and results for specimen C1 with flexible loading girder.

Table 14. Compression Chord Load Capacity for CM Flexible Girder Cases (kips)						
		FE Simulations with Maximum Geometric Imperfection (in.)				
Specimen	Test	0.05	0.075	0.10	0.20	0.40
C1	308	NA	NA	335	321	291
C2	268	NA	NA	312	292	254
C3	350	NA	NA	338	323	296
C4–Phase 1	332	NA	NA	336	324	305
C5–Phase 1	341	NA	NA	343	335	316
C4–Phase 3	334	NA	NA	337	339	328
C5–Phase 3	347	NA	NA	340	332	312

the ends of the welded dowel is not symmetric. On the bottom side, the stiffness can be considered relatively infinite due to bearing on the pedestal beam, which, in turn, bears on the lab floor. On the top side, the stiffness is finite and can be derived as a series system composed of bending in the bracing plate and elongation in the four threaded rods. The plate bending stiffness was evaluated numerically as 1,430 kips/in., representative of a 20×6×1½ in. plate when loaded by a concentrated transverse load and supported at its four corners per the experimental setup. Threaded rod axial stiffness was calculated as 1,790 kips/in. The equivalent series system has a stiffness of 1,190 kips/in. for the bracing assembly. Nonlinear gap and contact elements were defined accordingly to simulate this bounding condition at the bracings.

The simulation of out-of-plane bracing stiffness included assigning the initial ⅛-in. gap as either split between top and bottom sides or all to the top side, in conjunction with multiple contact algorithms and solution control options. It was concluded that the inclusion of out-of-plane bracing stiffness did not significantly affect the analytical buckling load and yet had a significant negative effect on the solution time and numerical stability due to the contact iterations.

Evaluation of Code Design Specifications

The AISC and SJI Specification equations for truss or joist member buckling are based on assumed end conditions for chord and web members and correspondingly assigned K-factors. In addition, the two Specification provisions provide no modification of the design loads to account for connection eccentricity in single-angle and double-angle member ends if the weld and member geometric centers do not coincide. For each subassembly specimen, the compression member strengths observed in the experiments (and determined using the FE simulations) were consistently higher than the ultimate strengths calculated using the Specification equations. This observation suggests that the effect of end conditions on the member behavior introduces

more rotational fixity than is accounted for by the Specification equations. In other words, the experimental behavior corresponds to lower K-factors than the design equations specify, which result in a conservative design in these cases.

In order to evaluate this effect, Table 15 compares the experimental and Specification chord member buckling loads and computes the equivalent K-factor values, which correspond to the experimental buckling load. Chord member forces were calculated from the actuator forces using free-body equilibrium and linear geometric transformation. Chord member buckling lengths were defined between the panel working points. With the exception of specimens C1 (which experiences an unanticipated rotation in the gusset plate resulting in premature end-panel failure) and C2 (which experienced weak-axis buckling due to the absence of vertical web members), all the equivalent K-factors fall in the range 0.5 to 0.65. Table 15 is computed by assigning the appropriate K-factor using the 2010 SJI Specification based on the critical member bucking mode, end conditions, location, and structural role within the truss subassembly.

SUMMARY

This study presents a procedure for analytically simulating the buckling behavior of single- and double-angle compression members and truss subassemblies and the performance of this procedure in comparison to experimental data. The members and subassemblies used in the experimental testing program were designed by the authors and the tests were performed at Lehigh University.

The single- and double-angle compression member correlation study was performed using FE simulations of 6 single-angle and 19 double-angle monotonic compression tests exhibiting buckling failure. For each specimen, the simulation consisted of a reference base case and an analytical sensitivity study matrix. The base case used measured angle dimensions and best-fit material properties from coupon tensile test results. The analytical sensitivity matrix included upper- and lower-bound material

Table 15. Critical Chord Member Experimental and Predicted Buckling Strengths					
Specimen (Phase)	Buckling Location	Tested Strength (kips)	Predicted Strength (kips)	Design *K*-Factor[a]	Equivalent *K*-Factor
C1	End panel	308	308	1	1.00
C2	End panel	268	258	1	0.94
C3	Middle panel	350	298	1	<0.50
C4, Phase 1	Middle panel	332	298	1	0.65
C4, Phase 3	Middle panel	334	298	1	0.63
C5, Phase 1	Middle panel	341	298	1	0.53
C5, Phase 3	Middle panel	347	298	1	<0.50

[a] SJI *K*-factors range from 0.75 to 1.0 depending on the member type and buckling mode. Reported design *K*-factor corresponds to the member type and buckling mode observed during the test.

properties, several superposition procedures to generate geometric imperfections, two maximum geometric imperfection magnitudes, three residual stress profiles, and two maximum residual stress magnitudes.

The correlation study leads to the following conclusions regarding angle member buckling simulations:

• The sensitivity of buckling load to small variations in modeled stress-strain response is minor (less than 6%).

• The sensitivity of buckling load to residual stress inclusion is minor (less than 5%) except in small cross sections (up to 10%).

• The full symmetric residual stress profile is consistently conservative and thus appropriate for design applications.

• An out-of-straightness imperfection magnitude of $L/1500$ is appropriate for use with the experimental results.

• The generation of imperfection shapes based on elastic buckling mode shapes within 5 to 10 times the first-mode elastic buckling load produces stable results, with minor sensitivity to the combination method.

Based on these findings, the following recommendations are made for modeling buckling in steel single- and double-angle compression members:

• Using a material stress-strain response curve determined by curve-fitting several representative coupon test results is sufficient; minor variations may be ignored.

• Residual stress effects need only be considered for relatively small cross sections (L1¾×1¾×⅛ or smaller), based on the full-symmetric residual stress profile.

• Initial geometric imperfection shapes should be analytically generated using inversely weighted mode shapes within five times the lowest elastic buckling load and $L/1500$ magnitude.

The truss subassembly correlation study was performed using FE simulations of five double-angle truss subassemblies subjected to a constant moment couple loading (three monotonic, two cyclic). The specimens were designed to investigate buckling in chord members under different detailing configurations. A base FE case was constructed using nominal properties and analytically generated initial imperfections with magnitudes ranging from 0.05 to 0.40 in. The base case used a rigid loading girder and rigid out-of-plane bracing at panel points. The study investigated the effect of explicitly modeling the loading girder stiffness using shear-deformable beams and of modeling the out-of-plane bracing stiffness using nonlinear gap and contact elements. The subassembly correlation study also investigated the effect of subassembly member end conditions on the axial load capacity by comparing experimental and FE simulation results to capacities calculated using the SJI Specification.

The truss subassembly simulations successfully bounded the experimental buckling capacities using initial geometric imperfection magnitudes between 0.10 and 0.40 in. and captured the effect of prior buckling on the subassembly capacities under reversed loading. In general, the analytical load-displacement response was stiffer than observed in the experiment.

The subassembly correlation study leads to the following conclusions:

• Explicitly including the flexibility of the in-plane loading girder resulted in correct predictions of the buckling location. Assuming a rigid loading girder sometimes resulted in inaccurate analytical buckling locations, yet the analytical buckling capacities were not significantly affected. Explicit modeling of in-plane boundary element stiffness should be considered to accurately capture the correct buckling location.

- Explicitly modeling the out-of-plane bracing stiffness did not affect the analytical capacity and resulted in longer simulation times and convergence difficulties.

- For end panels, the chord member end conditions resulted in effective K-factor values close to the SJI design values of 1.0.

- For intermediate panels, the chord member end conditions resulted in effective K-factor values ranging from 0.50 to 0.65 compared to SJI design values of 1.0 (i.e., these SJI design values are conservative).

ACKNOWLEDGMENTS

REFERENCES

ABAQUS (2007), *ABAQUS User's Manual,* Version 6.7, Dassault Systemes, R.I.

Adluri, S.M.R. and Madugula, M.K.S. (1996), "Flexural Buckling of Steel Angles: Experimental Investigation," *Journal of Structural Engineering*, ASCE, Vol. 122, No. 3.

AISC (2005), *Specification for Structural Steel Buildings*, ANSI/AISC 360-05, American Institute of Steel Construction, Chicago, Ill.

AISC (2010), *Specification for Structural Steel Buildings*, ANSI/AISC 360-10, American Institute of Steel Construction, Chicago, Ill.

AISC (2016), *Specification for Structural Steel Buildings*, ANSI/AISC 360-16, American Institute of Steel Construction, Chicago, Ill.

Candas, A.B., Sause, R. and Ricles, J.M. (2008), *Experimental Study on Buckling of Vanadium Steel Members with Single- or Double-Angle Cross-Sections*, Report No. 08-07, Lehigh University ATLSS Center, Bethlehem, Pa.

Galambos, T.V. (1998), *Guide to Stability Design Criteria for Metal Structures*, 5th Ed., John Wiley & Sons, Inc.

SGH (2011), *Correlation and Sensitivity Study on the Buckling of HSLA-V Steel in Single and Double Angle Members*, Project 047079, Simpson, Gumpertz & Heger Inc.

SGH (2012), *Parameter Study to Assess Modifications to the SJI Design Equations for HSLA-V Steels. Rev.1.*, Project 047079, Simpson, Gumpertz & Heger Inc.

SJI (2010), *Standard Specification for Longspan Steel Joists, LH-Series and Deep Longspan Steel Joists, DLH-Series*, ANSI/SJI-LH/DLH, Steel Joist Institute, Florence, S.C.

SJI (2020), *Standard Specification for K-Series, LH-Series, and DLH-Series Open Web Steel Joists and for Joist Girders,* ANSI/SJI 100, Steel Joist Institute, Florence, S.C.

Flange Local Buckling Resistance and Local–Global Buckling Interaction in Slender-Flange Welded I-Section Beams

WAJAHAT LATIF and DONALD W. WHITE

ABSTRACT

AISC *Specification* Chapter F characterizes the flange local buckling (FLB) strength of I-section members having a slender compression flange as the theoretical elastic plate local buckling resistance, ignoring beneficial local post-buckling strength. Previous research has shown that this results in highly conservative strength predictions for slender-flange members. Additionally, potential interaction between local and global lateral-torsional buckling modes is not considered in the AISC *Specification*. These aspects can be important in applications involving the use of slender-flange members. This paper investigates a number of potential methodologies to account for local post-buckling strength as well as local–global buckling interaction in beams having slender flanges. A parametric finite element analysis (FEA) study is conducted considering a range of I-section members. The strength predictions from the proposed methodologies and the AISC *Specification* are evaluated against the FEA results as well as against a database of measured strengths from previous experimental tests of I-section beams governed by FLB. Recommendations are provided focusing on simplicity of the calculations and the efficacy of their predictions.

Keywords: flange local buckling, lateral-torsional buckling, local–global buckling interaction, plate effective width.

INTRODUCTION

The AISC *Specification for Structural Steel Buildings* (AISC, 2016), hereafter referred to as the AISC *Specification*, idealizes the strength of slender-flange I-section beams as the theoretical elastic plate local bucking resistance. This handling of slender-flange members fails to recognize the flange local post-buckling reserve strength and tends to give very conservative predictions as the compression flange becomes more slender. This conservatism is evident from experimental tests documented by White and Jung (2008) and White and Kim (2008). In addition, analytical studies by Seif (2010), Seif and Schafer (2010), Toğay (2018), Toğay and White (2018), Gerard (2020), and Latif (2020) reveal the presence of significant local post-buckling capacity of slender-flange, I-section members loaded in flexure.

One application of slender flanges is in metal building design where it is common to use constant-width flanges while stepping the flange thicknesses, tapering the web depths, and/or stepping the web thicknesses to achieve design economy. In these types of structures, slender compression flanges can be economical in areas of low bending moment demand. Moreover, as the use of higher strength steels becomes more common, a greater number of cases will classify as having slender flanges since the noncompact-flange limit, λ_{rf}, becomes smaller. These aspects of design practice provide the impetus for development of a more accurate FLB strength characterization recognizing the local post-buckling strength of slender flanges.

As the compression flange becomes more slender, the flange local buckling response may have a significant influence on the global lateral-torsional buckling (LTB) strength of the member, due to local–global buckling interaction. The AISC *Specification* does not address this interaction. It is assumed implicitly that the flange local buckling (FLB) predictions for slender flanges are sufficiently conservative such that local–global strength interaction can be neglected. With the development of an improved procedure for predicting the FLB strength of slender-flange members accounting for post-buckling resistance, it may be important to address potential local–global interaction. Early experimental research by Cherry (1960) indicated the presence of significant local–global interaction in thin flange members. More recent analytical studies by Gerard (2020) and Latif (2020) have also shown this behavior.

This paper considers several methodologies for improved prediction of the flexural resistance of slender-flange I-section members accounting for local post-buckling strength and local–global buckling interaction. The procedures are evaluated using nonlinear shell finite element analysis as well as by comparison to previous experimental results.

Wajahat Latif, Research Affiliate, School of Civil and Environmental Engineering, Georgia Institute of Technology, Atlanta, Ga. Email: wajahatlatif@hotmail.com

Donald W. White, Professor, School of Civil and Environmental Engineering, Georgia Institute of Technology, Atlanta, Ga. Email: dwhite@ce.gatech.edu (corresponding)

METHODOLOGIES STUDIED

This section outlines five methodologies studied to characterize the post-buckling strength and local–global buckling interaction in slender-flange members. Representative FLB strength curves from these methodologies, and from the AISC *Specification*, are presented in Figure 1. Figures 2 and 3 outline the FLB and LTB calculations, respectively, for each approach via flowcharts employing a unified format to simplify the process of understanding their logical flow. The reader should note that the AISC *Specification* approach in these figures is shown in the form employed within the AISC/MBMA Design Guide 25 (White et al., 2021), which combines AISC *Specification* Section F4 and F5 provisions into one set of calculations. For instance, using the combined Section F4 and F5 provisions, R_{pg} is taken equal to 1.0 for compact- and noncompact-web members. The reader is referred to AISC *Specification* Sections F4 and F5 for the equations corresponding to R_{pg} and R_{pc}.

Effective Width Methods

The unified effective width method, developed by Peköz (1986), recognizes that slender plate elements are not able to develop full yielding on their gross cross section at their ultimate strength. These elements undergo local buckling, resulting in a loss of stiffness and redistribution of stresses. A plate element subjected to a given member critical compressive stress, F_{cr}, is effective for only a portion of its full width. This effective width is given by the AISC *Specification* Equations E7-2 and E7-3, which may be written as the single equation

$$b_e = \min\left[b_{fc}\left(1 - 0.22\sqrt{\frac{F_{el}}{F_{cr}}}\right)\sqrt{\frac{F_{el}}{F_{cr}}}, b_{fc} \right] \qquad (1a)$$

This equation is commonly referred to as Winter's (1970) curve. In the application of Equation 1a, the flange elastic local buckling stress may be written as

$$F_{el} = \frac{0.9Ek_c}{\lambda_f^2} \qquad (1b)$$

in which k_c is a flange local buckling coefficient and λ_f is the flange slenderness $b_f/2t_f$. The calculation of the member strength using the compression flange effective width obtained from Equation 1a inherently recognizes the post-buckling capacity of slender flange elements. Four approaches are considered in this research that utilize Winter's curve to define member FLB strengths. These approaches are denoted by the abbreviations EW, EW_{Fy}, EW-LG, and REW_{Fy}, where EW, REW, and LG stand for "effective width," "refined effective width," and "local–global interaction," respectively.

In these approaches, the noncompact-flange limit is given by $\lambda_{rf.new} = 0.64\sqrt{k_c\,E/F_y}$ as recommended by Schafer et al. (2020), instead of AISC *Specification* $\lambda_{rf.AISC} = 0.95\sqrt{k_c\,E/F_L}$ (with F_L taken equal to $0.7F_y$ for doubly symmetric sections). The limit $\lambda_{rf.AISC}$ is tied to the anchor point at $0.7M_{yc}$ on the AISC *Specification* theoretical elastic FLB strength curve. Conversely, the limit $\lambda_{rf.new}$ is tied to a point on Winter's curve, where the effective width of the compression flange reaches the full gross width, b_f. Therefore, $M_n = R_{pg}M_{yc}$ at $\lambda_f = \lambda_{rf.new}$, where $R_{pg} = 1$ for compact- and noncompact-web members. For $\lambda_f > \lambda_{rf.new}$, the strengths are defined by using Equation 1a for the compression flange effective width.

Based on recent research, several improvements to the LTB strength and noncompact-web slenderness limit, λ_{rw}, characterizations are incorporated in all the effective width methodologies considered in this paper:
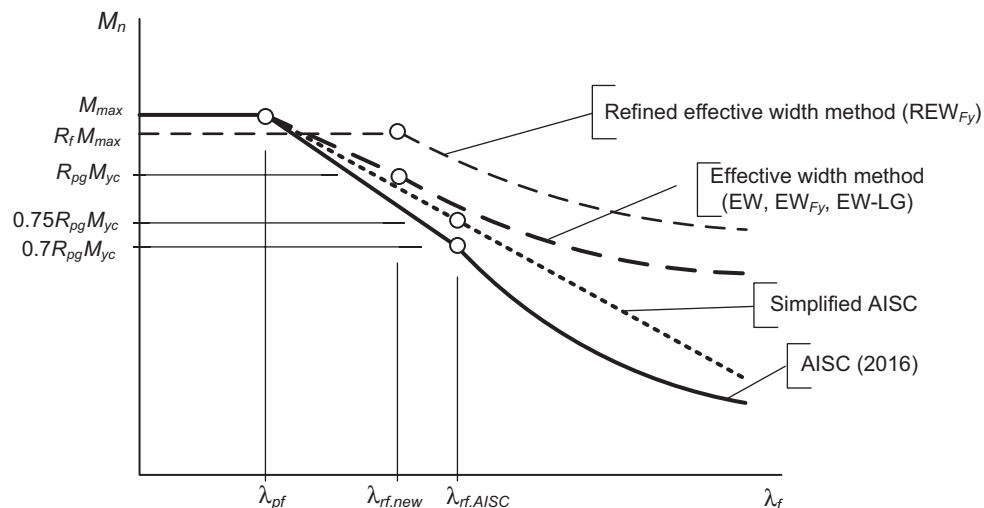

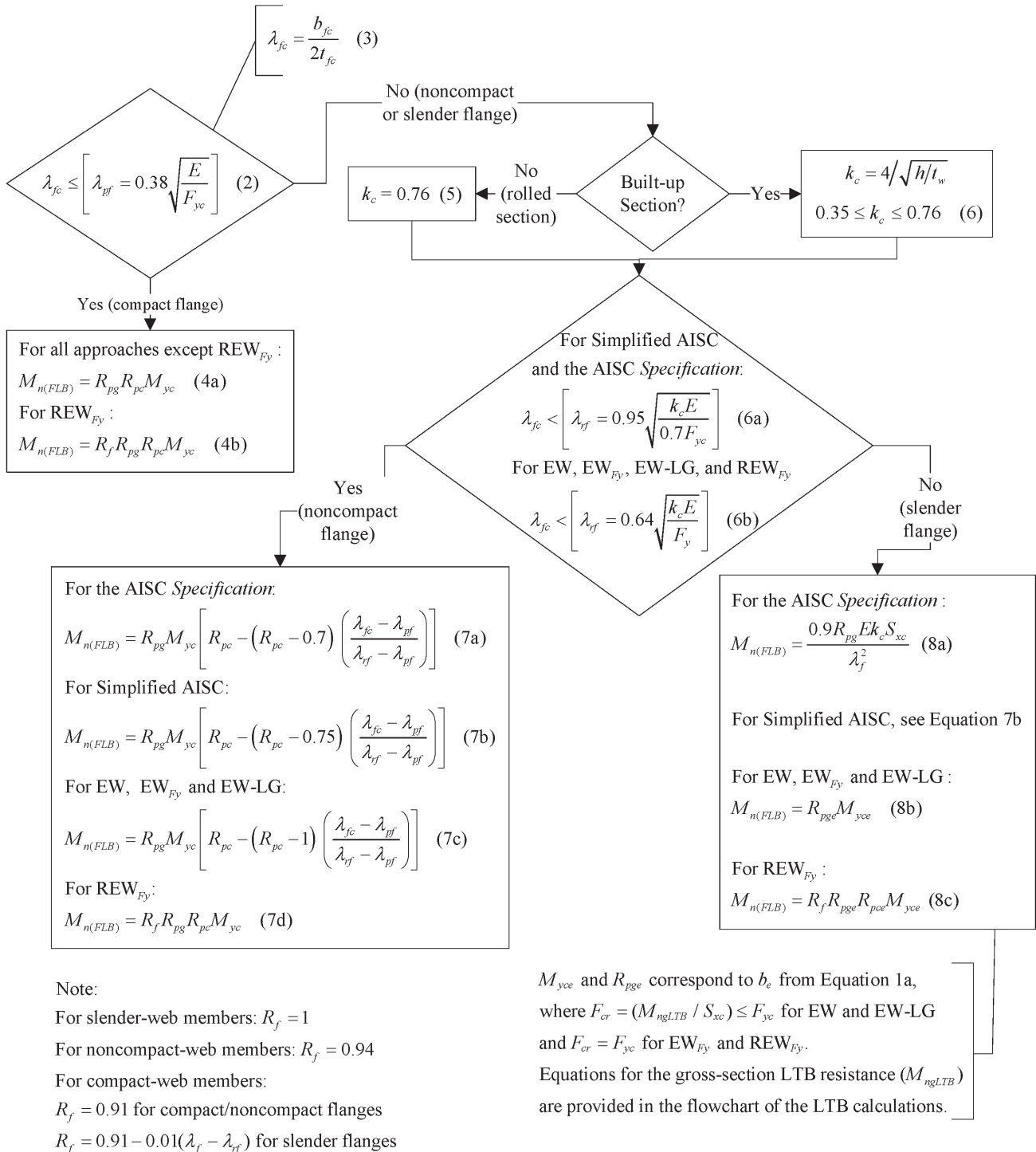*Fig. 1. Illustration of FLB curves based on the approaches studied.*

$$\lambda_{fc} = \frac{b_{fc}}{2t_{fc}} \quad (3)$$

$$\lambda_{fc} \le \left[\lambda_{pf} = 0.38\sqrt{\frac{E}{F_{yc}}} \right] \quad (2)$$

No (noncompact or slender flange)

No (rolled section)

$k_c = 0.76 \quad (5)$

Built-up Section?

Yes

$$k_c = 4/\sqrt{h/t_w}$$
$$0.35 \le k_c \le 0.76 \quad (6)$$

Yes (compact flange)

For all approaches except REW$_{Fy}$:
$$M_{n(FLB)} = R_{pg}R_{pc}M_{yc} \quad (4a)$$
For REW$_{Fy}$:
$$M_{n(FLB)} = R_f R_{pg}R_{pc}M_{yc} \quad (4b)$$

For Simplified AISC and the AISC *Specification*:

$$\lambda_{fc} < \left[\lambda_{rf} = 0.95\sqrt{\frac{k_c E}{0.7F_{yc}}} \right] \quad (6a)$$

For EW, EW$_{Fy}$, EW-LG, and REW$_{Fy}$

$$\lambda_{fc} < \left[\lambda_{rf} = 0.64\sqrt{\frac{k_c E}{F_y}} \right] \quad (6b)$$

Yes (noncompact flange)

No (slender flange)

For the AISC *Specification*:
$$M_{n(FLB)} = R_{pg}M_{yc}\left[R_{pc} - \left(R_{pc} - 0.7\right)\left(\frac{\lambda_{fc} - \lambda_{pf}}{\lambda_{rf} - \lambda_{pf}}\right)\right] \quad (7a)$$

For Simplified AISC:
$$M_{n(FLB)} = R_{pg}M_{yc}\left[R_{pc} - \left(R_{pc} - 0.75\right)\left(\frac{\lambda_{fc} - \lambda_{pf}}{\lambda_{rf} - \lambda_{pf}}\right)\right] \quad (7b)$$

For EW, EW$_{Fy}$ and EW-LG:
$$M_{n(FLB)} = R_{pg}M_{yc}\left[R_{pc} - \left(R_{pc} - 1\right)\left(\frac{\lambda_{fc} - \lambda_{pf}}{\lambda_{rf} - \lambda_{pf}}\right)\right] \quad (7c)$$

For REW$_{Fy}$:
$$M_{n(FLB)} = R_f R_{pg}R_{pc}M_{yc} \quad (7d)$$

For the AISC *Specification* :
$$M_{n(FLB)} = \frac{0.9R_{pg}Ek_c S_{xc}}{\lambda_f^2} \quad (8a)$$

For Simplified AISC, see Equation 7b

For EW, EW$_{Fy}$ and EW-LG :
$$M_{n(FLB)} = R_{pge}M_{yce} \quad (8b)$$

For REW$_{Fy}$:
$$M_{n(FLB)} = R_f R_{pge}R_{pce}M_{yce} \quad (8c)$$

Note:
For slender-web members: $R_f = 1$
For noncompact-web members: $R_f = 0.94$
For compact-web members:
$R_f = 0.91$ for compact/noncompact flanges
$R_f = 0.91 - 0.01(\lambda_f - \lambda_{rf})$ for slender flanges

M_{yce} and R_{pge} correspond to b_e from Equation 1a, where $F_{cr} = (M_{ngLTB}/S_{xc}) \le F_{yc}$ for EW and EW-LG and $F_{cr} = F_{yc}$ for EW$_{Fy}$ and REW$_{Fy}$. Equations for the gross-section LTB resistance (M_{ngLTB}) are provided in the flowchart of the LTB calculations.

Fig. 2. FLB calculations for I-section beams for all methodologies.

For the AISC *Specification* and Simplified AISC - I approaches, $n = 1.1$

For EW, EW$_{Fy}$, EW-LG, REW$_{Fy}$ and Simplified AISC - II, $n = 0.8$. However, for cases having negligible restraint of warping and/or flange lateral bending at the ends of the unbraced length, or where end restraint effects are directly accounted for via an effective length factor or an associated lateral-torsional buckling analysis, use 0.63 instead of 0.8.

"exact" expression

$$r_t = \frac{b_{fc}}{\sqrt{12\left(\dfrac{h_o}{d} + \dfrac{1}{6}\dfrac{h_c t_w}{b_{fc} t_{fc}}\dfrac{h^2}{h_o d}\right)}} \quad (10)$$

$$① \quad L_r = 1.95 r_t \frac{E \cdot S_{xc}}{M_L}\sqrt{\frac{J}{S_{xc}h_o} + \sqrt{\left(\frac{J}{S_{xc}h_o}\right)^2 + 6.76\left(\frac{M_L}{ES_{xc}}\right)^2}} \quad (12)$$

$$L_b \leq L_p = nr_t\sqrt{\frac{E}{F_{yc}}} \quad (9)$$

No (noncompact or slender unbraced length)

Note: $M_L = 0.7M_{yc}$ for the AISC *Specification* and Simplified AISC - I approaches, and $M_L = 0.5M_{yc}$ for EW, EW$_{Fy}$, EW-LG, REW$_{Fy}$ and Simplified AISC- II approaches.

Yes (compact unbraced length)

No (compact or noncompact web)

$$M_{ngLTB} = R_{pg}R_{pc}M_{yc} \quad (11)$$

If $\dfrac{I_{yc}}{I_y} \leq 0.23$ or $\dfrac{h}{t_w} > 150$

Take $J = 0$

Slender web? Yes ($J = 0$)

$$L_b \leq \left[L_r = \pi r_t\sqrt{\frac{ES_{xc}}{M_L}}\right] \quad (13)$$

$L_b \leq L_r$ (14) ①

Yes (noncompact unbraced length)

No (slender unbraced length)

Yes (noncompact unbraced length)

No (slender unbraced length)

$$M_{ngLTB} = \frac{C_b \pi^2 E S_{xc}}{\left(\dfrac{L_b}{r_t}\right)^2}\sqrt{1 + 0.078\frac{J}{S_{xc}h_o}\left(\frac{L_b}{r_t}\right)^2} \leq R_{pc}M_{yc} \quad (15)$$

$$M_{ngLTB} = \frac{C_b R_{pg} \pi^2 E S_{xc}}{\left(\dfrac{L_b}{r_t}\right)^2} \leq R_{pg}M_{yc} \quad (16)$$

$$M_{ngLTB} = C_b\left[R_{pc}M_{yc} - \left(R_{pc}M_{yc} - M_L\right)\left(\frac{L_b - L_p}{L_r - L_p}\right)\right] \leq R_{pc}M_{yc} \quad (17)$$

$$M_{ngLTB} = C_b R_{pg}\left[M_{yc} - \left(M_{yc} - M_L\right)\left(\frac{L_b - L_p}{L_r - L_p}\right)\right] \leq R_{pg}M_{yc} \quad (18)$$

M_{yce} corresponds to b_e from Equation (1a) where $F_{cr} = \left(M_{ngLTB}/S_{xc}\right) \leq F_{yc}$

Otherwise, $M_{yce} = M_{yc}$

For AISC *Specification*, EW, EW$_{Fy}$, REW$_{Fy}$ and Simplified AISC I and II:

$$M_{n(LTB)} = M_{ngLTB} \quad (19)$$

For EW-LG:

$$M_{n(LTB)} = M_{ngLTB}\frac{M_{yce}}{M_{yc}}\frac{R_{pge}}{R_{pg}} \quad (20)$$

Fig. 3. LTB calculations for I-section beams for all methodologies.

a. Consistent with the recommendations proposed in Subramanian et al. (2018), the compact unbraced length limit, L_p, is taken as $0.63r_t\sqrt{E/F_y}$. Subramanian et al. recommend this limit for cases having negligible warping and flange lateral bending restraint at the ends of unbraced length and for cases where end restraint effects are directly accounted for in the resistance calculations.

b. The maximum moment level above which the characterization of the strength by theoretical elastic LTB is no longer sufficient, due to residual stresses, geometric imperfections, and second-order flange lateral bending effects, is taken as $M_L = 0.5M_{yc}$ as recommended by Subramanian et al. (2018) rather than the value used in the AISC *Specification* ($0.7F_yS_{xc}$ for doubly symmetric sections).

c. Based on the recommendations by Subramanian and White (2017b, 2017d), the noncompact-web slenderness limit is taken as $\lambda_{rw} = c_{rw}\sqrt{E/F_y}$, where $c_{rw} = \max\left[\min(5.7, 3.1+5/a_w), 4.6\right]$. This modification influences both the LTB and the FLB strength estimates.

The different effective width approaches may be distinguished as follows.

EW Approach

In the EW approach, the FLB strength of slender-flange members is characterized based on the effective section properties obtained from Equation 1a using the global buckling stress $F_{cr} = (M_{ngLTB}/S_{xc} \le F_{yc})$, where M_{ngLTB} is the global LTB strength. The LTB strength calculations in this procedure are based on the gross cross section.

EW$_{Fy}$ Approach

This approach is similar to the EW approach except that the effective width of the slender flange is calculated at the yield strength (i.e., F_{cr} is taken equal to F_y in Equation 1a).

EW-LG Approach

This approach addresses the FLB strength calculations in a similar manner to the EW approach. However, in addition, the global LTB strength is calculated using the effective section properties to account for a loss in member global buckling capacity resulting from local buckling. That is, an effort is made to directly characterize and account for local–global buckling interaction. The effective width is calculated based on $F_{cr} = (M_{ngLTB}/S_{xc} \le F_{yc})$, where M_{ngLTB} is the global LTB strength based on gross section properties.

Refined Effective Width Method (REW$_{Fy}$)

This procedure is a form of the effective width approach, modified such that the Winter's curve characterizing the strength of slender flanges starts at a plateau resistance, M_{max}, larger than M_{yc} for members with noncompact or compact webs, as illustrated in Figure 1. The critical stress, F_{cr}, in Equation 1a is taken equal to the yield stress, F_y. Furthermore, a curve-fitting variable, R_f, is introduced in the FLB strength curve based on FEA results discussed later. The LTB strength calculations are based on gross cross-section properties.

Simplified AISC Method

A simplified procedure is proposed that uses a straightforward modification of the AISC *Specification* FLB strength curve to provide an accurate to conservative characterization of the significant local post-buckling resistance of I-section member compression flanges with $b_f/2t_f$ values approaching or exceeding the noncompact slenderness limit, $\lambda_{rf.AISC} = 0.95\sqrt{k_c\,E/F_L}$, where F_L is taken equal to $0.7F_{yc}$. In this procedure, the ordinate of the flange local buckling resistance is increased from $0.7M_{yc}$ to $0.75M_{yc}$ at $\lambda_{rf.AISC}$. Furthermore, the noncompact-flange local buckling equation is extended to members with slender compression flanges as a streamlined conservative characterization of the flange post-local buckling strength for these member types. This approach is a simplification of an approach recommended by Toğay (2018) and Toğay and White (2018), where the second anchor point on the noncompact-flange FLB curve, at the noncompact-flange limit, was defined as the point on Winter's curve at $\lambda_{rf.AISC.}$

Using this procedure for the FLB assessment, the following two calculations are considered depending on the handling of the LTB strength and the noncompact-web slenderness limit.

Simplified AISC–I

In this procedure, the LTB strength and the noncompact-web slenderness limit calculations are employed as defined in the AISC *Specification*.

Simplified AISC–II

In this procedure, the recommended LTB strength and noncompact-web slenderness limit calculations outlined in Section 2.1, from Subramanian et al. (2018) and Subramanian and White (2017b, 2017d), are employed.

Table 1. Test Members for FEA Studies Focused on Evaluating Flange Post-Buckling Resistance (b_f = 9 in., h = 28 in., L_b = 25 in., F_Y = 55 ksi)			
Test Category	**Test Name**	**$b_f/2t_f$**	**h/t_w**
Slender-web members	SW-7	7	149
	SW-9	9	149
	SW-11	11	149
	SW-13	13	149
	SW-15	15	149
	SW-18	18	149
Noncompact-web members	NCW-7	7	93.3
	NCW-9	9	93.3
	NCW-11	11	93.3
	NCW-13	13	93.3
	NCW-15	15	93.3
	NCW-18	18	93.3
Compact-web members	CW-7	7	70.0
	CW-9	9	70.0
	CW-11	11	70.0
	CW-13	13	70.0
	CW-15	15	70.0
	CW-18	18	70.0

FEA STUDIES

The FEA studies in this research focus on doubly symmetric I-section members. All the test members have homogenous material properties and a single unbraced length, braced against out-of-plane lateral deflection and twisting at the member ends. Multipoint constraints are implemented that enforce Vlasov kinematics at the member ends (plane sections remain plane except for warping of the flanges) as described by Kim (2010). The study is divided into two main investigations as detailed in the following sections.

Characterization of the FLB Limit State

The first FEA study is designed to evaluate the FLB resistances in the absence of significant LTB slenderness effects. The unbraced length of these members is held constant at (L_b = 25 in.) < L_p to ensure plateau strength LTB conditions. The calculated L_p values for the sections studied range from 26.8 to 34.8 in. The flange and web thicknesses are varied to study a range of flange slenderness values for compact-web, noncompact-web, and slender-web sections. All the members have an assumed yield strength of 60 ksi (representative of typical measured yield strengths for Grade 55 steels) and are subjected to uniform moment. Table 1 outlines the members considered. The test names are selected to reflect the web and flange slenderness values of the members. SW, NCW, and CW denote "slender," "noncompact," and "compact webs," respectively, while the number at the end of the name is the flange slenderness value, $b_f/2t_f$.

Investigation of Local–Global Buckling Interaction

The following additional FEA test simulations are conducted to evaluate member cross sections and lengths potentially most susceptible to local–global buckling interaction. The targeted test members are classified into six cases as outlined in Table 2.

A flange slenderness of $b_f/2t_f$ = 18 is selected for all the members in the local–global buckling interaction study. This is the upper limit of allowable flange slenderness recommended by AISC Design Guide 25 (White et al., 2021) and represents a relatively thin flange case. The post-buckling deformations of these flanges are expected to have significant potential impact on the global buckling strength. The slender-web sections studied have relatively deep webs compared to the compact-web sections, which have relatively shallow webs. The shallower webs are selected to evaluate situations where the strength may be more sensitive to the FLB behavior. This is because the elastic properties of these sections, such as the moment of inertia, have a

Case	Description	Test Names	h/t_w	h
	Table 2. Test Cases for Study of Potential Local–Global Buckling Interaction (b_f = 9 in. and $b_f/2t_f$ = 18 in.)			
1	Slender flange–slender web, uniform moment, F_y = 60 ksi	UM-Lb#-SF-SW-60	149	28
2	Slender flange–slender web, uniform moment, F_y = 100 ksi	UM-Lb#-SF-SW-100	149	28
3	Slender flange–compact web, uniform moment F_y = 60 ksi	UM-Lb#-SF-CW-60	36.0	9
4	Slender flange–compact web, uniform moment F_y = 100 ksi	UM-Lb#-SF-CW-100	36.0	9
5	Slender flange–slender web, moment gradient, F_y = 60 ksi	MG-Lb#-SF-SW-60	149	28
6	Slender flange–slender web, moment gradient, F_y = 100 ksi	MG-Lb#-SF-SW-100	149	28

smaller contribution from the web. A number of beams are subjected to a linearly varying moment (maximum moment at one end of the unbraced length and zero moment at the other end) in this study, in addition to specimens subjected to uniform bending.

The unbraced lengths for each section type are varied to investigate local–global buckling interaction. The notation for the test names is selected to uniquely define each member. For example, test member UM-LB85-SF-SW-60 indicates a member subjected to uniform moment with an unbraced length of 85 in, slender flanges, a slender web and F_y = 60 ksi. The notations MG and CW appearing in the test names in Table 2 stand for "moment gradient" and "compact web," respectively.

FINITE ELEMENT MODELING PARAMETERS

Element Type and FEA Discretization

The webs and flanges of the members are modeled using the S4R element in ABAQUS (Simulia, 2013), which is a four-node, quadrilateral, large-strain shell element. The members are evaluated using full, nonlinear finite element analysis, including material and geometric nonlinearity. The mesh density corresponds to 12 elements across the flange width and 30 elements through the web depth for the 28-in. deep web members. For the 9-in. deep web members studied, 12 elements are employed through the web depth. These relatively dense meshes perform well in terms of convergence of the finite element solution and are selected based on the mesh discretization studies by Subramanian (2015). The number of elements along the length is calculated such that the aspect ratio of each element is approximately 1.0 within the web.

Material Properties

The test members are modeled using a J2 plasticity model with isotropic hardening. All test sections have homogenous material properties corresponding to either F_y = 60 ksi or F_y = 100 ksi, depending on the test case being studied. The modulus of elasticity, E, is taken as 29,500 ksi, which represents a common mean value for structural steels. For the Grade 60 steels, intended to be representative of the actual yield strength in typical metal building frame members fabricated with Grade 55 steels, the post-elastic stress-strain response is modeled with a tangent stiffness of $E/1000$ up to a strain-hardening strain value of 10 times the yield strain, ε_y. The strain-hardening modulus is idealized as $E/50$ after this point. This is a common representation of the stress-strain response of ordinary structural steels (ASCE, 1971) and is adequate for the test simulations under consideration since the strain levels observed exceed the strain hardening strain by a minor amount and only within localized regions in these studies. For the Grade 100 steels, F_y is modeled directly as 100 ksi, and a constant post-elastic tangent stiffness of $E/1000$ is employed without any characterization of strain hardening. This provides a representation of the stress-strain response for some of these types of steels, such as the plates employed in the girder tests by Fahnestock and Sause (1998). Some high-strength steels do not exhibit a sharp yield response. This potential attribute is not addressed in this research.

Residual Stresses

The best-fit Prawel residual stress pattern used previously by Kim (2010) and Subramanian (2015) has been adopted for these studies. The residual stress values are halved based on the recommendations for LTB tests by Subramanian and White (2017a, 2017b, 2017c) to correlate with the

mean results from experimental tests. Additionally, the web residual stresses are taken equal to zero. This is a reasonable approximation for the slender web h/t_w values studied since the slender webs would buckle prior to reaching the base value for the web compressive residual stresses defined in the best-fit Prawel pattern. For the members with compact webs, the web can sustain these compressive stresses; however, the residual stresses in the web have a minor impact on the member response in these cases. The residual stress pattern employed for all the studies is illustrated in the left diagram in Figure 4. In addition, the test cases in Table 1 are simulated using the full best-fit Prawel residual stress pattern, including residual stresses in the web. The full residual stress pattern is shown in the right-hand diagram in Figure 4.

Geometric Imperfections

Three types of geometric imperfections—namely, flange tilt, web out-of-flatness, and flange sweep—are considered. The flange tilt and web out-of-flatness patterns are obtained by executing an elastic eigenvalue buckling analysis of the test member subjected to uniform axial compressive stress, and in which the web-flange juncture locations are continuously constrained against lateral displacement.

The flange tilt in the buckling mode obtained for the flanges is scaled to one-half of the tolerance recommended in CEN (2006) and the out-of-flatness in the buckling mode

for the web is scaled to one-half of the tolerance value in the *Metal Building Systems Manual* (MBMA, 2012). Recent research (Subramanian and White, 2017a) has shown that geometric imperfections of one-half typical specified tolerance values provide close correlation with the mean predictions from experimental LTB results. These one-half tolerance values are shown in Figure 5.

A flange sweep equal to approximately one-half of the value noted in AWS (2020) is applied at the web-compression flange juncture as shown in Figure 6. The tension flange is held straight when generating this imperfection.

In addition to these recommended one-half tolerance values, the test cases in Table 1 are also simulated with the full geometric imperfections. It should be noted that the full flange tilt imperfection from CEN (2006) is approximately 40% of the corresponding more restrictive value of the flange tilt tolerances from MBMA (2012), and the full flange sweep tolerance from AWS (2020) is approximately one-half the corresponding general member flange sweep tolerance in MBMA (2012).

RESULTS AND DISCUSSION

Characterization of the FLB Limit State

Figures 7 through 9 compare the FEA results for the test cases outlined in Table 1 with the strength predictions from the methodologies listed earlier for the slender-,
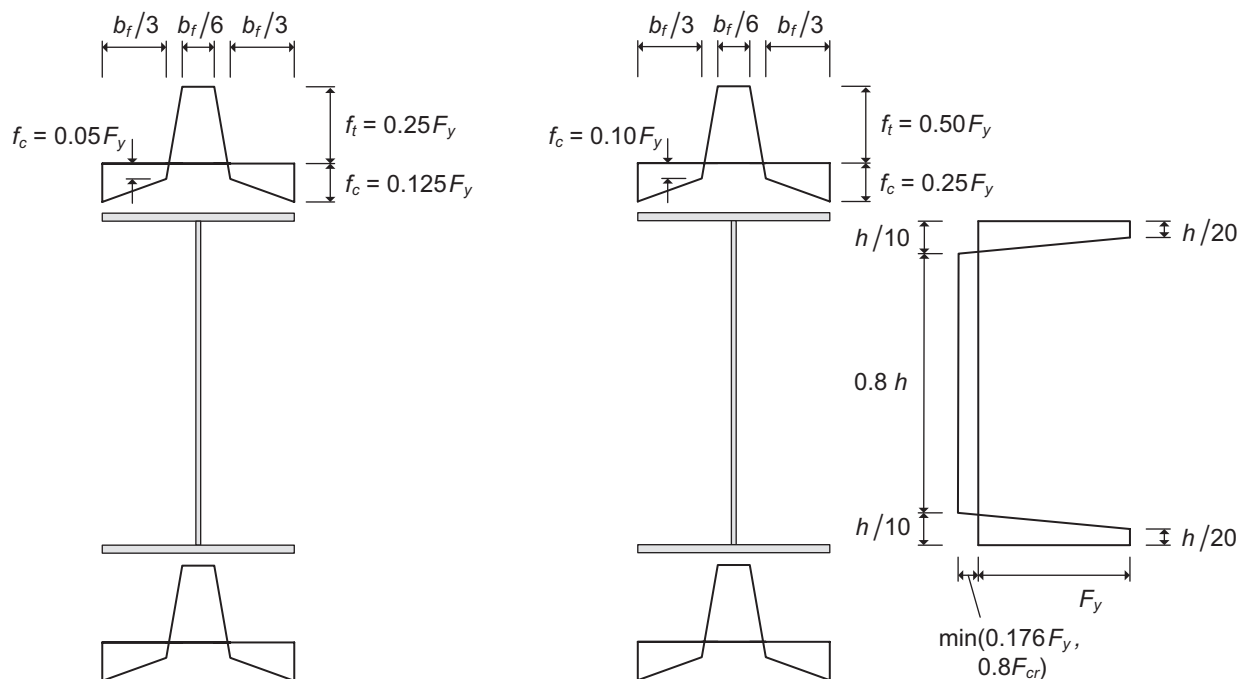
Fig. 4. Half residual stress pattern (left) and full residual stress pattern, including web stresses (right) employed in finite element analysis simulation studies.

noncompact-, and compact-web test members, respectively. In these plots, FEA(H) denotes FEA simulation results using the half residual stress and half geometric imperfection patterns, while FEA(F) denotes results using the full residual stress and full geometric imperfection patterns. Because the strength of all these members is governed by FLB, the EW and EW-LG procedures give the same predictions. Also, the critical stress, F_{cr}, is equal to F_y for these noncompact- and compact-web members, while it is very close to F_y for the slender-web members (M_{ngLTB} is reduced slightly below the yield moment by the strength reduction factor R_{pg} for the slender-web sections). For this reason, the predictions by the EW_{Fy} method are either equal to, or very close to, the EW and EW-LG predictions (i.e., the curves are indistinguishable even in cases where there are small differences). Therefore, the strength predictions by the EW, EW-LG, and EW_{Fy} methods are simply referred as EW in the plots. Similarly, the simplified AISC-I and AISC-II calculations are shown by a single strength curve, labeled as Simplified AISC, since these procedures only differ in their treatment of the LTB strength calculations (which do not govern for these test cases).

It is evident from these plots that the AISC *Specification* procedure gives highly conservative predictions compared to both the FEA(H) and FEA(F) results as the flange slenderness increases. This conservatism at high flange slenderness values is reduced by the use of the Simplified AISC curve. The EW curve consistently gives good correlation with the FEA(F) results for all three plots at the larger flange slenderness values, while the REW_{Fy} curve gives slightly conservative to accurate predictions for FEA(H) tests but significantly overestimates the FEA(F) strengths for the noncompact- and compact-web cases. However, for the noncompact- and compact-web cases, the EW curve suggests a rapid decrease in the strength when the flange slenderness is varied between the compact and noncompact limits. This rapid drop in the predicted capacity is an attribute of the EW approach and is not representative of physical or FEA simulation test data. Conversely, for slender-web members, the FLB strength curve does not have any noncompact-flange region in the EW calculations. That is, in the EW procedures, the start of the FLB strength reduction on Winter's curve corresponds to the plateau strength, $R_{pg}M_{yc}$. The REW_{Fy} procedure uses a curve fitting variable, R_f, to achieve more accurate predictions of the FEA(H) simulation results for the compact- and noncompact-web members. The difference between the strength predictions by the FEA(F) and FEA(H) solutions provides an indication of
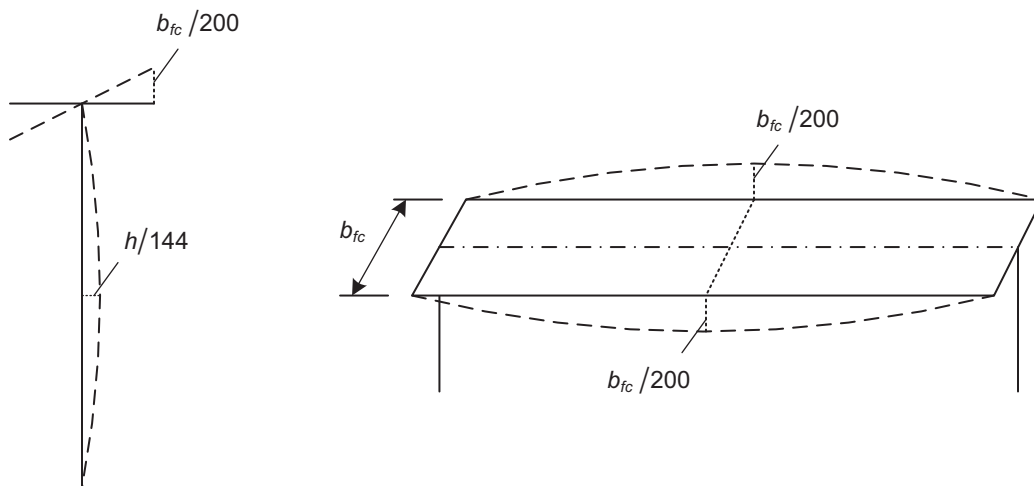
Fig. 5. Recommended one-half tolerance web out-of-flatness and flange tilt imperfections.
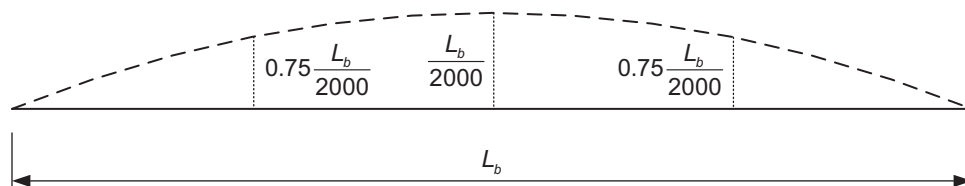
Fig. 6. Recommended one-half tolerance flange sweep imperfection.
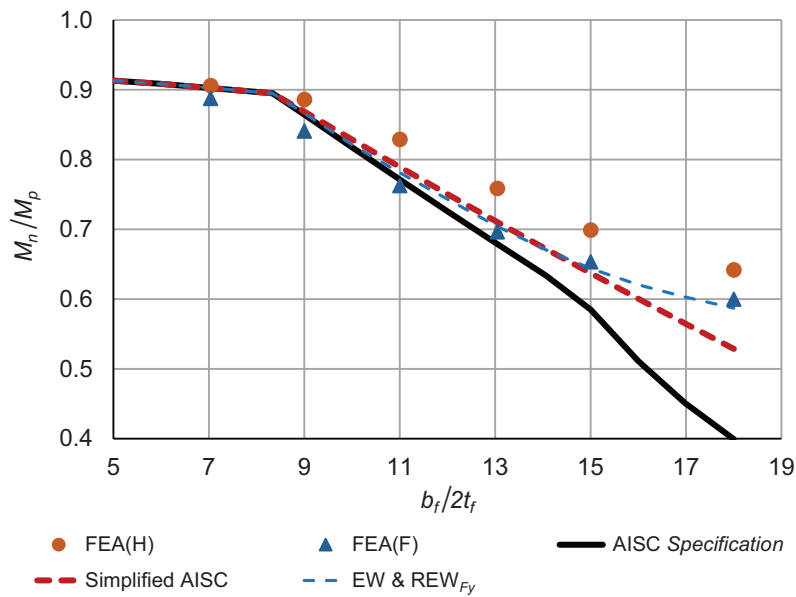
Fig. 7. Comparison of strength predictions by FEA simulations and
different methodologies versus flange slenderness for slender-web members.
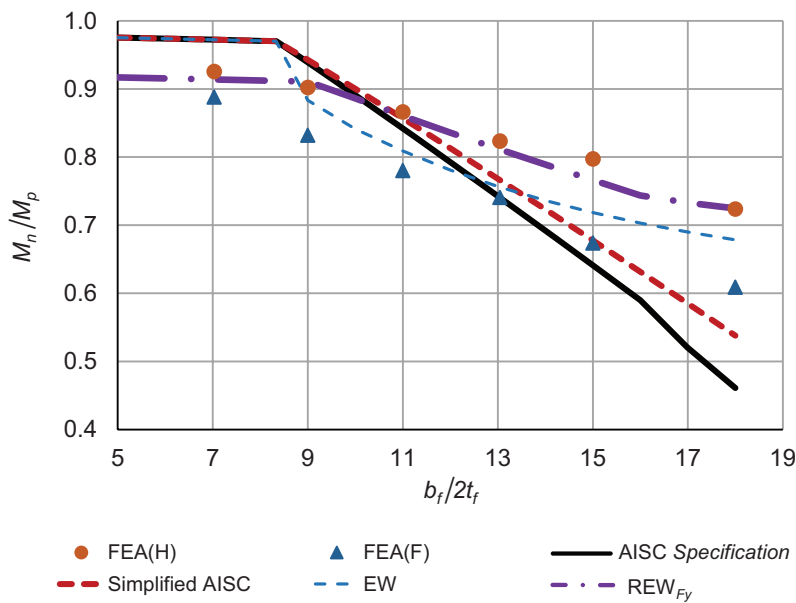
Fig. 8. Comparison of strength predictions by FEA simulations and
different methodologies versus flange slenderness for noncompact-web members.

the sensitivity to variations in the residual stresses and geometric imperfections that might be experienced in physical members.

It is noted that the FEA results do not attain the plateau strength, $R_{pc}M_{yc}$, for the compact-flange members corresponding to the smaller $b_f/2t_f$ values in Figures 8 and 9. However, the available experimental data (White and Jung, 2008; White and Kim, 2008), summarized earlier, indicates that the FLB plateau strengths are indeed achieved at the defined compact-flange limits.

Investigation of Local–Global Buckling Interaction

The results for test cases 1 to 6 (Table 2) are shown in Figures 10 through 15. These are plotted as the professional bias factor, M_{FEA}/M_n, where M_{FEA} is the strength determined from the FEA simulation and M_n corresponds to the strength predicted by any of the six procedures being evaluated. The solid markers along the respective curves denote the instances where the LTB equations govern, while the hollow markers indicate the cases where the FLB equations govern. Table 3 provides overall summary statistics for the professional bias factor, M_{FEA}/M_n, of all the methods for these six test cases, all having $b_f/2t_f = 18$.

The AISC *Specification* procedure tends to give the greatest conservatism and the largest dispersion of the predictions of all the methods (mean M_{FEA}/M_n of 2.56 and COV = 0.31 for all the conducted tests). The Simplified AISC-I approach mitigates this conservatism for both 60 ksi and 100 ksi members. However, as illustrated by Figures 10, 12, and 13, both the AISC *Specification* and Simplified

AISC-I procedures exhibit M_{FEA}/M_n values less than 1.0 in certain tests. These tests correspond to members where the strength predictions are governed by the AISC *Specification* LTB calculations. These predictions are improved by using the recommended LTB and web noncompact limit, λ_{rw}, calculations in the Simplified AISC-II method.

All the other methods aim to capture the post-buckling strength of the slender compression flange by using an effective width approach. The EW procedure performs well for the cases with $F_y = 60$ ksi; however, these predictions tend to be unconservative for 100-ksi members (mean $M_{FEA}/M_n = 0.97$ and minimum $M_{FEA}/M_n = 0.84$). This is due to a lack of accounting for local–global interaction because the LTB calculations are based on the gross cross-section properties. In contrast, the EW-LG procedure provides conservative predictions on average (mean $M_{FEA}/M_n = 1.17$ for all of the tests) and has the smallest dispersion of all the methods considering all of the tests (maximum $M_{FEA}/M_n = 1.33$, minimum $M_{FEA}/M_n = 0.94$, and a COV of 0.07). The differences between the EW and EW-LG predictions shows that the 100-ksi members studied are more susceptible to local-global buckling interaction than the 60-ksi members.

The strength predictions by the EW_{Fy} and REW_{Fy} procedures overlap for all the slender-web members, where $R_f = 1.0$, and for all the tests governed by LTB because the LTB strength calculations are the same for both of these methods. Similar to the EW procedure, the EW_{Fy} and REW_{Fy} methods perform well for members with $F_y = 60$ ksi; however, the predictions tend to be unconservative for 100-ksi members at certain unbraced lengths due
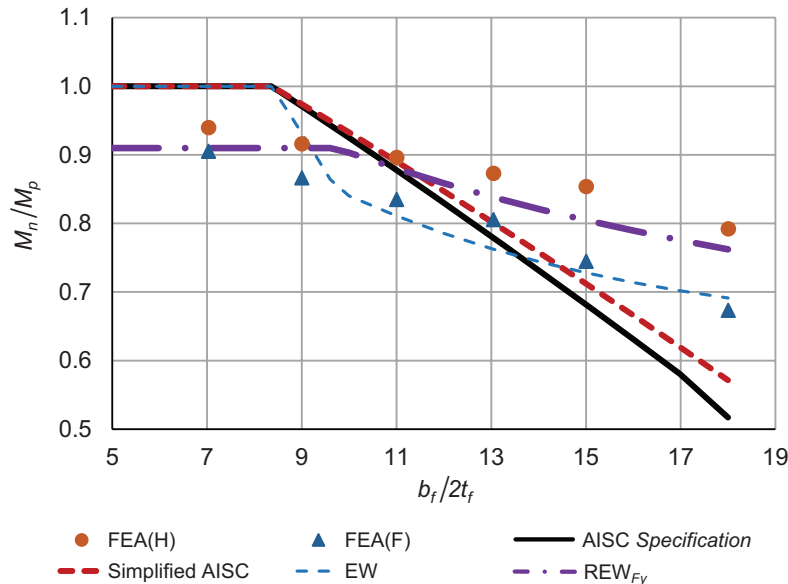

Fig. 9. Comparison of strength predictions by FEA simulations and different methodologies with flange slenderness for compact-web members.
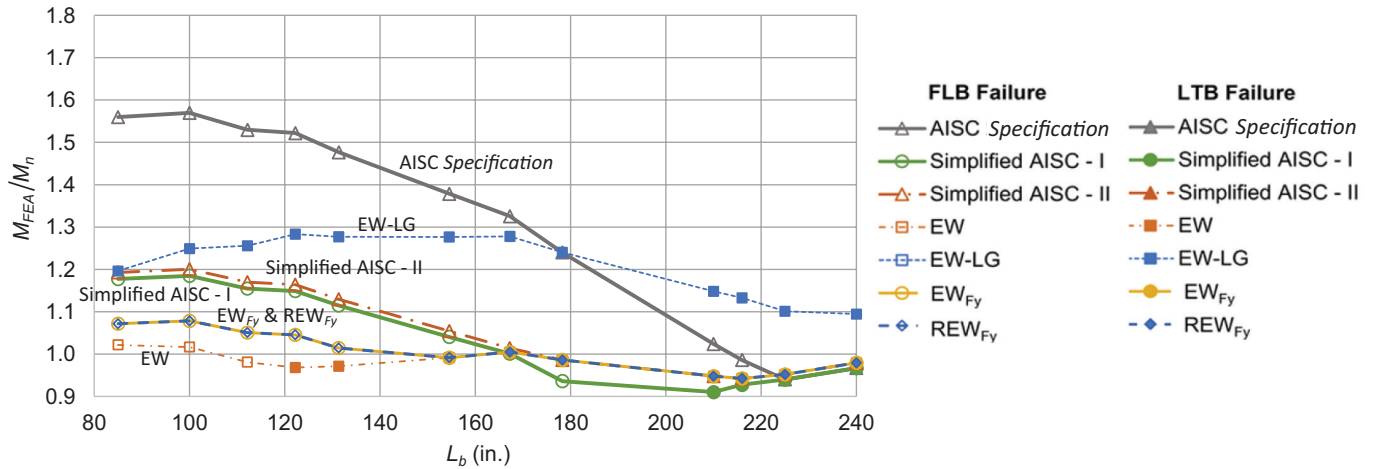
Fig. 10. Comparison of M_{FEA}/M_n for case 1 members (slender-flange–slender-web members subjected to uniform moment loading, $F_y = 60$ ksi).
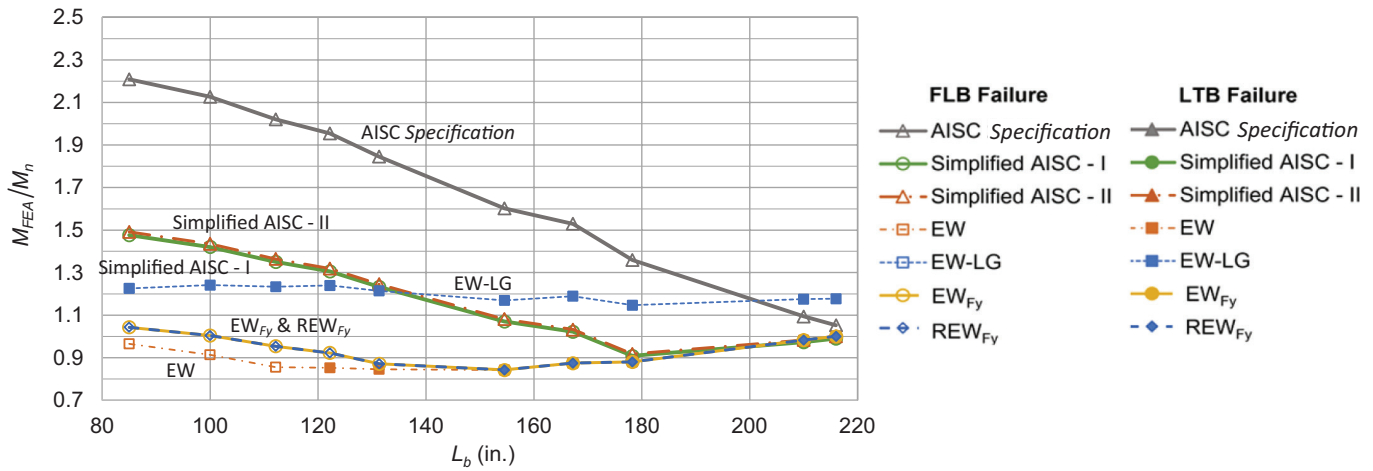

Fig. 11. Comparison of M_{FEA}/M_n for case 2 members (slender-flange–slender-web members subjected to uniform moment loading, $F_y = 100$ ksi).
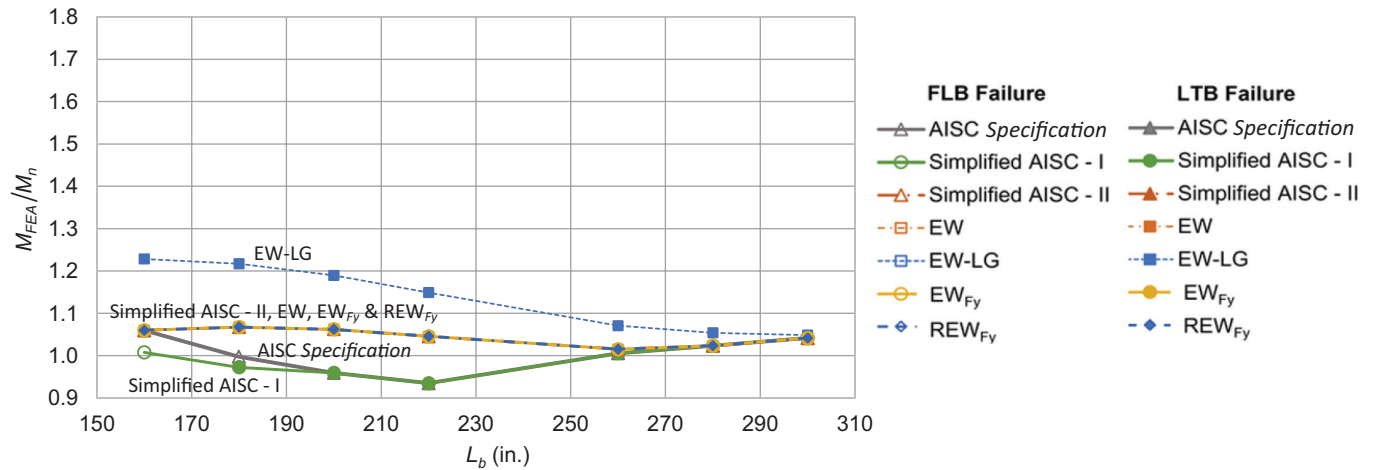

Fig. 12. Comparison of M_{FEA}/M_n for case 3 members (slender-flange–compact-web members subjected to uniform moment loading, $F_y = 60$ ksi).
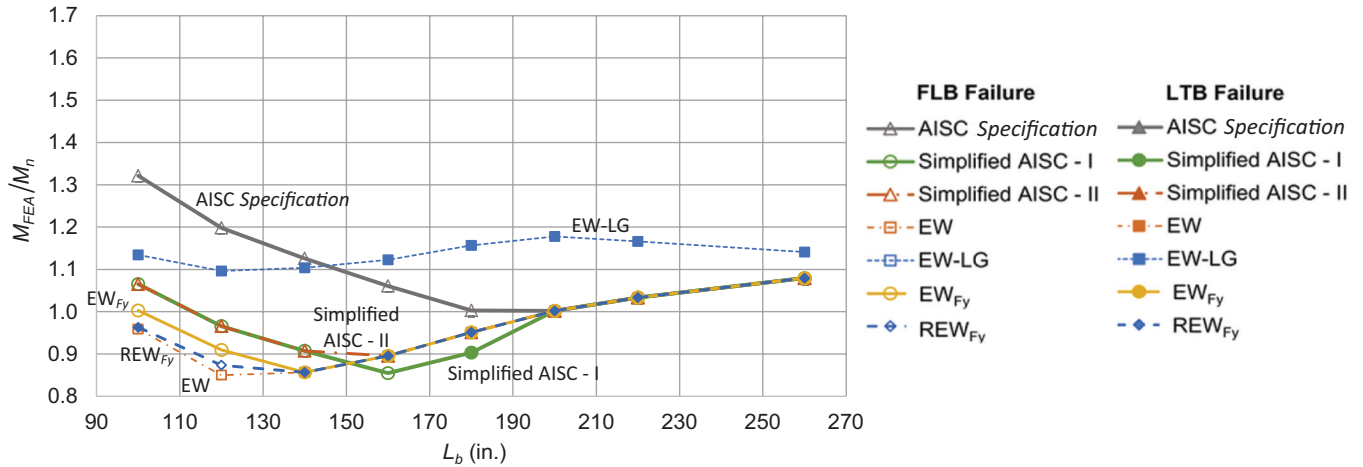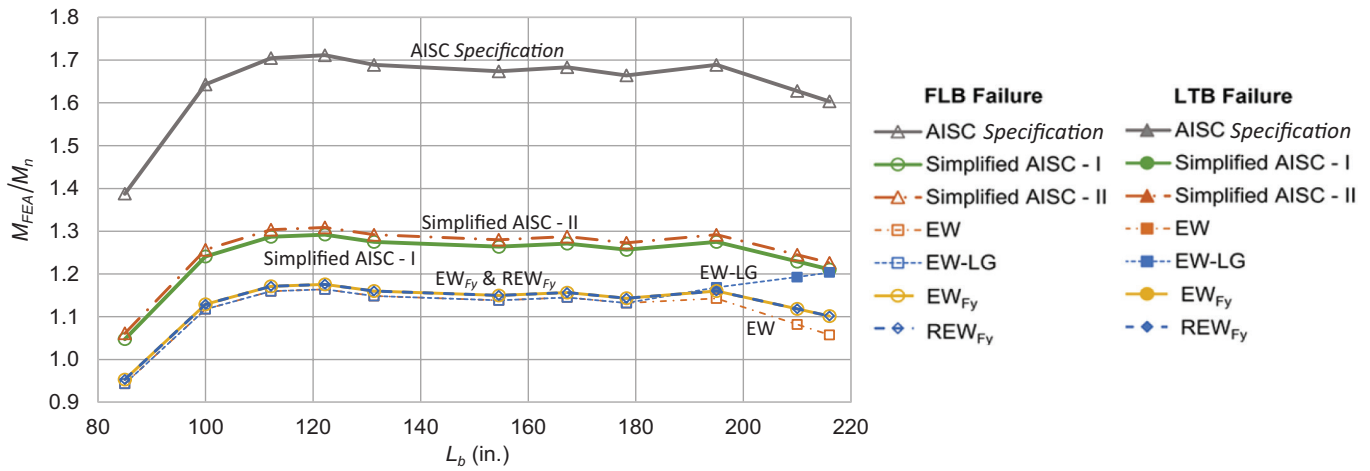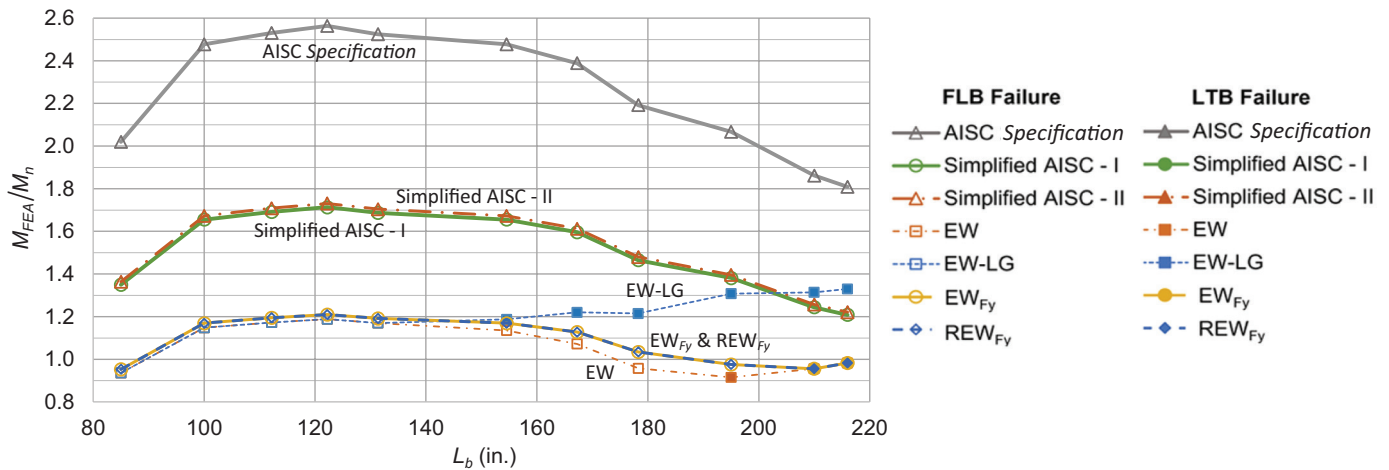
Fig. 13. Comparison of M_{FEA}/M_n *for case 4 members (slender-flange–compact-web members subjected to uniform moment loading,* $F_y = 100$ *ksi).*

Fig. 14. Comparison of M_{FEA}/M_n *for case 5 members (slender-flange–slender-web members subjected to a linearly varying moment,* $F_y = 60$ *ksi).*

Fig. 15. Comparison of M_{FEA}/M_n *for case 6 members (slender-flange–slender-web sections under a linearly varying moment,* $F_y = 100$ *ksi).*

		AISC Specification	Simplified AISC-I	Simplified AISC-II	EW	EW-LG	EW_{Fy} and REW_{Fy}
Category	Statistics						
All tests	Maximum	2.56	1.71	1.73	1.19	1.33	1.21
	Minimum	0.93	0.85	0.90	0.84	0.94	0.84
	Average	1.54	1.17	1.19	1.01	1.17	1.03
	COV	0.31	0.19	0.19	0.10	0.07	0.09
Tests with F_y = 60 ksi	Maximum	1.71	1.29	1.31	1.16	1.28	1.18
	Minimum	0.93	0.91	0.94	0.94	0.94	0.94
	Average	1.35	1.10	1.13	1.04	1.17	1.06
	COV	0.22	0.12	0.11	0.07	0.07	0.07
Tests with F_y = 100 ksi	Maximum	2.56	1.71	1.73	1.19	1.33	1.21
	Minimum	1.00	0.85	0.90	0.84	0.94	0.84
	Average	1.74	1.25	1.26	0.97	1.18	1.00
	COV	0.32	0.22	0.22	0.11	0.06	0.11
Tests with a compact web	Maximum	1.32	1.08	1.08	1.08	1.23	1.08
	Minimum	0.93	0.85	0.90	0.85	1.05	0.86
	Average	1.06	0.98	1.01	1.00	1.14	1.00
	COV	0.09	0.06	0.06	0.08	0.05	0.07
Tests with a slender web	Maximum	2.56	1.71	1.73	1.19	1.33	1.21
	Minimum	0.94	0.91	0.92	0.84	0.94	0.84
	Average	1.71	1.24	1.26	1.01	1.19	1.04
	COV	0.26	0.18	0.18	0.10	0.07	0.10

Table 3. Statistics for Local–Global Buckling Interaction Test Cases

to a lack of accounting for local–global interaction. The EW_{Fy} and REW_{Fy} methods give slightly larger M_{FEA}/M_n values on average compared to the EW method (mean $M_{FEA}/M_n = 1.00$ for 100-ksi members and mean $M_{FEA}/M_n = 1.03$ for all the conducted tests). The overall statistics for the EW_{Fy} and REW_{Fy} procedures are the same to the significant digits shown in Table 3 because these methods give the same strength predictions for most of the tests.

For the moment gradient tests (Figures 14 and 15), all but a few of the test members are predicted to fail in FLB by all of the procedures. The AISC Specification procedure gives highly conservative predictions for these cases.

For the compact-web test cases (Figures 12 and 13), the Simplified AISC-II method gives the "best" predictions of all the methods (mean $M_{FEA}/M_n = 1.01$ with a small COV of 0.06, a minimum $M_{FEA}/M_n = 0.90$, and a maximum $M_{FEA}/M_n = 1.08$). The Simplified AISC-II method also performs reasonably well for the test cases with $F_y = 60$ ksi, giving a mean $M_{FEA}/M_n = 1.13$, a COV of 0.11, a minimum M_{FEA}/M_n of 0.94, and a maximum M_{FEA}/M_n of 1.31. However, this method tends to give more conservative predictions and larger dispersion (mean $M_{FEA}/M_n = 1.26$ and COV = 0.22) for the 100-ksi members.

Figure 16 shows an example of significant compression flange local buckling deformations at the peak load for the UM-Lb154-SF-SW-100 test member. The magnified deformed shape (scale factor = 5.0) is plotted showing the von Mises stress contours on the top surface of the flanges.

Comparison with Experimental Data

Figure 17 summarizes the predictions of the strengths from uniform bending experimental tests in which the flexural resistance is governed by flange local buckling based on the AISC Specification calculations. The Lew and Toprac (1968) and Carskaddan (1968) tests had flange yield strengths exceeding 100 ksi, whereas the test by Basler et al. (1960) had a compression flange yield strength of only 35.4 ksi. The tests by Holtz and Kulak (1973) had a compression flange yield strength of 46.8 ksi, while the tests by Holtz and Kulak (1975) had a compression flange yield strength of only 34.7 ksi. Johnson's (1985) tests had F_{yc} between 53.7 ksi and 63.4 ksi. All of these specimens were doubly symmetric except for the test by Basler et al., in which the compression flange was larger than the tension flange.

One of the tests from Johnson (1985) and two of the tests from Holtz and Kulak (1973) had compact flanges. As such, the $\lambda_{fc}/\lambda_{pf}$ values for these tests are less than 1.0 in Figure 17, and the flange local buckling resistance corresponds to the flexural strength plateau for these specimens. These tests are included since they were a part of a series of tests that were focused on evaluating flange local buckling resistance.

The specimens tested by Johnson (1985), Basler et al. (1960), and Lew and Toprac (1968) with $\lambda_{fc}/\lambda_{pf} > 1.75$ are classified as slender-flange members per the AISC *Specification*. It is evident that the AISC *Specification* gives conservative strength estimates for these members. This behavior is identified also by the FEA studies discussed previously. This conservatism is mitigated by the other approaches.

The predictions by EW-LG procedure are governed by the LTB resistance (based on effective section properties) for a number of the tests, resulting in slightly larger M_{test}/M_n values in Figure 17(f) compared to those obtained using the other effective width based approaches. While the EW-LG approach tends to gives some of the most conservative predictions for the tests with intermediate flange slenderness values, it performs well in bringing the

M_{test}/M_n values close to 1.0 for several of the tests with larger flange slenderness values. The other effective width-based procedures perform well in bringing the mean of M_{test}/M_n closer to 1.0, but they give M_{test}/M_n values significantly less than 1.0 for a number of the tests with larger λ_{fc} values. This is particularly notable for two of the tests with larger $\lambda_{fc}/\lambda_{pf}$ values conducted by Lew and Toprac (1968), which have improved predictions using the EW-LG method; for the single test conducted by Basler et al. (1960), which has relatively small yield strengths and is governed by FLB in all cases; and for several of the tests conducted by Johnson (1985) that had noncompact and compact webs, where the adjustments increasing the corresponding calculated strengths in the REW$_{Fy}$ method result in an over-prediction of the test results ($M_{test}/M_n < 1.0$).

Compared to the more elaborate flange effective width-based approaches discussed in this paper, it is evident that the Simplified AISC approach, which modifies the AISC *Specification* FLB calculations by increasing the ordinate of the second anchor point of the linear equation for noncompact flanges, and extending the use of this equation into the slender-flange range, performs well in predicting accurate to conservative strengths for all the test members.
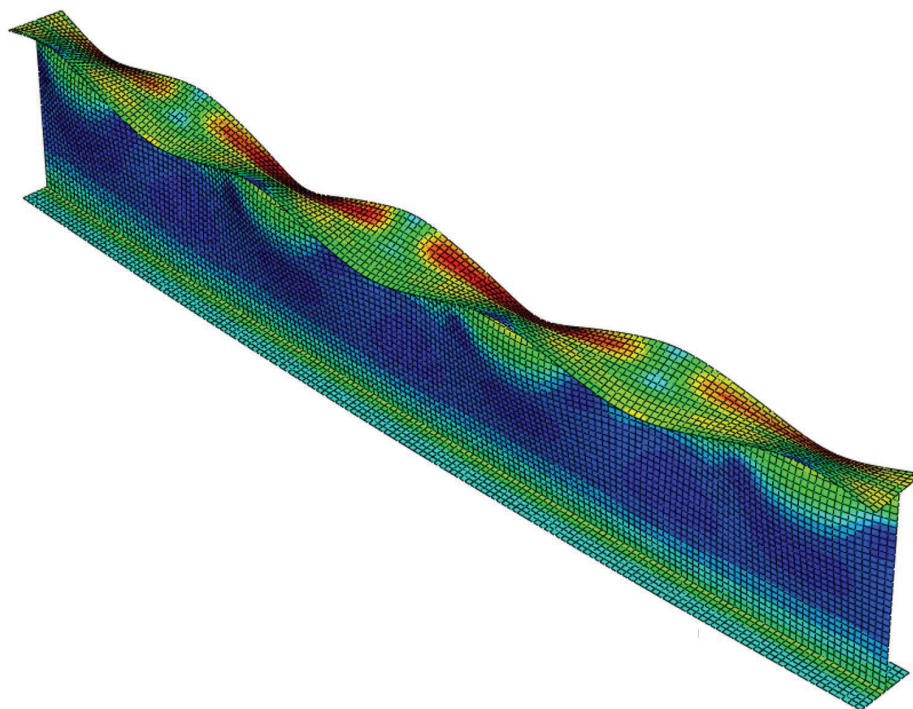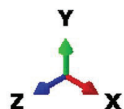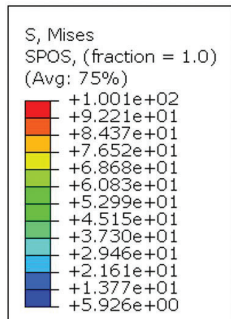

Fig. 16. Deformed shape of UM-Lb154-SF-SW-100 test member at peak load plotted showing the von Mises stress contours at the top surface of the flanges (displacement scale factor = 5.0).
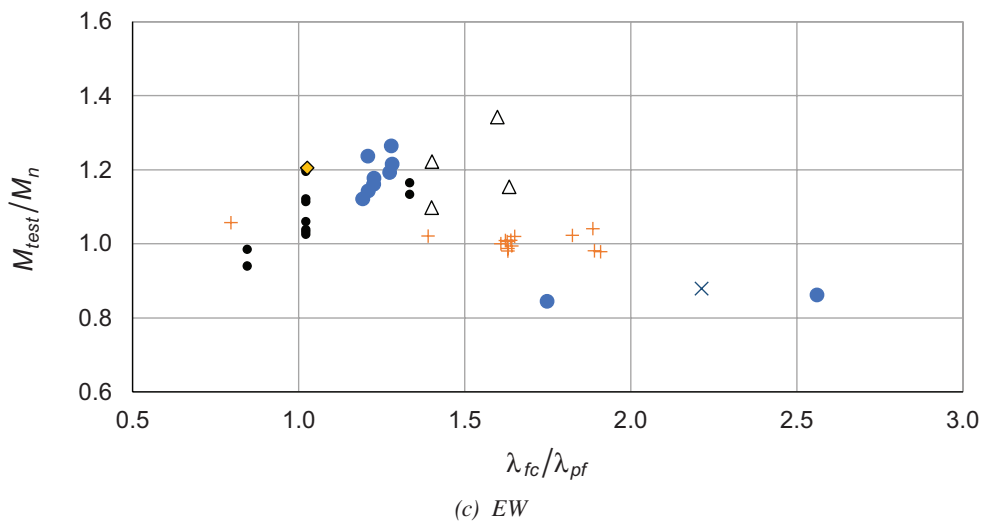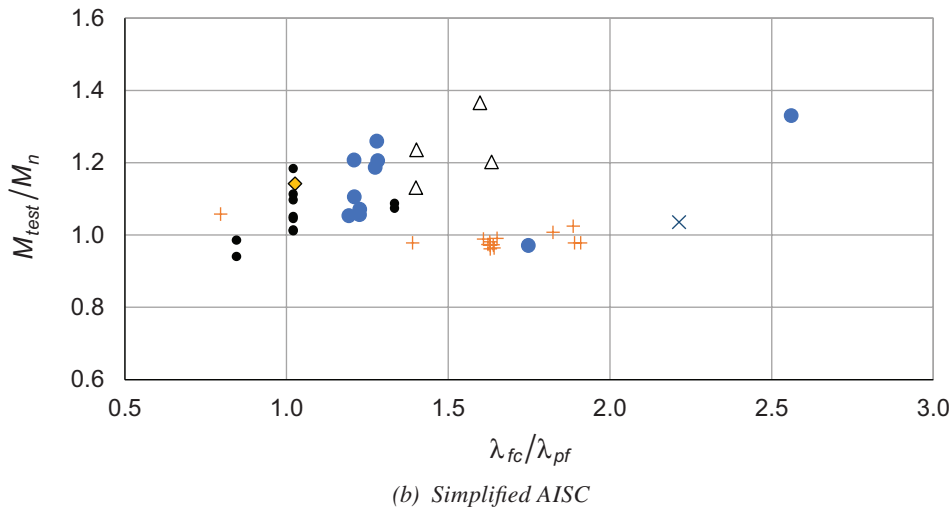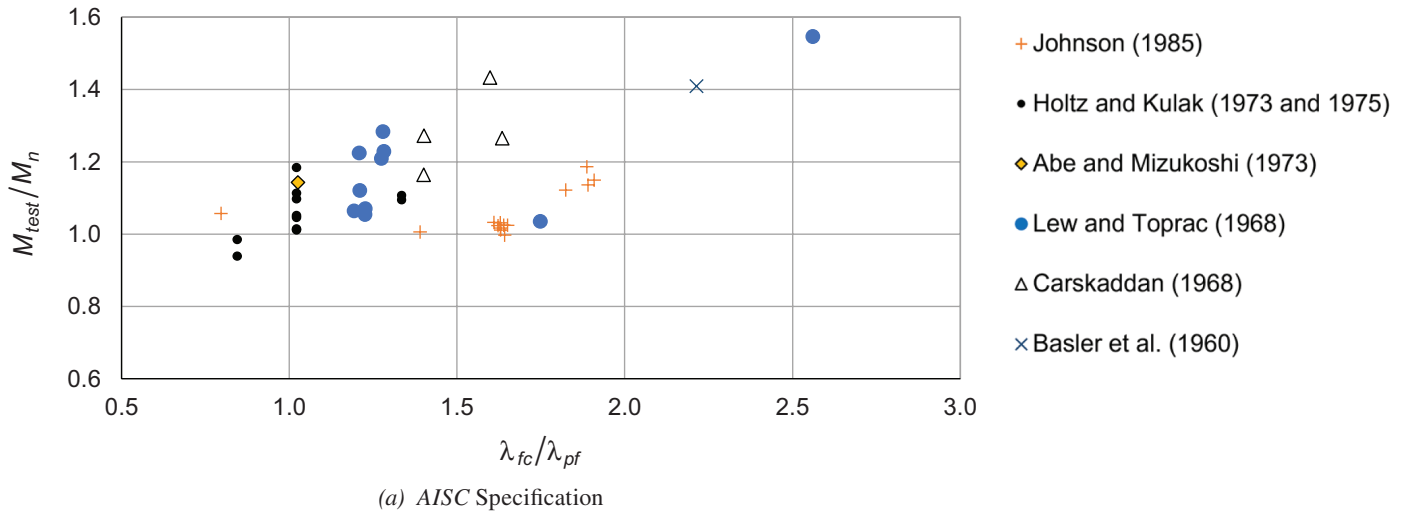
Fig. 17 (a,b,c). Comparison of M_{test}/M_n *for experimental data versus* λ_f/λ_{pf} *for all methodologies studied, uniform bending tests.*
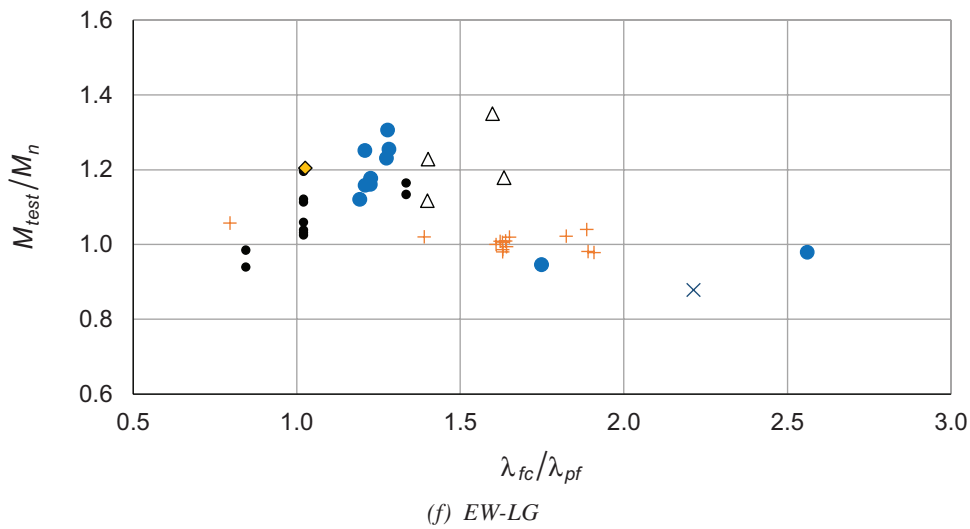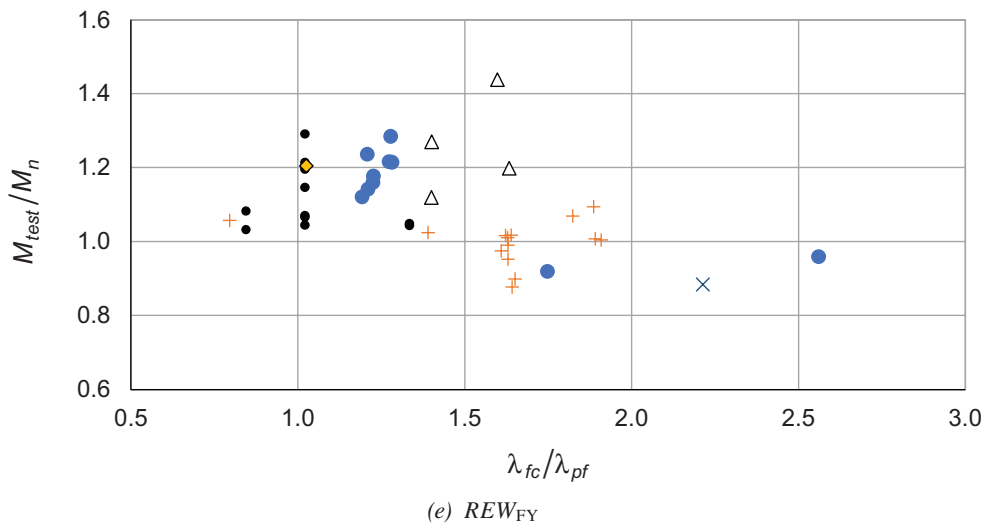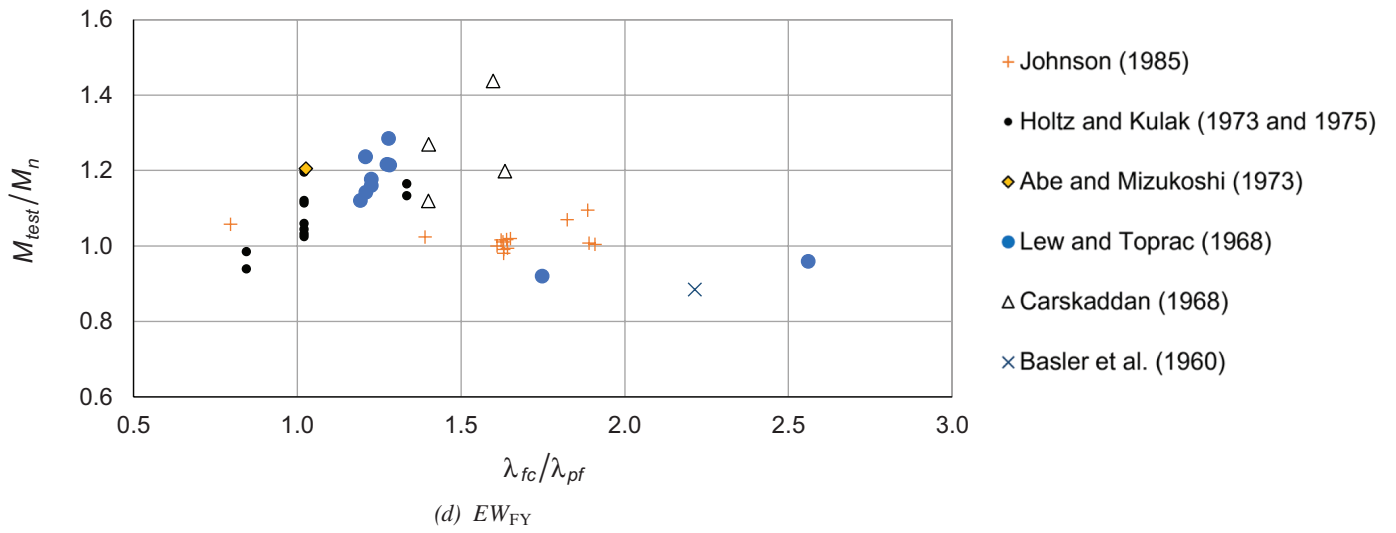
Legend:
+ Johnson (1985)
• Holtz and Kulak (1973 and 1975)
◇ Abe and Mizukoshi (1973)
● Lew and Toprac (1968)
△ Carskaddan (1968)
× Basler et al. (1960)

(d) EW_{FY}

(e) REW_{FY}

(f) EW-LG

Fig. 17 (d,e,f). Comparison of M_{test}/M_n for experimental data versus λ_f/λ_{pf} for all methodologies studied, uniform bending tests.

Figure 18 summarizes the AISC *Specification* and Simplified AISC calculations for a subset of moment gradient tests cataloged previously by White and Kim (2008), as well as a subset of the tests conducted by Righman (2005), Xiong et al. (2016), and Wang et al. (2021), in which the calculated AISC *Specification* flexural strengths are all governed by FLB. In all of these experimental tests, the flanges classify as noncompact according to the AISC *Specification* and the Simplified AISC provisions. The range of $\lambda_{fc}/\lambda_{pf}$ extends only from 1.01 to 1.60 for the data in Figure 18. None of the FLB strength calculations are influenced by moment gradient. Because the wavelength of the flange local buckles is typically small relative to the variation in the moment along the member length, the impact of moment gradient on the FLB resistance is commonly taken to be negligible. Only the calculated LTB resistances are affected. However, as discussed in Deshpande et al. (2021), the web shear

associated with moment gradient, $V = dM/dx$, can influence the web distortion. This in turn may have some impact on the physical FLB resistances. In addition, two of the tests by Schilling (1985), all of the tests by Righman (2005), and one of the tests by Wang et al. (2021) involve singly symmetric I-section members with a smaller flange in compression. The larger depth of the web in compression, combined with the web shear due to the moment gradient, may lead to some challenges in the accurate prediction of the flexural strengths. One practical scenario where the compression flange can be smaller than the tension flange is in composite bridge or building girders, when they are in their noncomposite condition during construction.

All of the tests from Wang et al. (2021), Lew and Toprac (1968), Fahnestock and Sause (1998), and Salem and Sause (2004) considered in Figure 18 entail girders with a measured $F_{yc} > 100$ ksi. The tests by Xiong et al. (2016) focused
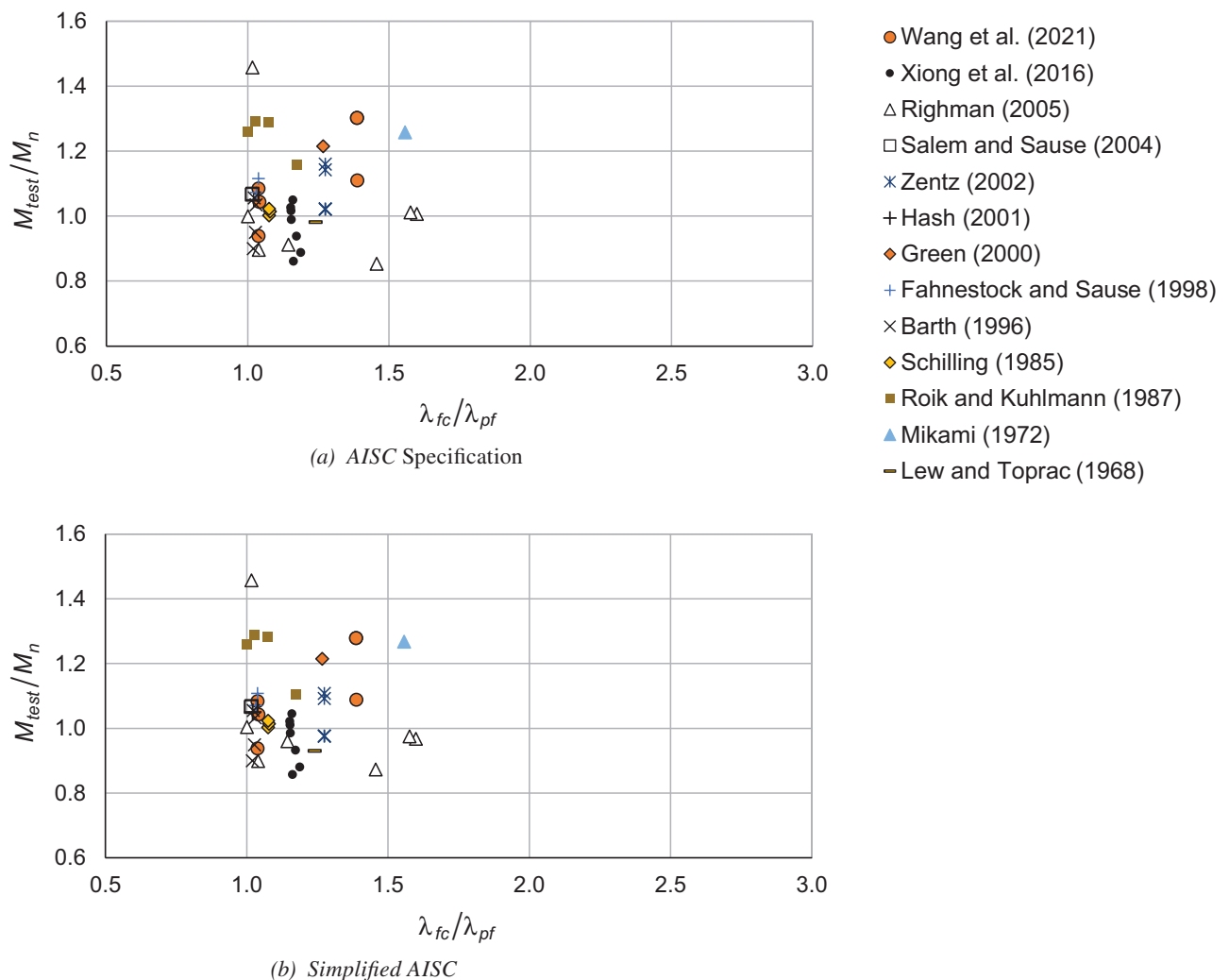

(a) AISC Specification

(b) Simplified AISC

Fig. 18. Comparison of M_{test}/M_n *for experimental data versus* λ_f/λ_{pf} *for the AISC* Specification *and the Simplified AISC methods, moment gradient tests.*

on I-section members with $F_{yc} = 76.1$ ksi, the test by Green (2000) had $F_{yc} = 86.8$, three of Righman's tests had F_{yc} of 88.2 ksi or larger, and all the tests by Zentz (2001) had $F_{yc} = 91.0$ ksi. Therefore, these tests involve a range of high-strength steels.

One can observe that the predictions from the AISC *Specification* and the Simplified AISC procedures are practically the same for the tests in Figure 18. The mean and COV from the AISC *Specification* calculations is 1.07 and 0.13, respectively, versus 1.06 and 0.13 from the Simplified AISC provisions. It should be noted however that while the predictions from these two procedures are nearly identical for these experimental tests, comprised of members with noncompact flanges, the Simplified AISC procedure would tend to mitigate the conservatism of the AISC *Specification* predictions for slender-flange members. Further experimental testing would be appropriate to provide additional verification of the flange local buckling resistance of I-section members having these characteristics.

Three of the smaller professional bias factors, M_{test}/M_n, from the tests conducted by Xiong et al. (2016) correspond to cases in which the physical member clearly failed by LTB rather than FLB. These tests correspond to LTB slenderness values at which the calculated strengths, scaled by C_b, are truncated by the plateau resistance. Several of the smaller M_{test}/M_n values from Righman (2005) have I_{yc}/I_y values close to or violating the limit of 0.23 in Figure 3, combined with relatively large h/t_w values between 84 and 94 (h_c/t_w = between 95 and 107), relatively large LTB slenderness values, and moment gradient loading. However, one of the Righman (2005) tests that had an I_{yc}/I_y less than 0.23 combined with a web with $h/t_w = 33$ and $h_c/t_w = 41$, as well as relatively small LTB slenderness, exhibited the largest M_{test}/M_n shown in Figure 18 ($M_{test}/M_n = 1.46$). Clearly, there are many attributes of the moment gradient tests that can significantly influence the flexural resistances other than the direct evaluation of FLB. However, the scatter band of the M_{test}/M_n calculations from the AISC *Specification* and the Simplified AISC calculations is comparable to that of the LTB results considered in reliability assessments pertaining to the AISC *Specification* (White and Jung, 2008; White and Kim, 2008; Subramanian et al. 2018; Slein et al., 2021). The test results considered in Figures 17 and 18 are evaluated in more detail in Slein et al. (2021).

CONCLUSIONS

Strength predictions from parametric FEA studies as well as measured strengths collected from previous experimental tests on I-section members failing by FLB show that the AISC *Specification* gives highly conservative results for flexural members having a slender compression flange. The methodologies proposed in this paper successfully

mitigate this conservatism by considering the post-buckling strength of slender flanges; however, there are important considerations regarding the efficacy of their use considering their predictions relative to the FEA and experimental test results. These considerations may be summarized as follows:

1. The EW-LG procedure, accounting for slender flange post-buckling strength as well as local–global interaction, gives accurate to conservative predictions in most cases for members with highly slender flanges having 60-ksi and 100-ksi yield strengths. However, comparison with reported experimental strengths shows that it tends to underpredict the strengths for members with intermediate flange slenderness values.

2. The EW, EW_{Fy}, and REW_{Fy} procedures provide adequate predictions for 60-ksi members in the FEA simulation studies, mitigating the conservatism attached with AISC *Specification* predictions for slender-flange members. However, the FEA simulation results show that the predictions for 100-ksi members with slender flanges tend to be slightly unconservative for intermediate unbraced lengths most susceptible to local–global interaction. In addition, several experimental tests of members with yield strengths exceeding 100 ksi show this trend. Although the REW_{Fy} method gave improved predictions in the FEA simulation studies for 60-ksi members, it overpredicts the strengths in a number of experimental tests having compact or noncompact webs.

3. The Simplified AISC procedure provides a straightforward adjustment to the AISC *Specification* calculations for FLB, without requiring the use of flange effective width calculations to account for the post-buckling strength of slender flanges or (in the case of the EW-LG procedure) local–global buckling interactions. This procedure is shown to produce accurate to conservative strength predictions for both the 60-ksi and 10-ksi FEA test simulation cases as well as for experimental tests documented in the literature. The best predictions for this method are obtained with the Simplified AISC-II procedure, which combines the recommended FLB calculations with the use of the LTB strength curve and noncompact web limit parameters recommended by Subramanian et al. (2018) and Subramanian and White (2017b and 2017d).

REFERENCES

Abe, H., and Mizukoshi, N. (1973), "Buckling Tests on Plate Girders under Bending," *Annual Meeting of the Japanese Society of Civil Engineers*, Japan Society of Civil Engineers, Tokyo.

AISC (2016), *Specification for Structural Steel Buildings*, ANSI/AISC 360-16, American Institute of Steel Construction, Chicago, Ill.

ASCE (1971), *Plastic Design in Steel: A Guide and Commentary*, American Society of Civil Engineers, New York, N.Y.

AWS (2020), *Structural Welding Code–Steel*, AWS D1.1:D1.1, American Welding Society, Miami, Fla.

Barth, K.E. (1996), "Moment-Rotation Characteristics for Inelastic Design of Steel Bridge Beams and Girders," Doctoral Dissertation, Department of Civil Engineering, Purdue University, West Lafayette, Ind.

Basler, K., Yen, B., Mueller, J., and Thurlimann, B. (1960), "Web Buckling Tests on Welded Plate Girders," WRC Bulletin No. 64, Welding Research Council, New York, N.Y.

Carskaddan, P. (1968), "The Bending Behavior of Slender-web Girders with A514 Steel Flanges," U.S. Steel Corporation, Applied Research, Report (57.019-904)(5) (AS-EA-23-ps).

CEN (2006), *Eurocode 3: Design of Steel Structures*, 1993-1-5, Comite Européen de Normalisation, Brussels, Belgium.

Cherry, S. (1960), "The Stability of Beams with Buckled Compression Flanges," *Structural Engineering*, Vol. 38, pp. 277–285.

Deshpande, A.M., Kamath, A.M., Slein, R., Sherman, R.J., and White, D.W. (2021), "Built-Up I-Section Member Flexural Resistance: Inelastic C_b Effects from Web Shear Post-Buckling and Early Tension Yielding," SEMM Research Report 21-02, School of Civil and Environmental Engineering, Georgia Institute of Technology, Atlanta, Ga.

Fahnestock, L. and Sause, R. (1998), "Flexural Strength and Ductility of HPS-100W Steel I-Girders," ATLSS Report No. 98-05, Lehigh University, Bethlehem, Pa.

Gerard, L. (2020), "Contribution to the Design of Steel I and H-Sections Members by Means of the Overall Interaction Concept," Doctoral Dissertation, Civil and Water Engineering Department, Laval University, Quebec, Canada.

Green, P.S. (2000), "The Inelastic Behavior of Flexural Members Fabricated from High Performance Steel," Doctoral Dissertation, Department of Civil Engineering, Lehigh University, Bethlehem, Pa.

Hash, J.B. (2001), "Shear Capacity of Hybrid Steel Girders," Master's Thesis, Department of Civil Engineering, University of Nebraska, Neb.

Holtz, N. and Kulak, G. (1973), "Web Slenderness Limits for Compact Beams," Structural Engineering Report No. 43, University of Alberta, Alberta, Canada.

Holtz, N. and Kulak, G. (1975), "Web Slenderness Limits for Noncompact Beams," Structural Engineering Report No. 51, (p. 21). University of Alberta, Alberta, Canada.

Johnson, D. (1985), "An Investigation into the Interaction of Flanges and Webs in Wide Flange Shapes," *Annual Technical Session*, Structural Stability Research Council, pp. 395–405.

Kim, Y.D. (2010), "Behavior and Design of Metal Building Frames Using General Prismatic and Web-Tapered Steel I-Section Members," Doctoral Dissertation, Georgia Institute of Technology, Atlanta, Ga.

Latif, W. (2020), "Flange Local Buckling Resistance and Local-Global Buckling Interaction in Slender-Flange Welded I-Section Beams," MS Thesis, Georgia Institute of Technology, Atlanta, Ga.

Lew, H. and Toprac, A. (1968), "The Static Strength of Hybrid Plate Girders," S.F.R.L. Technical Report P550-11, Structures Fatigue Research Laboratory, Department of Civil Engineering, University of Texas, Austin, Texas.

MBMA (2012), *Metal Building Systems Manual*, Metal Building Manufacturer's Association, Cleveland, Ohio.

Mikami, I. (1972), "Study on Buckling of Thin Walled Girders under Bending," Doctoral Dissertation, Department of Civil Engineering, Nagoya University, Japan (in Japanese).

Peköz, T. (1986), "Development of a Unified Approach to the Design of Cold-Formed Steel Members," Report SG-86-4, American Iron and Steel Institute, Washington, D.C.

Righman, J. (2005), "Rotation Compatibility Approach to Moment Redistribution for Design and Rating of Steel I-Girders," Doctoral Dissertation, School of Civil Engineering, West Virginia University, Morgantown, W.V.

Roik, K. and Kuhlmann, U. (1987), "Rechnerische Ermittlung der Rotationkapazitat biegebeanspruchter I-Profile," *Stahlbau*, Vol. 11, pp. 321–327.

Salem, E.S. and Sause, R. (2004), "Flexural Strength and Ductility of Highway Bridge I-Girders Fabricated from HPS-100W Steel," ATLSS Report No. 04-12.

Schafer, B., Fraser, T., Goel, S., McManus, P., Sherman, D., Sabol, T., Uang, C.-M., Varma, A., and Leu, B. (2020), "Task Group Report on Local Buckling (Width-to-Thickness) Limits," American Institute of Steel Construction, Chicago, Ill.

Schilling, C.G. (1985), "Moment-Rotation Tests of Steel Bridge Girders," Project 188, Autostress Design of Highway Bridges, American Iron and Steel Institute, Washington, D.C.

Seif, M. (2010), "Cross-Section Stability of Structural Steel," Doctoral Dissertation, John Hopkins University, Baltimore, Md.

Seif, M. and Schafer, B. (2010), "Local Buckling of Structural Steel Shapes," *Journal of Constructional Steel Research*, Vol. 66, pp. 1,232–1,247.

Simulia (2013), *ABAQUS/Standard Version 6.13-1*, Simulia, Inc., Providence, R.I.

Slein, R., Phillips, M.L., Sherman, R.J., and White, D.W. (2021), "Assessment of Built-Up I-Section Member Flexural Resistances from Experimental Test Data," SEMM Research Report 21-09, School of Civil and Environmental Engineering, Georgia Institute of Technology, Atlanta, Ga.

Subramanian, L. (2015), "Flexural Resistance of Longitudinally Stiffened Plate," Doctoral Dissertation, Georgia Institute of Technology, Atlanta, Ga.

Subramanian, L.P. and White, D.W. (2017a), "Resolving the Disconnects between Lateral Torsional Buckling Experimental Tests, Test Simulations and Design Strength Equations," *Journal of Constructional Steel Research*, Vol. 128, pp. 321–334.

Subramanian, L. and White, D.W. (2017b), "Reassessment of the Lateral Torsional Buckling Resistance of I-Section Members: Uniform-Moment Studies," *Journal of Structural Engineering*, ASCE, Vol. 143, No. 3, DOI: 10.1061/(ASCE)ST.1943-541X.0001686.

Subramanian, L. and White, D.W. (2017c), "Reassessment of the Lateral Torsional Buckling Resistance of Rolled I-Section Members: Moment Gradient Tests," *Journal of Structural Engineering*, ASCE, Vol. 143, No. 4, DOI: 10.1061/(ASCE)ST.1943-541X.0001687.

Subramanian, L. and White, D.W. (2017d), "Improved Noncompact Web-Slenderness Limit for Steel I-Girders," *Journal of Structural Engineering*, Vol. 143, No. 4, DOI: 10.1061/(ASCE)ST.1943-541X.0001722.

Subramanian, L., Jeong, W.Y., Yellepeddi, R., and White, D.W. (2018), "Assessment of I-Section Member LTB Resistances Considering Experimental Test Data and Practical Inelastic Buckling Design Calculations," *Engineering Journal*, AISC, Vol. 55, No. 1, pp. 15–44.

Toğay, O. (2018), "Advanced Design Evaluation of Planar Steel Frames Composed of General Nonprismatic I-Section Members," Doctoral Dissertation, Georgia Institute of Technology, Atlanta, Ga.

Toğay, O. and White, D.W. (2018), "Toward the Recognition of Unaccounted for Flange Local Buckling and Tension Flange Yielding Resistances in the ANSI/AISC 360 *Specification*," *Proceedings of the Annual Stability Conference Structural Stability Research Council*.

Wang, K., Xiao, M., Chung, K.-F., and Nethercot, D.A. (2021), "Lateral Torsional Buckling of Partially Restrained Beams of High Strength S690 Welded I-Sections," *Journal of Constructional Steel Research*, Vol. 184, DOI: 10.1016/j.jcsr.2021.106777.

White, D.W., Jeong, W., and Slein, R. (2021), *Frame Design Using Nonprismatic Members*, 2nd Ed., Design Guide 25, AISC, Chicago, Ill.

White, D.W. and Jung, S. (2008), "Unified Flexural Resistance Equations for Stability Design of Steel I-Section Members—Uniform Bending Tests," *Journal of Structural Engineering*, Vol. 134, No. 9, pp. 1,450–1,470.

White, D.W. and Kim, Y. (2008), "Unified Flexural Resistance Equations for Stability Design of Steel I-Section Members—Moment Gradient Tests," *Journal of Structural Engineering*, Vol. 134, No. 9, pp. 1,471–1,486.

Winter, G. (1970), *Light Gage Cold-Formed Steel Design Manual: Commentary of the 1968 Edition*, American Iron and Steel Institute, Washington, D.C.

Xiong, G., Kang, S.B., Yang, B., Wang, S., Bai, J., Nie, S., Hu, Y., and Dai, G. (2016), "Experimental and Numerical Studies on Lateral Torsional Buckling of Welded Q460GJ Structural Steel Beams," *Engineering Structures*, Vol. 126, DOI: 10.1016/j.engstruct.2016.07.050.

Zentz, A. (2002), "Experimental Moment-Shear Interaction and TFA Behavior in Hybrid Plate Girders," MS Thesis, University of Missouri, Columbia, Mo.

Cyclic Behavior of DuraFuse Frames Moment Connections

PAUL W. RICHARDS

ABSTRACT

Most special moment frames (SMF) rely on beam yielding to reach drifts of 0.04 rad and beyond. In contrast, DuraFuse Frames (DFF) incorporate a fuse plate that acts as the yielding element. Nine full-scale DFF specimens were tested using AISC 341 (2016b), *Seismic Provisions for Structural Buildings*, Chapter K, to prequalify the DFF connection for use in SMF and inclusion in AISC 358 (2016a), *Prequalified Connections for Special and Intermediate Steel Moment Frames for Seismic Applications*. Eight specimens were tested with the standard protocol and exceeded the qualification criteria. The other specimen completed a custom protocol representing three maximum considered earthquakes (MCE) in sequence. The experiments demonstrated that the stiffness of the DFF connection is sufficient to classify the connection as fully restrained (FR).

Keywords: special moment frame, replaceable fuse, prequalified moment connection, experimental testing, DuraFuse, fully restrained connection.

INTRODUCTION

Steel special moment frames (SMF) are commonly used to resist earthquake effects in high seismic areas. Because SMF are designed with R = 8 (ASCE, 2016), they are expected to operate well in the inelastic range during severe earthquakes. AISC 341, *Seismic Provisions for Structural Steel Buildings*, hereafter referred to as AISC 341 (AISC, 2016b), Section E3.6b, specifies that SMF connections must demonstrate stable performance for drifts up to 0.04 rad.

Most SMF connections rely on beam yielding to provide some or all of the inelastic rotation required to accommodate these large-story drifts. Prequalified connections like the welded unreinforced flange-welded web (WUF-W) and reduced beam section (RBS) rely exclusively on beam yielding, while other connections, like the bolted flange plate (BFP) or double tee, rely on a combination of bolt slip and beam yielding (AISC, 2016b).

There are some drawbacks to relying on beam plastic hinges to achieve ductile SMF. Strict width-to-thickness ratios have to be imposed on the beams, limiting the shapes that can be used (AISC 341, Section D1.1b). Extra lateral bracing is required to keep the beams stable after plastic hinges form (AISC 341, Section D1.2). The portions of the beams subject to inelastic straining need to be designated as protected zones (AISC 341, Section E3.5c). After an earthquake, residual drifts may be locked into the frame by deformed beams. A final drawback of relying on beam plastic hinges is that beam ends may need to be cut out and replaced after a severe earthquake, a challenging proposition that may be economically unfeasible.

DuraFuse Frames (DFF) take a different approach to achieving SMF ductility. Rather than having the beam form a plastic hinge, DFF connections incorporate a fuse plate that acts as the yielding element (UES, 2020).

Figure 1 shows one-sided DFF connections for I-shaped or HSS/box columns. Two-sided and biaxial DFF connections (not shown in Figure 1) are also permitted. For I-shaped columns, the column has cover plates on each side that are fillet welded to the column flanges, as shown in Figure 1(a). For box or HSS columns, the sides of the column may function as the cover plates, as shown in Figure 1(c). Four external continuity plates that extend past the face of the column are fillet welded to the column cover plates or side. The column has a shear tab, with horizontal slotted holes, that is fillet welded to the column face. The beam web, with standard holes, is attached to the shear tab with pretensioned bolts. The beam flanges are attached to the external continuity plates via top plates (top flange) and a fuse plate (bottom flange) (Figure 1). The fuse plate is proportioned such that certain regions of the plate experience shear yielding when the connection is subjected to severe earthquake loading [Figure 1(b)]. The fuse plate is bolted so that it could be removed and replaced following a severe earthquake. The top plates are intended to experience minimal yielding, such that they would not require repair following a severe earthquake. The various plates in the connection are proportioned such that the beam remains essentially elastic.

Several experimental studies have been performed to investigate the behavior of DFF connections subjected to

Paul W. Richards, Vice President of Research and Development, DuraFuse Frames, West Jordan, Utah. Email: paul.richards@durafuseframes.com

cyclic loads. Richards and Oh (2019) performed testing on reduced-scale DFF specimens that demonstrated good potential for the system. Richards (2019, 2021) reported other series of tests with full-scale DFF connections.

Additional testing was performed at the University of California–San Diego (UCSD) to prequalify the DFF connection for use in SMF (Reynolds and Uang, 2019a, 2019b). This paper presents results from nine full-scale DFF specimens that were tested at UCSD. The experiments will be described, and the results will be discussed in the context of AISC 341 criteria for SMF connections.

EXPERIMENTAL TESTING

Test Setup

The overall test setup and specimen geometry are shown in Figure 2. The specimens represented SMF subassemblies with one beam framing into the column (strong axis). The specimens were tested with the column vertical and the beam cantilevering out. To simulate inflection points, the ends of the specimen column were mounted on short sections of W14×257 positioned to experience weak-axis bending. For all specimens, the distance between column supports was 16 ft. For Series E, F, and G, the distance from the column centerline to the actuator line of action was 15.5 ft, while for Series H the distance was 20.5 ft [Figure 2(a)]. A corbel was bolted to the "free" end of the beam and attached to one end of a servo-controlled actuator. The other end of the actuator was mounted to the strong floor. Out-of-plane restraint was provided at the actuator location on both sides of the corbel [Figure 2(b)]. No lateral restraint was provided near the connection or at any other location along the length of the beam.

Connection Details

Four series of tests were performed (E, F, G, H), each with unique beam and column sizes. Table 1 provides beam size, column size, bolt size, and plate thicknesses for each series. Two tests were performed in the E, F, and G series, and three tests were performed in the H series, resulting in a total of nine tests (Table 1).

For each series, the beam size, column size, and connection plate thicknesses were constant (Table 1). Beam sizes ranged from W21 to W40, and beam weight ranged from 50 to 232 lb/ft. Wide-flange column sizes ranged from W14 to W36, and the box column for the H series was 24 in. deep. Fuse plate thicknesses ranged from 0.625 to 1.75 in., and cover plate thicknesses ranged from 0.375 to 0.875 in.

A variety of considerations influenced the beam sizes used in the study. The W36×232 was the strongest W36 beam that could be tested using the equipment/test setup available at the time without the beam length becoming excessive relative to common practice. The W40×167 beam was the strongest W40 beam that could be tested at the time with a 15.5-ft half-span length. The W36×232 and W40×167 had different flange widths that influenced the fuse plate geometry, so both were of interest. The W30×99 had a flange width-to-thickness ratio beyond λ_{hd}, to investigate relaxed width-to-thickness requirements. The W21×50, with a 15.5-ft unbraced length, was included to investigate relaxed lateral bracing requirements (this beam usually requires lateral bracing every 5.4 ft, per AISC 341, Section D1.2b). The four beam sizes used for the UCSD testing complimented beam sizes that had been used in previous DFF studies (W36×150, W33×152, W27×84, W14×38) (Richards, 2019; Richards, 2021; Richards and Oh, 2019).

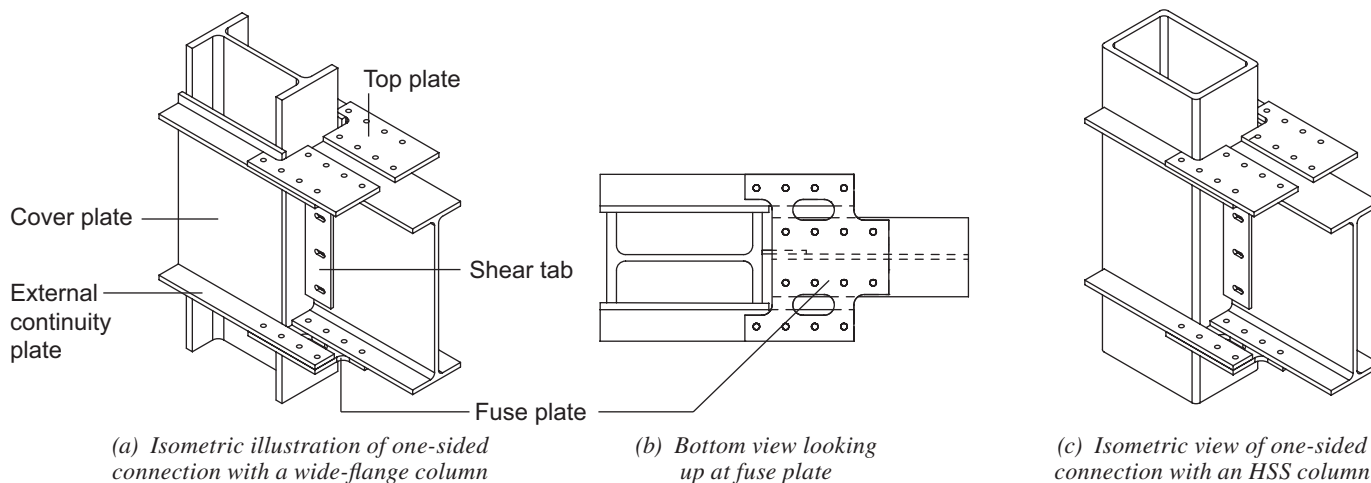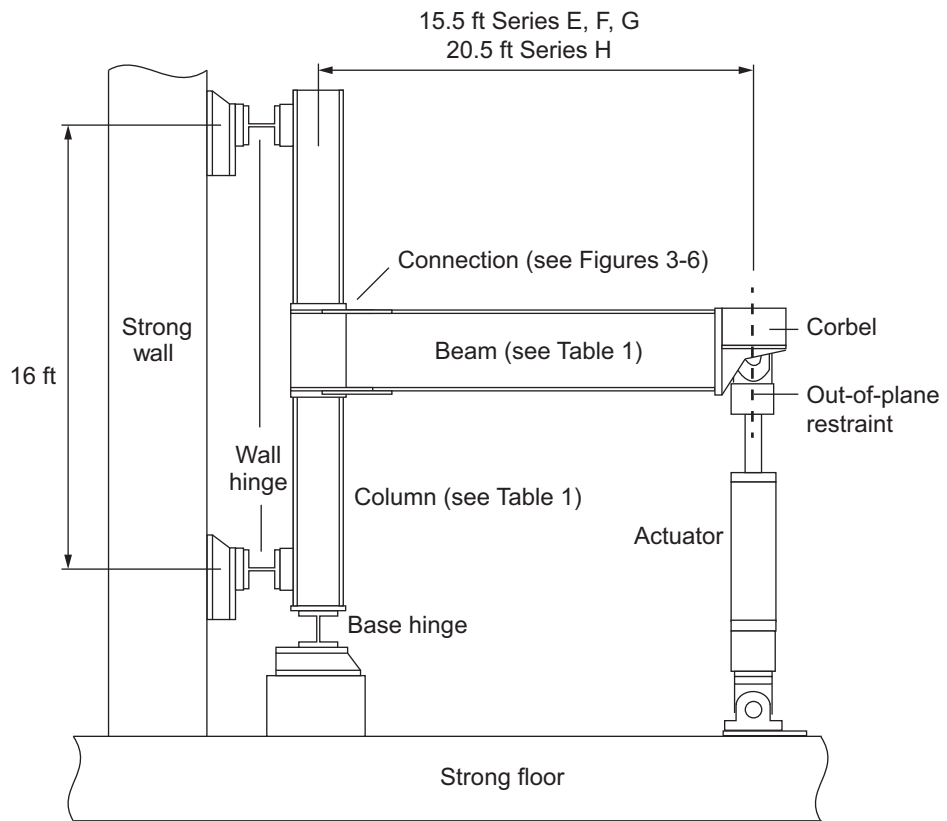The columns were selected to match the beam strengths, investigate torsional issues, and prequalify DFF

(a) Isometric illustration of one-sided connection with a wide-flange column

(b) Bottom view looking up at fuse plate

(c) Isometric view of one-sided connection with an HSS column

Fig. 1. DuraFuse Frames connection for SMF.

(a) Schematic with dimensions

(b) Installed specimen (G1.1) and out-of-plane restraint at actuator

Fig. 2. Experiment test setup.

Table 1. Member, Plate, and Bolt Sizes							
Series	Specimens	Beam	Column	Fuse Thickness (in.)	Cover Plate Thickness (in.)	Bolt Size (in.)	Bolt Grade (ASTM F3125)
E	E1.1	W30×99	W21×132	0.75	0.625	1	F2280
	E1.2						
F	F1.1	W40×167	W36×231	1.25	0.875	1.125	F2280
	F1.2						
G	G1.1	W21×50	W14×68	0.625	0.375	0.875	F1852
	G1.2						
H	H1.1	W36×232	BOX24×17½×1¾	1.75	1.75[a]	1.25	A490
	H1.2						
	H1.3						
[a] The sides of the box column functioned as the cover plates for the H series.							

connections for HSS/box column configurations. In each series, the column had a plastic section modulus that was similar but higher than the beam such that it satisfied the strong column–weak beam criterion. The W36 column for the F series was included to investigate the effects of very deep columns, even though previous DFF testing with W36 columns had not indicated any torsional issues (Richards, 2021). The box column in the H-series investigated DFF configurations that do not require column cover plates [Figure 1(c)].

The details for each series are communicated in Figures 3 through 5. The H-series, with box columns, had a similar detail to the others, the only difference being that the box column did not require additional cover plates because the sides of the box column could function in that capacity (Figure 5).

Material Properties

The wide-flange beams and columns were ASTM A992 (ASTM, 2015b) steel while the plates and bars were ASTM A572 Gr. 50 (ASTM, 2015a). Material properties for the various steel components were determined from independent testing (American Metallurgical Services) as reported in Table 2.

Beam strength considerations were different for the DFF connections, as compared to other prequalified SMF connections, because the DFF beams were not designed to yield. From Table 2, some of the beam flanges had strength beyond R_yF_y (Series E and G), while other were at R_yF_y (Series F), or below R_yF_y (Series H) (see Table 2). Because the fuse plates were proportioned to preclude beam yielding,

assuming a beam strength of only F_y, the same performance was expected regardless of beam strength beyond that.

Material for the fuse plates was selected to represent a conservative case from the standpoint of ductility and maximum force delivered to the connection. A572 Gr. 50 material with a high yield point was selected for the fuses because such material generally has lower toughness and ductility. The DFF design criteria prohibits the use of A572 Gr. 50 material with tensile strength greater than 85 ksi (UES, 2020). The fuse plates with relatively high strength (Table 2) also represented the critical case with regards to the maximum force that would be delivered to bolts, welds, and the other connection plates. Material for the other A572 Gr. 50 connection plates was intentionally selected to be as weak as could be acquired (Table 2) to represent a critical combination.

Fabrication

The plate components, including the fuse plates, were cut with a Kinetic K5200XMC plasma cutter. The specification for DFF states that "roughness of all thermal cut surface shall be no greater than an ANSI surface roughness of 1000 micro-in." and "roughness exceeding this value or gouges not more than ³⁄₁₆ in. shall be removed by machining and grinding." However, to test poor fabrication of the fuse, gouges were introduced at the critical locations on each of the fuse plates and not ground smooth. The depth of the gouges was ⅛ in.

Bolt holes in the beams were drilled, while bolt holes in the external continuity plates, top plates, and fuse plates were either drilled or plasma cut. The method of bolt hole
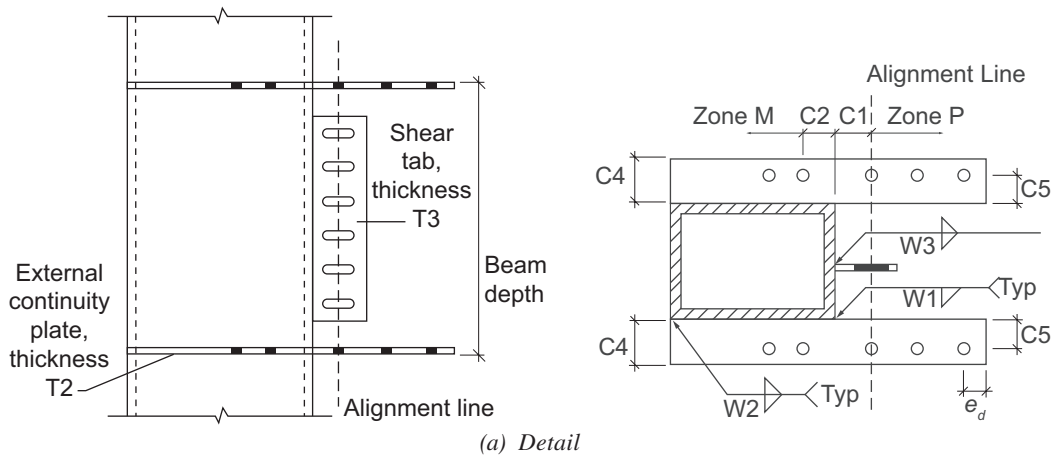
(a) Detail
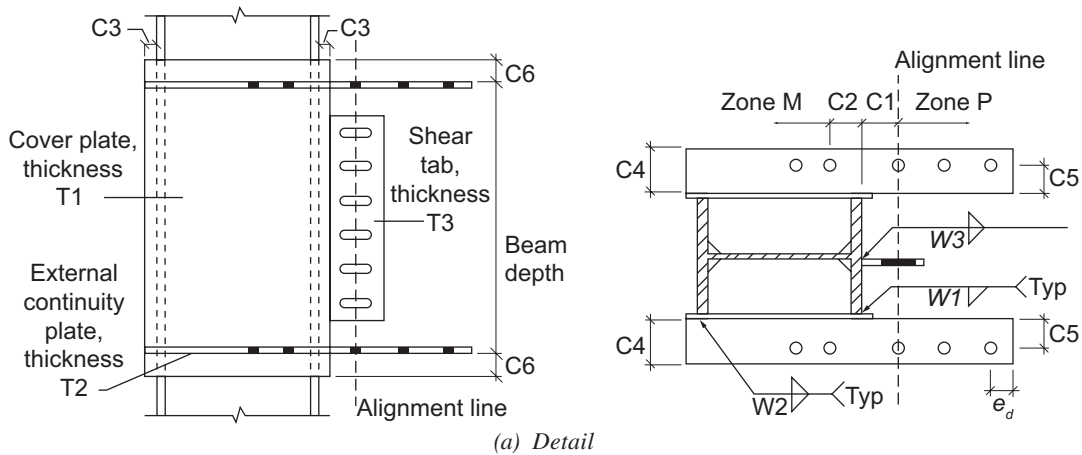
Specimens	Plate Thickness (in.)			Dimensions (in.)						Weld Sizes (in.)		
	T1	**T2**	**T3**	**C1**	**C2**	**C3**	**C4**	**C5**	**C6**	**W1**	**W2**	**W3**
E1.1 E1.2	0.625	0.75	0.5	3.75	5	1	4.75	3	3	⁹⁄₁₆	³⁄₈	³⁄₈
F1.1 F1.2	0.875	1.25	0.625	4.75	1.25	1	5	3	3	⁵⁄₈	³⁄₈	⁷⁄₁₆
G1.1 G1.2	0.375	0.625	0.5	2.875	1	1	3.5	2.313	3	⁷⁄₁₆	¼	⁵⁄₁₆
Note: See Figure 5 for bolt quantities and spacing.												

(b) Schedule

Fig. 3. Connection details for Series E, F, and G.

(a) Detail

Specimens	Plate Thickness (in.)		Dimensions (in.)			Weld Sizes (in.)	
	T2	**T3**	**C1 + C2**	**C4**	**C5**	**W2**	**W3**
H1.1	1.75	0.875	3.75	5.25	3.5	¾	½
H1.2 H1.3	1.75	0.875	3.75	6.125	3.5	1	½
Notes: See Figure 5 for bolt quantity and spacing.							

(b) Schedule

Fig. 4. Connection details for Series H.

(a) Detail
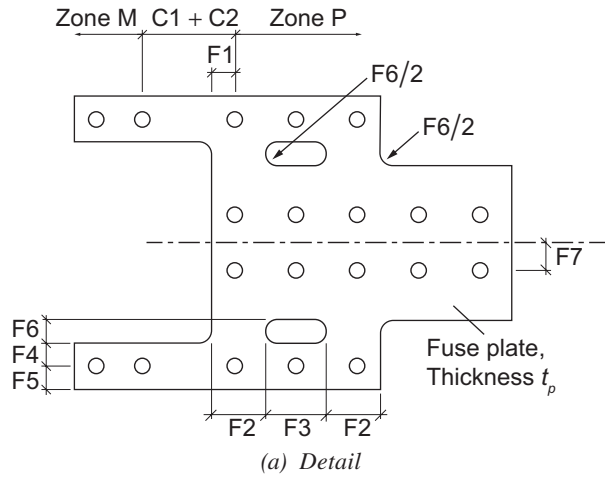
Specimen	Dimensions (in.)									Bolts	
	F1	F2	F3	F4	F5	F6	F7	C1 + C2	Bolt Spacing	P	M
E1.1	2	3.125	6.25	2	1.375	2.5	2.75	8.75	3	4	2
E1.2	2	3.375	5.75	2	1.375	3	2.75	8.75	3	4	2
F1.1	2	3.5	6.625	2.125	2	3.5	2.75	6	3.375	4	3
F1.2	2	3.6875	6.25	2.125	2	4	2.75	6	3.375	4	3
G1.1	1.5	1.875	4.5	1.375	1.1875	1.5	1.75	3.875	2.625	3	2
G1.2	1.5	1.875	4.5	1.375	1.1875	1.5	1.75	3.875	2.625	3	2
H1.1	2.25	3.3125	8.625	2.375	2.25	3	2.75	3.75	3.75	4	4
H1.2	2.25	3.3125	8.625	2.375	2.25	3	2.75	3.75	3.75	4	4
H1.3	2.25	3.5	8.25	2.375	2.25	4	2.75	3.75	3.75	4	4

(b) Schedule

Fig. 5. Fuse plate dimensions.

Table 2. Material Properties					
Series	Component	Steel Grade	Yield Strength (ksi)	Tensile Strength (ksi)	Elongation (%)
E	Beam flange	A992	60.5	76	28
	Column flange	A992	52	78.5	28
	Fuse plate	A572 Gr. 50	58.3	84	29
	Cover plate	A572 Gr. 50	54	73.5	36.5
	Other plates	A572 Gr. 50	51.8	73.3	32.5
F	Beam flange	A992	55.5	74.5	33
	Column flange	A992	62	82	29
	Fuse plate	A572 Gr. 50	57.3	83.5	28
	Cover plate	A572 Gr. 50	(55)[a]	(77.8)[a]	(24)[a]
	Other plates	A572 Gr. 50	57.3	83.5	28
G	Beam flange	A992	60.5	78.5	33
	Column flange	A992	57	75.5	28
	Fuse plate	A572 Gr. 50	58	83.3	33.5
	Cover plate	A572 Gr. 50	59.3	75	33.5
	Other plates	A572 Gr. 50	54	73.5	36.5
H	Beam flange	A992	52.5	74	30
	Column flange	A992	52.5	79.8	29
	Fuse plate	A572 Gr. 50	54	83.3	28
	Cover plate	A572 Gr. 50	52.5	79.8	29
	Other plates	A572 Gr. 50	52.5	79.8	29

[a] Values in parentheses were from mill reports; all others were determined from independent testing.

creation was not found to have any impact on test results.

All of the welds were produced in the shop in the flat position. The same electrode, Lincoln UltraCore 70C, AWS D1.8 (AWS, 2016) compliant, was used for all welds.

Bolting

A variety of bolt sizes, ASTM F3125 (ASTM, 2019) grades, and tightening methods were used. Bolts sizes ranged from 0.875 to 1.25 in. and are indicated in Table 1. Series E and F used Gr. F2280 bolts, Series G used Gr. F1852 bolts, and Series H used Gr. A490 bolts. For series E, F, and G, the bolts were pretensioned with a twist-off tool. For series H, the bolts were pretensioned using the turn-of-the-nut method. All of the bolt installations were performed in the laboratory. The grade of bolt, or bolt tightening method, was not found to have any impact on test results.

The E series investigated the impact of closing gaps with or without shims. For Specimen E1.1, there was a ³⁄₁₆-in. gap between the west top plate and external continuity plates during loose fit-up. That gap was closed without shim plates during bolt tightening. For Specimen E1.2, similar gaps were present between the top plate and external continuity plates and between the fuse plate and external continuity plates. Finger shims were used in the gaps prior to bolt tightening. The similar response of E1.1 and E1.2 indicated that finger shimming had negligible impact on behavior.

Loading Protocol and Instrumentation

The standard loading protocol specified in AISC 341, Section K2.4b (2016b), was used for all but one of the tests. The specified loading was six cycles at 0.00375-rad story drift, followed by six cycles at 0.005 rad, six cycles at 0.0075 rad, four cycles at 0.01 rad, two cycles at 0.015 rad, two cycles at 0.02 rad, two cycles at 0.03 rad, two cycles at 0.04 rad, and two additional cycles at each 0.01-rad increment up to failure. The actuator displacement corresponding to each drift level was calculated by multiplying the target rotation by the distance from the column centerline to the actuator line of action (see Figure 2).

For the first test in each series, the loading protocol was applied through the 0.04-rad drift cycles. Then, testing was stopped, the fuse plates (and bolts) were replaced, and another test was started. The last test in each series was continued all the way until fuse plate tearing occurred.

Conservative adjustments to the standard protocol were made at some points. For all the specimens tested with the standard protocol, the target displacement for the 0.04-rad cycles was increased from 0.001 to 0.003 rad to ensure that the inelastic rotation was at least 0.03 rad during those cycles. This was done because some qualification criteria are based on inelastic rotation rather than story drift. The other conservative deviations from the standard protocol occurred during F1.2 tests. During the first 0.05-rad cycle, an actuator control issue resulted in a larger-than-intended displacement of 0.068 rad.

Specimen H1.2 was the one specimen tested with a non-standard protocol. The protocol was developed by performing nonlinear response history analysis (RHA) on the moment frame in Section 4.3 of the *Seismic Design Manual* (AISC, 2018). RHA was performed using the 1994 Northridge (Beverly Hills–14145 Mulhol), 1989 Loma Prieta (Capitola), and 1995 Kobe (Shin-Osaka) records. The records were scaled to the maximum considered earthquake (MCE) level. The third-story drifts in the example building were the largest and were used for the protocol. The significant drift cycles from the Northridge, Loma Prieta, and Kobe responses were combined to form the protocol shown in Figure 6. The protocol has over 50 cycles and represents demands from three MCE events applied in sequence.

EXPERIMENTAL RESULTS

Observed Response

The observed response of Specimen E1.2 will be discussed in some detail because it was representative of the other specimens. Figure 7 shows photos of E1.2 at different stages of testing. The specimen appeared to remain elastic throughout the 0.00375-, 0.005-, 0.0075-rad cycles. During the 0.01-rad cycles, slight flaking of the mill scale indicated localized yielding in the yield regions [Figure 7(a)]. Bolt slip occurred during the 0.015-rad and subsequent cycles. During the 0.02-, 0.03-, and 0.04-rad cycles, inelastic

deformations of the fuse plate became more pronounced [Figure 7(c)–(e)]. The external continuity plates had noticeable curvature at 0.05-rad drift [Figure 7(f)] but were still primarily elastic (the plates were essentially straight after testing). During the second cycle at 0.06 rad, ductile tearing of the fuse plate initiated [Figure 7(g)], and during the first excursion to 0.07 rad, the west side of the fuse plate tore through [Figure 7(h)].

The other specimens had similar observed response, with localized yielding occurring around 0.01 rad, followed by bolt slip, significant fuse plate yielding (for drifts beyond 0.02 rad), and eventually fuse plate tearing. Figure 8 shows photos from each series at 0.05 rad.

Table 3 summarizes the cycles that were completed by each specimen. The first specimen in each series was only tested to 0.04 rad so that the fuse plates could be replaced to demonstrate repairability. Specimens E1.2, G1.2, and H1.3 all completed cycles at 0.06 rad. Specimen F1.2 completed two cycles at 0.05 rad; however, one of them included an unintended excursion to 0.068 rad. In general, the cyclic rotation capacity was greater for the shallower beams because the strains in the fuse plates were proportional to the beam depth.

While incidental yielding was observed in various elements, significant inelastic deformations were confined to the fuse plates. Minor yielding of the reentrant corner of the top plates occurred for all the specimens (Reynolds and Uang, 2019a), but the top plates did not require replacement. The same top plates were used for multiple tests in Series F, G, and H. For the F series, minor flaking of the mill scale was observed in the proximity of the beam flange bolt holes and in the shear tab plate. Overall, however, the beams, columns, and panel zones remained essentially elastic throughout testing (Figure 8).

Specimen H1.2 was tested with a nonstandard protocol. The customized protocol reflected demands from three MCE events applied in sequence. Specimen H1.2 exhibited fuse yielding and bolt slip during testing, but no tearing in the fuse, and no significant yielding in other components.
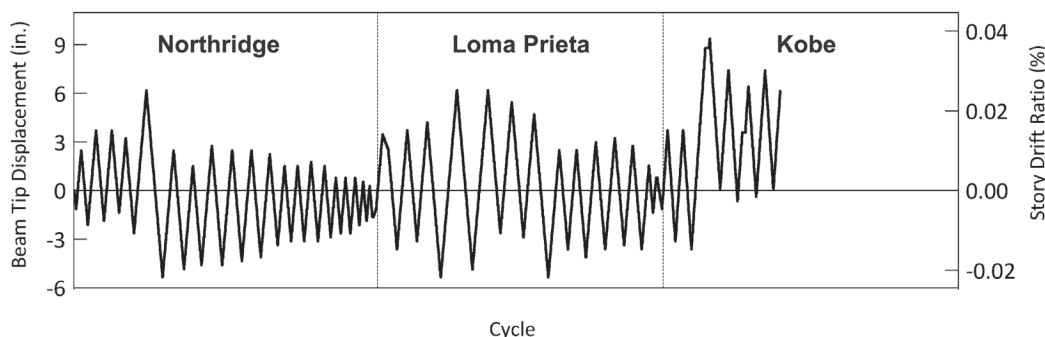

Fig. 6. Nonstandard protocol representing three MCE events applied sequentially.

(a) 0.01 rad

(b) 0.015 rad

(c) 0.02 rad

(d) 0.03 rad

(e) 0.04 rad

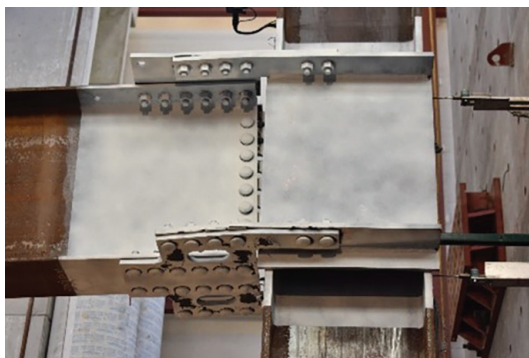*(f) 0.05 rad*

(g) 0.06 rad

(h) 0.07 rad

Fig. 7. Connection behavior at various cycles of loading, E1.2 shown.

Table 3. Cycles Completed and Maximum Applied Force for Each Specimen			
Specimen	Beam	Cycles Completed [rad (number of cycles)]	Maximum Actuator Force (kips)
E1.1	W30×99	0.04 (2)[a]	80.8
E1.2		0.06 (2)	91.8
F1.1	W40×167	0.04 (2)[a]	206
F1.2		0.05 (2)[b]	225
G1.1	W21×50	0.04 (1)[a]	30.3
G1.2		0.06 (2)	33.5
H1.1	W36×232	0.04 (2)	179
H1.2		—[c]	177
H1.3		0.06 (1)	225

[a] The first test in each series was stopped after 0.04 rad so that the fuse plate could be replaced to demonstrate repairability.
[b] Due to an actuator control problem, F1.2 was pushed to 0.068 rad during the first 0.05-rad cycle.
[c] Specimen H1.2 was tested with a nonstandard protocol with unsymmetric cycles.

(a) E1.2

(b) F1.2

(c) G1.2

(d) H1.3

Fig. 8. Specimens from each series at 0.05 rad.

Measured Response

The hysteretic behavior of the DFF connections is shown in Figure 9, where the moment at the column face is plotted versus the story drift for each of the specimens. The moment at the column face was calculated as the actuator load multiplied by the distance from the actuator line of action to the column face. The moment at the column face was normalized by the nominal plastic moment of the beam, M_{pn}, on the right side of each plot. Horizontal dashed lines were added at $0.8M_p$, which is the strength degradation threshold when determining rotation capacity (AISC, 2016b). The drift was calculated as the displacement at the actuator line of action divided by the distance from the actuator line of action to the centerline of the column. Vertical dashed lines were added to the plots at 0.04-rad drift, which is the qualification criteria for special moment frames (AISC, 2016b).

Hysteretic response of the DFF connections was similar to other bolted SMF connections, except there was no strength degradation at large drifts. As with other bolted SMF connections (Sato et al., 2008), the DFF hysteretic plots had a flatter region in the middle of each large cycle corresponding to bolt slip (Figure 9). Once bolts returned to bearing, the strength continued to climb. One difference, as compared to other bolted SMF connections, was the lack of strength degradation at large drifts. SMF connections that form plastic hinges in the beam have strength degradation after 0.03 or 0.04 rad due to flange and web local buckling of the beam in the plastic hinge region (Uang and Fan, 2001). The DFF connections did not have flange local buckling or local buckling in the fuse plate, and maintained strength through large drift cycles until the fuse plates fatigued.

The hysteretic response of H1.2 (Figure 10) was consistent with H1.1 and H1.3 tested with the standard protocol. The nonsymmetric hysteretic plot for H1.2 would fit within in the envelopes of the H1.1 or H1.3 responses [comparing Figure 10 with Figure 9(g), (h)].

Connection Stiffness

Experimental results were used to quantify the stiffness of the DFF connections. During testing, the actuator force, F, and beam displacement, δ, were recorded. For the elastic cycles, the beam displacement was the sum of the displacement effects caused by beam deformations, δ_b, column deformations, δ_c, panel zone deformations, δ_{pz}, and connection deformations, δ_{con}.

$$\delta = \delta_b + \delta_c + \delta_{pz} + \delta_{con} \qquad (1)$$

Displacement effects from connection deformations, δ_{con}, were determined by subtracting beam, column, and panel zone displacement effects from the total measured displacement (rearranging Equation 1). The total deformation was taken from the first peak at 0.00375 rad. Beam and

column deformation effects, δ_b and δ_c, were determined using Timoshenko beam theory and the measured applied force on the beam, F, and the calculated reaction forces on the column. Panel zone deformation effects, δ_{pz}, were computed by multiplying the measured panel zone shear deformation by the distance from the column face to the actuator. With δ, δ_b, δ_c, and δ_{pz} all known, δ_{con} was calculated from Equation 1. Table 4 summarizes values of δ, δ_b, δ_c, δ_{pz}, and δ_{con} from the initial 0.00375-rad cycle for the first test in each series.

An effective spring stiffness was calculated for the connections as:

$$K_S = \frac{M}{\theta} = \frac{Fg}{\left(\dfrac{\delta_{con}}{g}\right)} \qquad (2)$$

where g was the distance from the actuator line of action to the face of the column. Calculated values for K_s are summarized in Table 5.

Moment frame connections are considered fully restrained (FR) for design purposes if the connection stiffness is large relative to the flexural stiffness (EI/L) of the beam. In AISC 358, *Prequalified Connections for Special and Intermediate Steel Moment Frames for Seismic Applications,* Chapter 13 Commentary (2016a), a minimum stiffness of $18EI/L$ is discussed. In AISC 360, *Specification for Structural Steel Buildings*, Section B3 Commentary (2016c), $20EI/L$ is discussed as a level of acceptability. Relative to these specifications, the normalized values of K_s shown in the last column of Table 5 were sufficient to classify the DFF connection as FR.

SUMMARY AND CONCLUSIONS

Connections in steel special moment frames (SMF) must be capable of accommodating large story drifts without excessive strength deterioration. Most SMF connections rely on beam yielding to achieve large inelastic rotations. In contrast, DuraFuse Frames (DFF) moment connections are designed so that yielding occurs in a fuse plate, making DFF SMF easier to repair after severe earthquakes. As part of the prequalification for DFF connections, full-scale testing was conducted in accordance with AISC 341, Chapter K. Nine specimens were tested at UCSD, with beam sizes of W21×50, W30×99, W36×232, and W40×167.

The experiment results support the following conclusions:

- The eight specimens that were tested with the standard protocol all met the AISC 341 acceptance criteria by completing at least one cycle at 0.04 rad without strength degradation below $0.8M_{pn}$.

- The series with W21×50 and W30×99 beams completed two cycles at 0.06 rad prior to fuse tearing. The heaviest
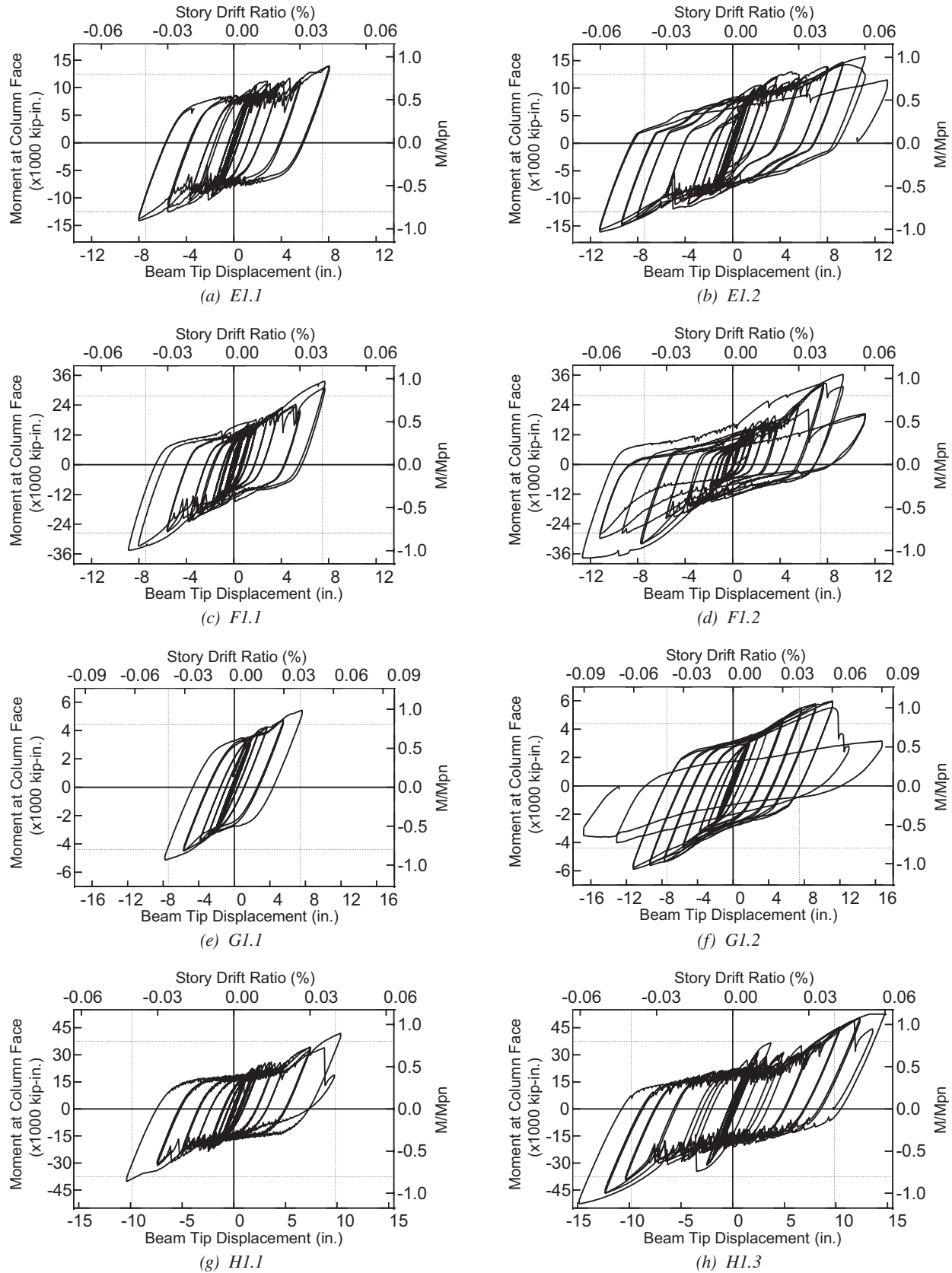
Fig. 9. Hysteretic response for the DFF specimens tested with standard protocol.

Table 4. Deformation Effects from First Elastic Cycle at 0.00375 Rad						
Specimen	F (kips)	δ (in.)	δ_b (in.)	δ_c (in.)	δ_{pz} (in.)	δ_{con} (in.)
E1.1	28.7	0.726	0.477	0.132	0.0797	0.0387
F1.1	36.1	0.312	0.191	0.0398	0.0671	0.0137
G1.1	10.0	1.07	0.694	0.214	0.0805	0.0810
H1.1	55.0	0.865	0.581	0.123	0.0751	0.0852

Table 5. Effective Stiffness of DFF Connections						
Specimen	Beam	I (in.^{4})	L[a] (in.)	$\dfrac{EI}{L}$ (kip-in.)	K_s (kip-in./rad)	$\dfrac{K_s}{EI/L}$
E1.1	W30×99	3,990	372	311,000	22,700,000	73
F1.1	W40×167	11,600	372	904,000	74,000,000	82
G1.1	W21×50	984	372	76,700	3,960,000	52
H1.1	W36×232	15,000	492	884,000	35,400,000	40
[a] Bay width of the prototype frame.						
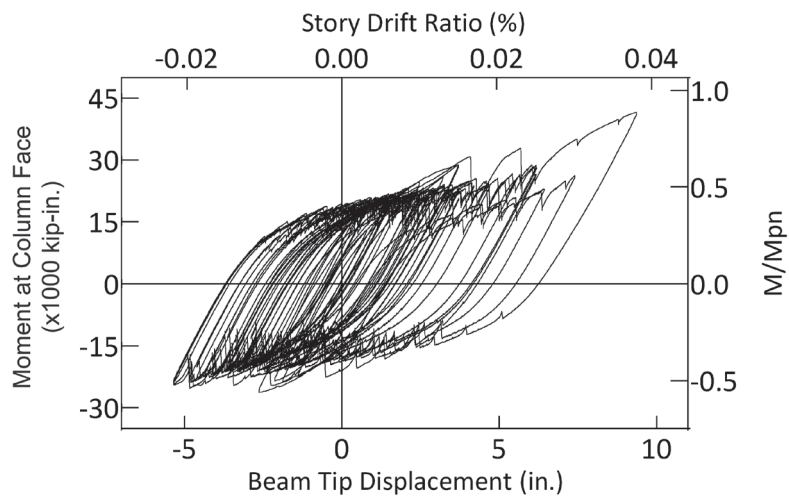
Fig. 10. Hysteretic response of H1.2, tested with alternative loading protocol.

series, with a W36×232 beam, completed one cycle at 0.06 rad prior to fuse tearing.

- Testing under an earthquake-specific protocol demonstrated that DFF fuse plates can withstand multiple MCE events in sequence without requiring replacement.

- DFF connections were found to be fully restrained (FR) with the experimentally determined connection stiffness exceeding $20EI/L$ for the full range of sizes.

- DFF connections did not experience strength degradation at large drifts since beam local buckling was prevented. Fuse plates maintained their strength until ductile tearing occurred.

- DFF connections were repaired by replacing the bottom fuse plate. Repeatable performance was demonstrated after fuse plates were replaced. Fuse yielding for drifts up to 0.02 rad was localized and would not necessitate fuse replacement.

REFERENCES

AISC (2016a), *Prequalified Connections for Special and Intermediate Steel Moment Frames for Seismic Applications,* ANSI/AISC 358-16, American Institute of Steel Construction, Chicago, Ill.

AISC (2016b), *Seismic Provisions for Structural Steel Buildings,* ANSI/AISC 341-16, American Institute of Steel Construction, Chicago, Ill.

AISC (2016c), *Specification for Structural Steel Buildings,* ANSI/AISC 360-16, American Institute of Steel Construction, Chicago, Ill.

AISC (2018), *Seismic Design Manual*, 3rd Ed., American Institute of Steel Construction, Chicago, Ill.

ASCE (2016), *Minimum Design Loads and Associated Criteria for Buildings Structures,* ASCE/SEI 7-16, American Society of Civil Engineers, Reston, Va.

ASTM (2015a), *Standard Specification for High-Strength Low-Alloy Columbium-Vanadium Structural Steel*, A572/A572M, ASTM International, West Conshohocken, Pa.

ASTM (2015b), *Standard Specification for Structural Steel Shapes*, A992/A992M, ASTM International, West Conshohocken, Pa.

ASTM (2019), *Standard Specification for High-Strength Structural Bolts and Assemblies, Steel and Alloy Steel, Heat Treated, 120 ksi (830 MPa) and 150 ksi (1040 MPa) Minimum Tensile Strength, Inch and Metric Dimensions*, F3125/F3125M, ASTM International, West Conshohocken, Pa.

AWS (2016), *Structural Welding Code—Seismic Supplement*, D1.8/D1.8M, American Welding Society, Miami, Fla.

Reynolds, M. and Uang, C.-M. (2019a), *Cyclic Testing of DuraFuse (DF) Moment Frame Connections for SMF and IMF Applications: Series E, F, and G Specimens*, TR19-01, University of California San Diego, La Jolla, Calif.

Reynolds, M. and Uang, C.-M. (2019b), *Cyclic Testing of DuraFuse (DF) Moment Frame Connections for SMF and IMF Applications: Series H Specimens*, TR19-02, University of California San Diego, La Jolla, Calif.

Richards, P.W. (2019), "A Repairable Connection for Earthquake-Resisting Moment Frames," *Steel Construction*, Vol. 12, No. 3, pp. 191–197.

Richards, P.W. (2021), "Cyclic Hardening Factor for Replaceable Shear Fuse Connections," *Journal of Constructional Steel Research*, Vol. 185, 106838.

Richards, P.W. and Oh, S.S. (2019), "Cyclic Behavior of Replaceable Shear Fuse Connections for Steel Moment Frames," *Journal of Structural Engineering*, Vol. 145, No. 12, 04019156.

Sato, A., D. Newell, J., and Uang, C.-M. (2008), "Cyclic Behavior and Seismic Design of Bolted Flange Plate Steel Moment Connections," *Engineering Journal*, AISC, Vol. 45, pp. 221–232.

Uang, C. and Fan, C. (2001), "Cyclic Stability Criteria for Steel Moment Connections with Reduced Beam Section," *Journal of Structural Engineering*, Vol. 127, No. 9, pp. 1021–1027.

UES (2020), *DuraFuse Frames Technology*, UES ER-610, IAPMO Uniform Evaluation Services, Ontario, Calif.

Steel Structures Research Update

Inelastic Design Method for Steel Buildings Subjected to Wind Loads

JUDY LIU

INTRODUCTION

Ongoing research on an inelastic wind design method for steel buildings is highlighted. This study is under way at Brigham Young University, led by Dr. Johnn Judd, Assistant Professor in the Department of Civil and Construction Engineering. Dr. Judd's research interests include seismic performance of steel moment frame buildings, field evaluation and structural health monitoring of steel bridges, and wind performance assessment of buildings. Dr. Judd has also been awarded the AISC Milek Fellowship for this research on inelastic design methods for steel buildings subjected to wind loads. The research team is in the third year of the four-year study. Selected results from the study are highlighted along with a preview of future work.

RESEARCH OBJECTIVES AND PLAN

The major outcome of the research will be an inelastic design method for steel frame buildings subjected to wind loads. The methodology follows the ductile seismic design approach of controlled inelasticity in selected structural components and reduced design forces. Expected benefits include improved economy in design and system ductility for rare windstorms and high seismic events.

The basic research objectives are to establish loads, design prototype buildings, simulate nonlinear response, and evaluate reliability and risk. More specifically, the first objective is to identify steel buildings and develop the wind loads. This includes determining the duration of the wind loads and creating a set of archetype steel frame buildings. The second objective is to simulate nonlinear response with careful attention paid to structural damping and key modeling parameters. The third objective is to determine reliability and risk and develop guidelines for implementation of the inelastic design method.

Judy Liu, PhD, Research Editor of the AISC *Engineering Journal*, Professor, Oregon State University, School of Civil and Construction Engineering, Corvallis, Ore. Email: judy.liu@oregonstate.edu

The team is well into their research plan and is busy with design, simulation, and evaluation. In year 1, the research team determined the wind load characteristics needed for nonlinear response history analysis. The team also designed archetype steel frame buildings for further investigation in the study. Year 2 focused on identifying modeling parameters necessary for nonlinear response simulation of those archetype buildings subjected to wind loading. In year 3, the team has continued their design of prototype buildings while also conducting wind analyses. Wind load reliability and risk research will continue into year 4, followed by development of implementation guidelines.

IDENTIFY STEEL BUILDINGS AND WIND LOADS

First steps in the development of this inelastic method are to identify the steel frame buildings best suited for the design approach and to determine the wind loading for the study. A pilot study was first conducted to validate the proposed approach. This study also aided in the selection of the wind tunnel data and wind durations. An archetypal design space and prototype building designs were created.

Pilot Study

The pilot study was based on a structure with publicly available wind tunnel test data. The four-story, moment frame building is 78.5 ft long by 52.5 ft wide in plan and has a 13-ft story height, as shown in Figure 1. The lateral force-resisting system consists of a pair of 20-ft single-bay moment frames in each orthogonal direction. Ductile and conventional (i.e., nonductile) moment frame buildings were designed for a 110-mph wind. Exposure B was used to correlate to the suburban terrain used in the wind tunnel tests. Variable short duration and constant 4-hr wind events were considered.

Inelastic behavior was captured in the OpenSees (PEER, 2020) models of the prototype building. The ductile moment frame connections were based on the modified Ibarra-Medina-Krawinkler (IMK) model (Lignos and Krawinkler, 2011). The conventional moment frame buildings were assumed to have nonductile, flange-welded, pre-Northridge connections (ASCE, 2017; FEMA 2009, 2000) and were modeled using a Pinching4 model (Lowes et al.,

2004). For column plastic hinges, the modified IMK model was adjusted to account for the influence of axial compressive load on the hysteretic behavior of the column (Lignos et al., 2019).

Evaluation of the prototype building under wind loading included nonlinear static wind pushover and incremental dynamic analysis. The incremental dynamic analysis was based on records from wind tunnel tests conducted at Tokyo Polytechnic University (TPU) (Tamura, 2012). The wind direction changed in 15° increments from a cross-wind direction (0°) to an along-wind direction (90°). The lateral load pattern for the pushover analysis mimicked the wind profile in open terrain (Exposure C). Figure 2(a) shows velocity profiles for suburban (Exposure B) and open terrain (Exposure C) along with the target profile for the wind tunnel tests. The wind speed at a height z above ground level, $V(z)$, is normalized by the basic wind speed, V. V is a 3-s gust for ASCE 7-16 (ASCE, 2017) and a 10-min average wind speed for the Japanese standard. The equivalent full-scale duration of the sampled wind tunnel tests was less than 1 hr; those records were replayed until the total wind event was equal to 4 hr (1-hr ramp-up, 2 hr at the target wind speed, and 1-hr ramp-down) as recommended in the *Prestandard for Performance-Based Wind Design* (ASCE, 2019). Figure 2(b) shows the time history of the pressure coefficient, C_p.

The results showed improved performance for the ductile moment frame compared to the conventional moment frame. In the pushover analyses for the ductile moment frame, there is a modest increase (14%) in system over-strength but a significant increase (250%) in system ductility, μ, compared to the conventional moment frame. From the incremental dynamic analysis, plots of wind speed versus maximum story drift ratio were generated. Figure 3 shows a median collapse wind speed of 172 mph for the conventional moment frame and 192 mph for the ductile moment frame. Collapse margin ratios (CMRs) used velocity pressure in comparisons of the median collapse intensity to design strength-level intensity; the CMRs are 2.4 and 3.0, respectively, for the conventional and ductile moment frames. This is a dramatic increase (by 25%) in the CMR for the ductile moment frame. Fragility curves were also used to assess probability of collapse. The analysis showed that the ductile moment frame designed for 110 mph provides the same level of capacity as a conventional moment frame designed for 123 mph. In terms of wind pressure, this represents a 25% increase in capacity.

The pilot study validated the proposed design approach and helped to define important parameters for the study. The preliminary results showed that a ductile moment frame could be designed with a wind force reduction factor, R_w, of 1.25 and meet the reliability of a conventional moment frame. The researchers also concluded that the ductile moment frame is capable of meeting the reliability target of 0.01% recommended in the *Prestandard for Performance-Based Wind Design* (ASCE, 2019). To capture effects of windstorm duration, 30-min. and 4-hr wind load records would be used. The team chose to base the
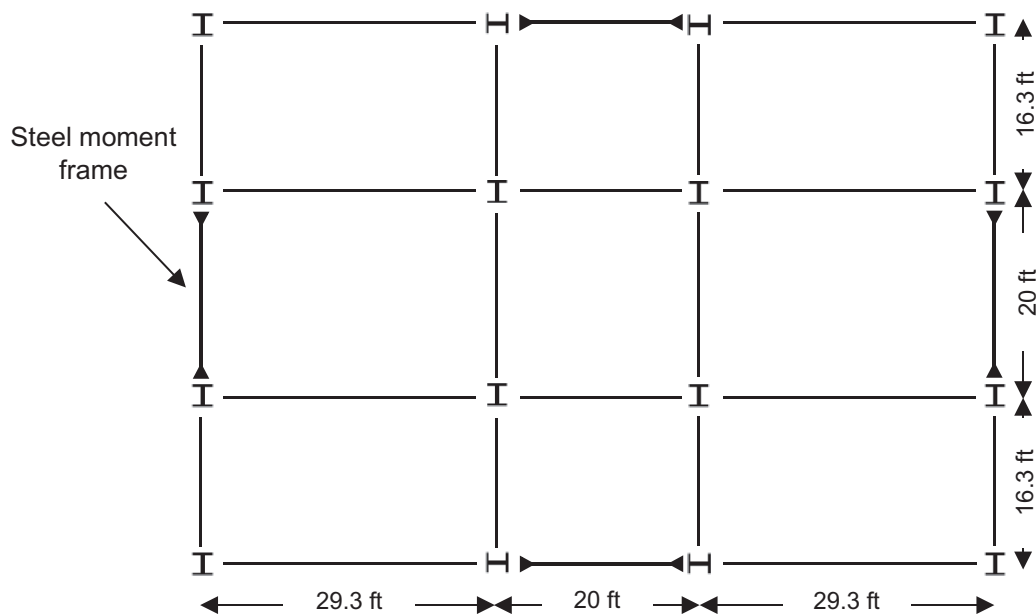

*Fig. 1. Pilot study prototype building plan.*

archetype buildings on a NIST database (NIST, 2017) instead of the TPU database to better correlate to the ASCE 7-16 exposure categories and utilize smaller increments in the wind direction angle.
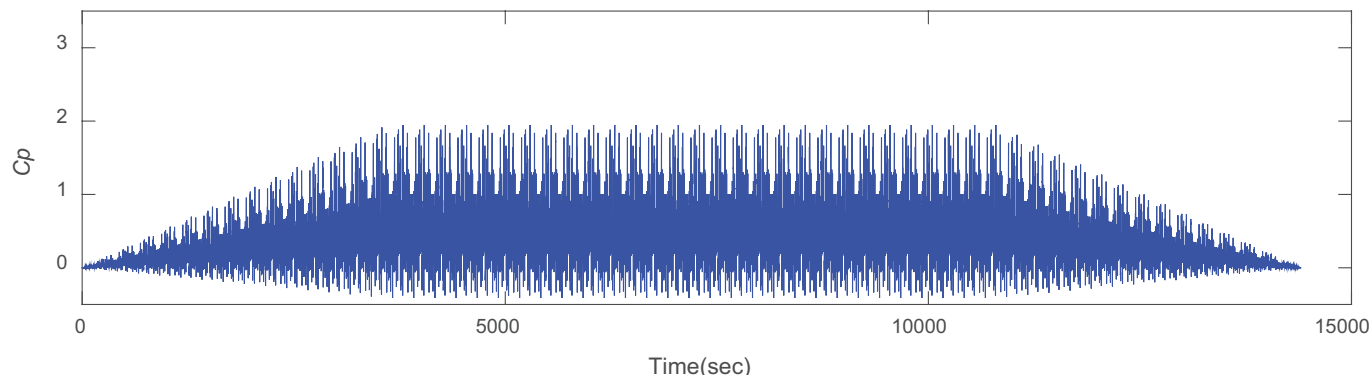
Archetype Steel Frame Buildings

The design space for the archetype steel frame buildings ranges from type of lateral force-resisting system to the wind speed. Again, the buildings were partly based on structures with publicly available wind tunnel test data. There are also similarities to buildings used to illustrate the *Seismic Design Manual* (AISC, 2018). The building plans have typical aspect ratios and are suited to different lateral force-resisting systems.

There are three floor plans and two types of buildings with a few different heights [Figure 4(a)]. The one- and three-story office buildings are 125×80 ft in plan [Figure 4(b)]. The first story is 15 ft tall and the upper stories are 12 ft tall. There is also a 46-story office building at $100 \times 150 \times 600$ ft. The one-story warehouse is 250×160 ft in plan with a 24-ft story height. Work to date has primarily been with the warehouse and the three-story office buildings.

Three types of lateral-force-resisting systems and levels of connection ductility are being evaluated. The lateral-force-resisting systems are steel moment frames (MF), steel-braced frames (BF), and composite plate shear walls filled with concrete (C-PSW/CF). Buildings have a pair of
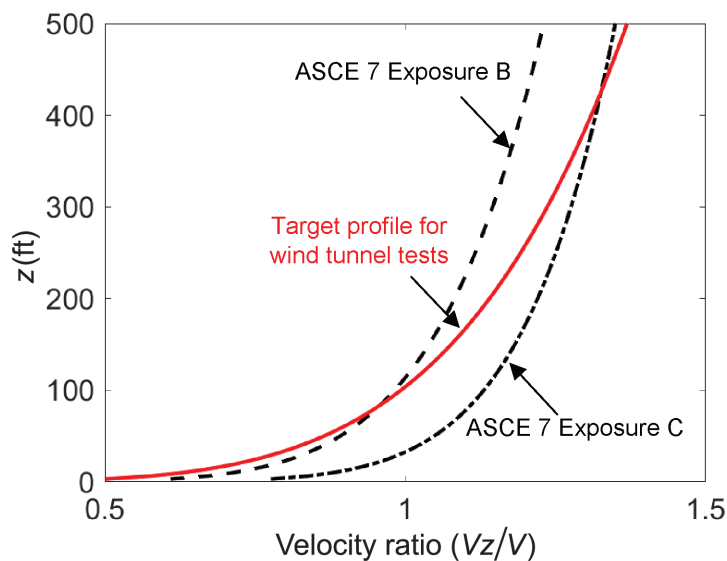
(a) Velocity profiles

(b) Pressure coefficient time history
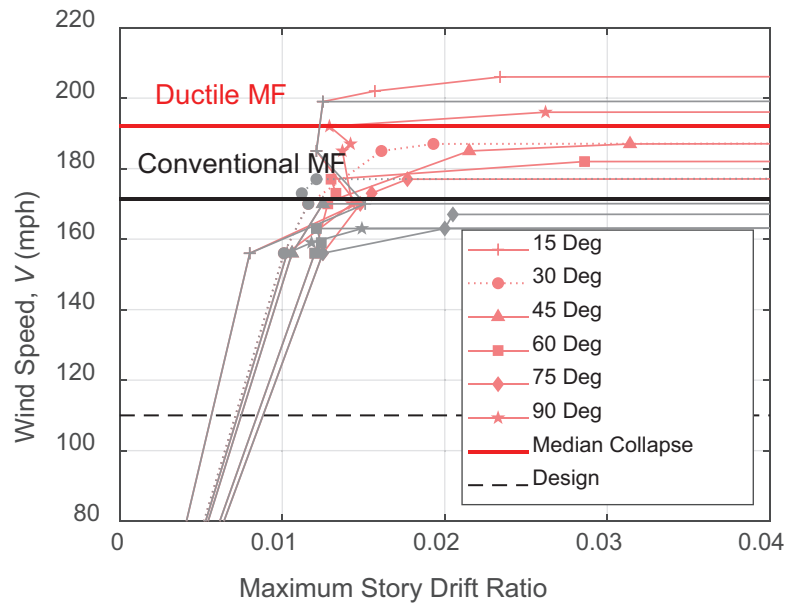
Fig. 2. Dynamic analysis of prototype building.

Fig. 3. Wind speed versus maximum story drift ratio for incremental dynamic analysis of prototype building.

(a) Schematics of archetype steel buildings

(b) One- and three-story office building floor plan showing moment frames only
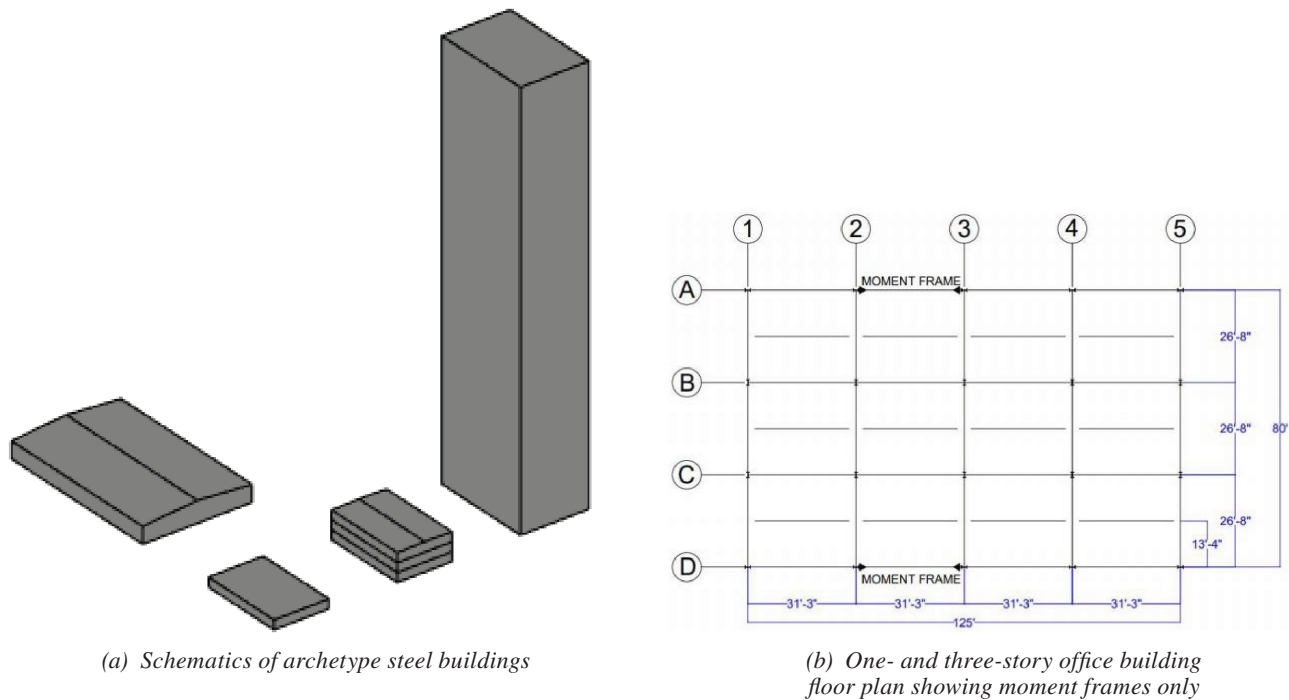
Fig. 4. Steel-framed building archetypes.

moment frames in one direction and a pair of braced frames or composite shear walls in the orthogonal direction. Each lateral force-resisting system is designed using the directional procedure (ASCE, 2017). Design work on the braced frames and composite shear walls is in progress.

Low-, medium-, and high-connection ductility are considered for the moment frame designs. The low, or nonductile, moment frame connections are fully restrained (FR) flange-welded beam-to-column connections designed following the 2016 AISC *Specification* (AISC, 2016a). Moderately ductile frames use welded unreinforced flange-welded web (WUF-W) connections that satisfy the *b/t* limits for moderately ductile sections as defined in the 2016 AISC *Seismic Provisions* (AISC, 2016b). Highly ductile frames also used welded unreinforced flange-welded web (WUF-W) connections but satisfy the *b/t* limits for highly ductile sections (AISC, 2016b, 2016c).

The archetype buildings are designed for gravity, snow, and wind loads. The strength-level wind speeds are 110, 127, 156, and 220 mph in Exposure C. A height/400 drift limit is checked using a service-level wind speed. Floor and roof live loads are 80 and 20 psf, respectively. The snow load is 20 psf; 85 psf and 68 psf floor and roof dead loads are used for the one- and three-story office buildings. The curtain wall weight is taken as 175 lb/ft.

The steel moment frame designs were governed by strength criteria. Even at the lowest wind speeds, drift limits were satisfied with members sized for the flexural or combined axial and flexural loading. Preliminary design of the three-story office building resulted in member sizes ranging from W12×19 to W18×55 for the beams and W14×26 to W24×76 for the columns. Preliminary member sizing was followed by panel zone shear and flange local bending checks. Additional details of the moment frame designs can be found in Gocke (2020) and Giles (2021) for the warehouse and office buildings, respectively.

The braced frame designs have also been governed by strength criteria. For the warehouse building, the square HSS members used for the diagonal braces were typically near 90% of their strength capacity. Member sizes ranged from HSS4×4×0.25 to HSS8×8×0.313. At higher wind speeds, local demands on the beams from the chevron braces required upsizing of the W-shapes for the limit state of flange local bending or local web yielding. Additional details of the braced frame designs can be found in Jacobs (2020).

SIMULATION OF NONLINEAR BEHAVIOR

Next steps were focused on simulation of the nonlinear behavior of the archetype buildings. In the proposed design approach, the premise is that controlled inelasticity and structural ductility allows for reduced design forces and improves system ductility. The control of inelasticity and ductility is at multiple levels: material response, local buckling, and selected components. Material ductility can be preserved by limiting the yield-to-ultimate tensile stress. Local buckling can be delayed by limiting the width-to-thickness ratio of section elements. Locations of inelasticity are limited to selected components. As such, the various sources of inelasticity are important for modeling and evaluation of the archetype buildings. The second year of the project addressed key modeling parameters for the steel systems. The steel moment frame and steel concentrically braced frame modeling are briefly highlighted here.

Steel Moment Frame Models

The sources of inelasticity in the steel moment frame models include ductile and nonductile beam plastic hinges. Figure 5(a) shows the ductile beam plastic hinge formation, again idealized using the modified IMK hysteresis model for the moment-rotation response. The cyclic degradation due to local buckling is considered directly in the rule-based hysteresis model. Parameters used in the model are based on statistical analysis of test data (Lignos and Krawinkler, 2011). Figure 5(b) shows the nonductile beam plastic hinge. For this model, a trilinear loading and unloading rule-based hysteresis model for reinforced concrete moment frames (Lowes et al., 2004) was adapted to capture fracture and pinching in the cyclic response. Parameters used for the nonductile beam plastic hinge were based on the behavior of pre-Northridge, flange-welded connections as evaluated by Lee and Foutch (2002) and others.

The column plastic hinges and panel zones are additional sources of inelasticity. The column plastic hinges are also idealized using the IMK hysteresis model. The modeling parameters account for the influence of axial compressive loading following Lignos et al. (2019). The cyclic shear force-deformations in the column panel zones are modeled using the Krawinkler model (Krawinkler, 1978). Additional details of the modeling can be found in Giles (2021).

Steel Concentrically Braced Frame Models

The steel concentrically braced frame models use distributed and concentrated plasticity. The beams, columns, and braces were modeled with nonlinear beam-column elements with fiber sections, as shown in Figure 6. The diagonal braces are subdivided into 10 elements with an out-of-plane initial imperfection or out-of-straightness. The imperfection was set to length/500 to achieve the predicted axial compressive strength calculated following the AISC *Specification* (AISC, 2016a). The fiber sections are used to capture local behaviors. The brace cross sections, for example, have four fibers across a side and four fibers through the thickness. The material modeling includes isotropic strain

hardening and fatigue based on work by Uriz (2005) for steel braced frames. Shear tab and gusset plate connections are modeled using nonlinear spring elements and parameters as defined in the literature (e.g., Hsiao et al., 2012).

Finite Element Analysis

The building responses are evaluated with cyclic nonlinear static pushover and nonlinear dynamic response history analysis. Cyclic nonlinear static pushover analysis is used to obtain system parameters such as overstrength and ductility. The lateral load pattern corresponds to the Exposure C wind profile and is applied with a displacement-control strategy at a roof node. Figure 7 shows a representative cyclic pushover curve. System overstrength for wind, Ω_{wind}, is defined as the maximum base shear force in the pushover analysis, F_{max}, divided by the wind design base shear force, F_{design}. The ductility, μ, is obtained by dividing the post-peak roof displacement at 80% of the peak load, $\Delta_{80\%}$,

(a) Ductile beam plastic hinges

(b) Nonductile beam plastic hinges
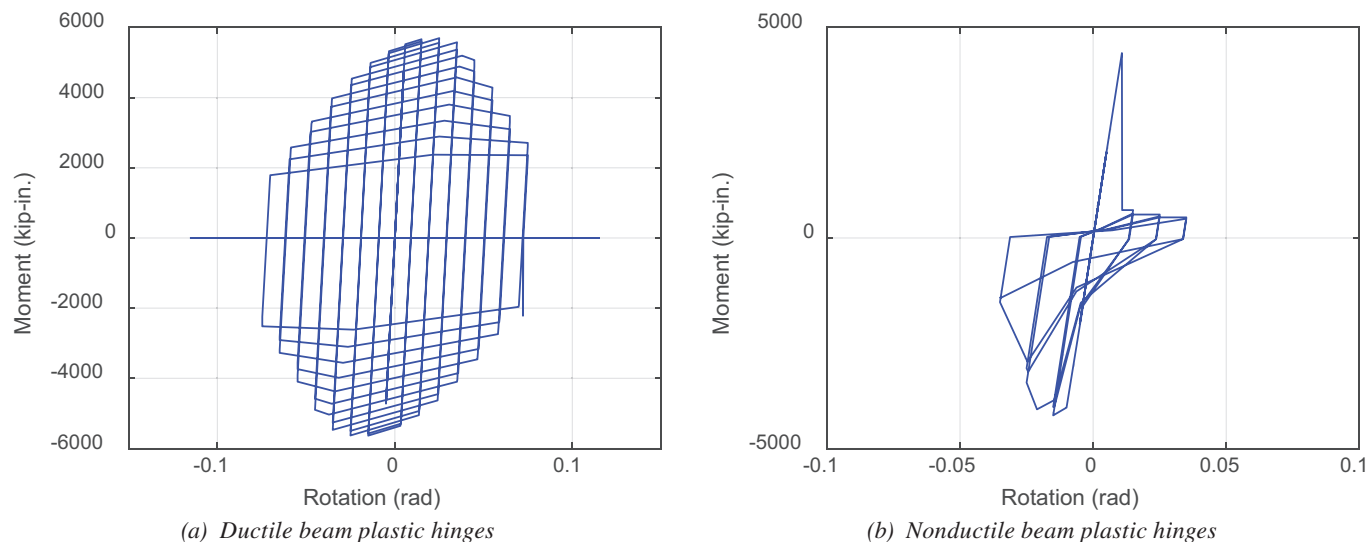
Fig. 5. Steel moment frame models.
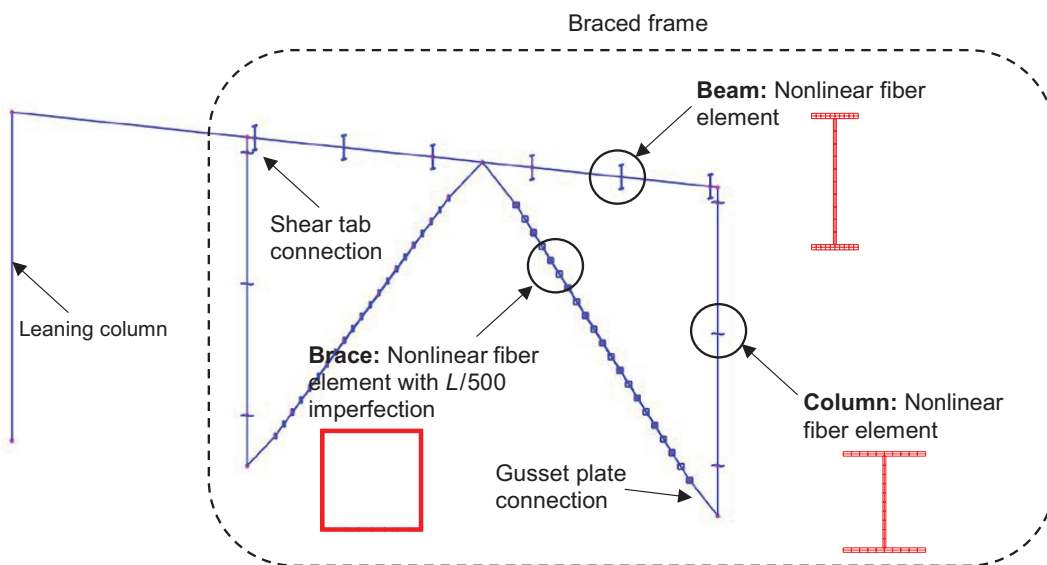
Fig. 6. Braced frame model with beam, brace, and column fiber elements.

by the effective yield displacement, Δ_y, (FEMA, 2009). Details on the cyclic nonlinear static pushover and nonlinear dynamic response history analysis can be found in Giles (2021).

Preliminary Results

Results from the cyclic nonlinear static pushover analyses have further validated the proposed approach. The effects of controlling inelasticity by limiting width-to-thickness ratios and by limiting inelasticity to selected components are investigated. For the braced frame in the warehouse building, the cyclic response for a conventional beam and non-slender brace, shown in Figure 8(a), is compared to a design with a strong beam and highly ductile brace, as shown in Figure 8(b). The system overstrength for wind, Ω_{wind}, increases from 2.5 to 10.6 for the strong beam and highly ductile brace. The ductility, μ, decreases from 40 to 23. These and other results demonstrate the effectiveness of connection ductility and controlling inelasticity

$$\Omega_{wind} = \frac{F_{max}}{F_{design}}$$
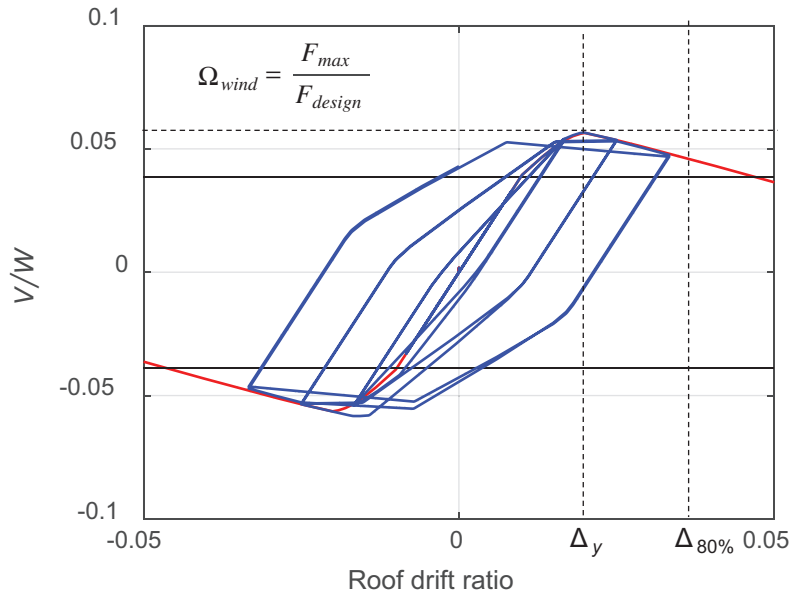
Fig. 7. Representative cyclic nonlinear static pushover analysis.

(a) Conventional beam and nonslender brace

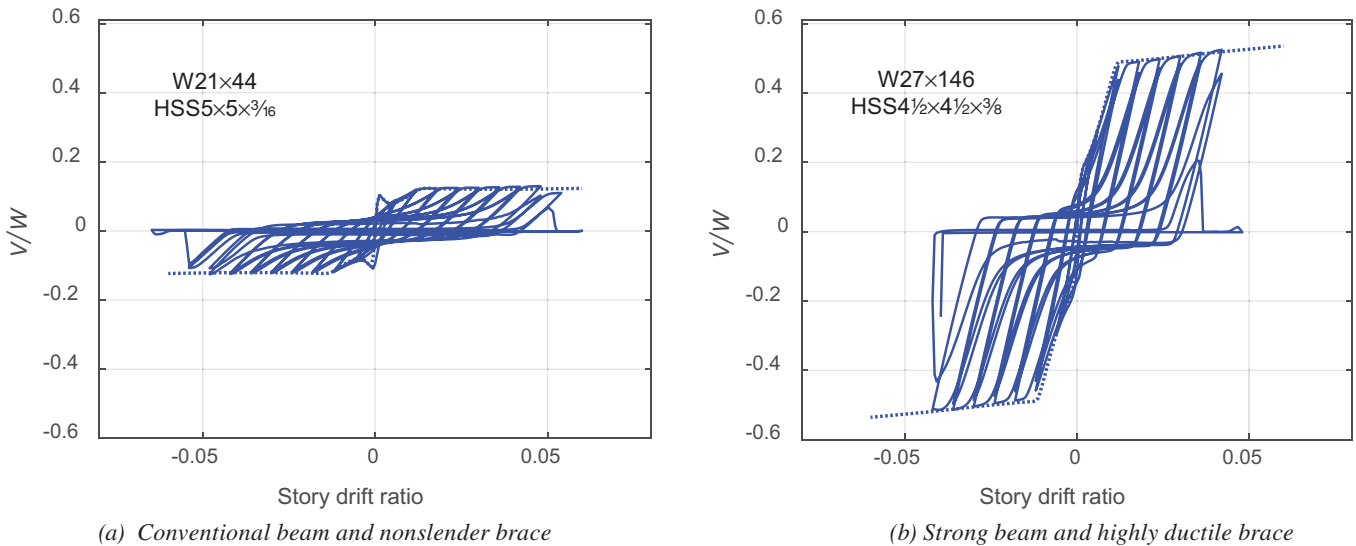*(b) Strong beam and highly ductile brace*

Fig. 8. Comparison of cyclic pushover response of braced frame in the warehouse building for 110-mph design.

for improving the predicted global strength of the system subjected to wind loads. The research team expects similar observations for the incremental dynamic analysis.

RELIABILITY AND RISK, FUTURE WORK, AND EXPECTED OUTCOMES

The third research objective centers around reliability and risk and forms the bulk of the future work. The main tasks are to provide a comprehensive analysis of reliability and risk for inelastic wind design and to develop guidelines for practical implementation of the proposed design approach. Designs of the concentrically braced frame (CBF) and composite plate shear wall filled with concrete (C-PSW/CF) systems will be finalized for the office buildings. The designs will be evaluated through cyclic nonlinear static pushover analysis, nonlinear dynamic response history analysis, and incremental dynamic analysis (Figure 9). Expected outcomes include recommendations for wind strength modification factors and best practices for controlling inelasticity.

ACKNOWLEDGMENTS

REFERENCES

AISC (2016a), *Specification for Structural Steel Buildings*, ANSI/AISC 360-16, American Institute of Steel Construction, Chicago, Ill.

AISC (2016b), *Seismic Provisions for Structural Steel Buildings*, ANSI/AISC 341-16, American Institute of Steel Construction, Chicago, Ill.

AISC (2016c), *Prequalified Connections for Special and Intermediate Steel Moment Frames for Seismic Applications*, including Supplement No. 2, ANSI/AISC 358, American Institute of Steel Construction, Chicago, Ill.

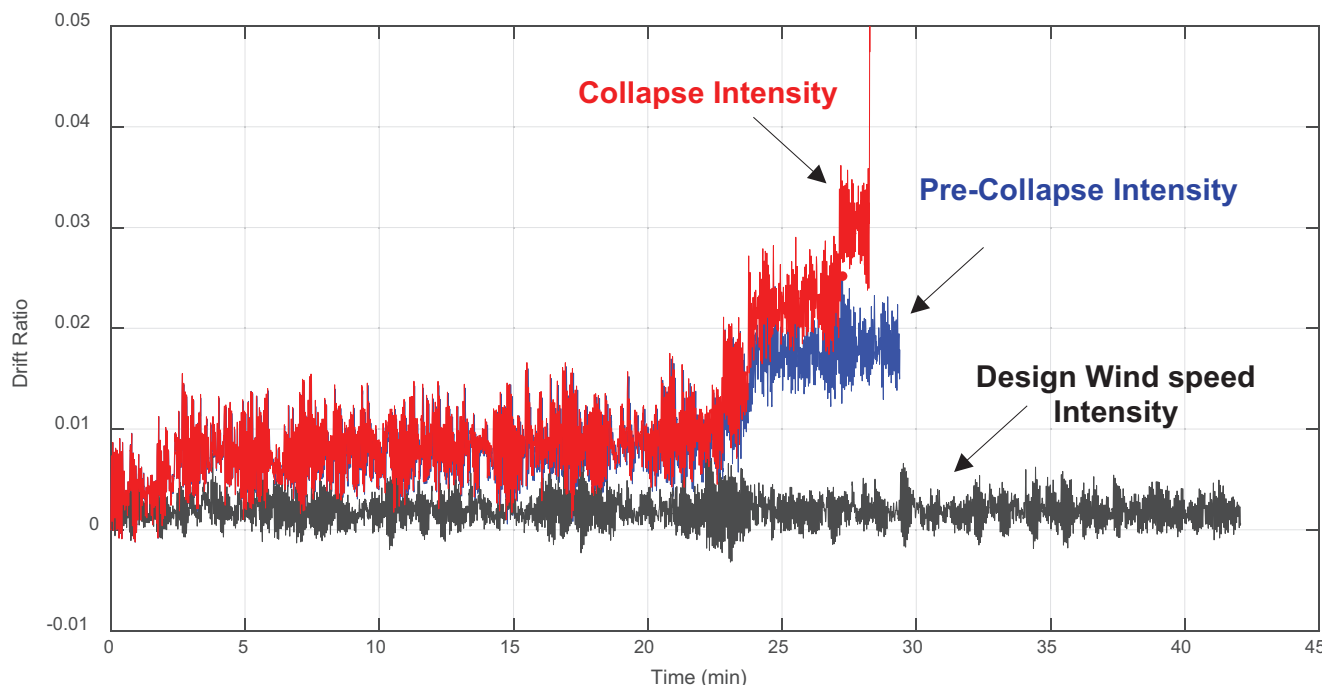AISC (2018), *Seismic Design Manual*, 3rd Ed., American Institute of Steel Construction, Chicago, Ill.

Fig. 9. Design, pre-collapse, and collapse intensity results from incremental dynamic analysis.

ASCE (2017), *Minimum Design Loads and Associated Criteria for Buildings and Other Structures*, ASCE/SEI 7-16, American Society of Civil Engineers, Reston, Va.

ASCE (2019), *Prestandard for Performance-Based Wind Design*, ASCE/SEI, American Society of Civil Engineers, Reston, Va.

FEMA (2000), *State of the Art on Systems Performance of Steel Moment Frames Subjected to Earthquake Ground Shaking*, FEMA 355C, prepared by the SAC Joint Venture, Federal Emergency Management Agency, Washington, D.C.

FEMA (2009), *Quantification of Building Seismic Performance Factors*, FEMA P-695, Federal Emergency Management Agency, Washington, D.C.

Giles, T.E. (2021), *Ductile Design and Predicted Inelastic Response of Steel Moment Frame Buildings for Extreme Wind Loads*, Master's Thesis, Department of Civil and Environmental Engineering, Brigham Young University, Provo, Utah, July.

Gocke, J.W. (2020), *Response Modification Factor for Inelastic Design of Low-Rise Steel Moment Frame Buildings Subjected to Extreme Wind Loads*, Master's Thesis, Department of Civil and Architectural Engineering, Brigham Young University, Provo, Utah, December.

Hsiao, P.-C., Lehman, D. E., and Roeder, C.W. (2012), "Improved Analytical Model for Special Concentrically Braced Frames," *Journal of Constructional Steel Research*, Vol. 73, pp. 80–94.

Jacobs, J. (2020). *Response Modification Factor for Inelastic Design of Low-Rise Steel Concentrically Inverted-V Braced Frame Buildings Subjected to Extreme Wind Loads*, Master's Thesis, Department of Civil and Architectural Engineering, Brigham Young University, Provo, Utah, December.

Krawinkler, H. (1978), "Shear in Beam-Column Joints in Seismic Design of Frames," *Engineering Journal*, Vol. 15, No. 3, pp. 82–91.

Lee, K. and Foutch, D.A. (2002), "Seismic Performance Evaluation Pre-Northridge Steel Frame Buildings with Brittle Connections," *Journal of Structural Engineering*, Vol. 128, No. 4, pp. 546–555.

Lignos, D.G. and Krawinkler, H. (2011), "Deterioration Modeling of Steel Components in Support of Collapse Prediction of Steel Moment Frames under Earthquake Loading," *Journal of Structural Engineering*, Vol. 137, No. 11, pp. 1,291–1,302.

Lignos, D.G., Hartloper, A.R., Elkady, A., and Deierlein, G.G. (2019), "Proposed Updates to the ASCE 41 Nonlinear Modeling Parameters for Wide-Flange Steel Columns in Support of Performance-Based Seismic Engineering," *Journal of Structural Engineering*, Vol. 145, No. 9, https://doi.org/10.1061/(ASCE)ST.1943-541X.0002353.

Lowes, L.N., Mitra, N., and Altoonash, A. (2004), *A Beam-Column Joint Model for Simulating the Earthquake Response of Reinforced Concrete Frames*, PEER Report 2003/10, Pacific Earthquake Engineering Research Center, University of California, Berkeley, Calif.

NIST (2017), *NIST Aerodynamic Database*, https://www.nist.gov/el/materials-and-structural-systems-division-73100/nist-aerodynamic-database, August.

PEER (2020), Open Systems for Earthquake Engineering Simulation (OpenSees), version 3.2.2. PEER, University of California, Berkeley, Calif.

Tamura, Y. (2012), "Aerodynamic Database of Low-Rise Buildings," http://www.wind.arch.t-kougei.ac.jp/info_center/windpressure/lowrise/mainpage.html, March.

Uriz, P. (2005), *Towards Earthquake Resistant Design of Concentrically Braced Steel Structures*. Ph.D. Dissertation, Structural Engineering, Mechanics, and Materials, Civil and Environmental Engineering, University of California, Berkeley, Calif.

Guide for Authors

Scope   *Engineering Journal* is dedicated to the improvement and advancement of steel construction. Its pages are open to all who wish to report on new developments or techniques in steel design, research, the design and/or construction of new projects, steel fabrication methods, or new products of significance to the uses of steel in construction. Only original papers should be submitted.

General   Papers intended for publication should be submitted by email Margaret Matthew, editor, at **matthew@aisc.org**.

The articles published in the *Engineering Journal* undergo peer review before publication for (1) originality of contribution; (2) technical value to the steel construction community; (3) proper credit to others working in the same area; (4) prior publication of the material; and (5) justification of the conclusion based on the report.

All papers within the scope outlined above will be reviewed by engineers selected from among AISC, industry, design firms, and universities. The standard review process includes outside review by an average of three reviewers, who are experts in their respective technical area, and volunteers in the program. Papers not accepted will not be returned to the author. Published papers become the property of the American Institute of Steel Construction and are protected by appropriate copyrights. No proofs will be sent to authors. Each author receives three copies of the issue in which his contribution appears.

Manuscripts   Manuscripts must be provided in Microsoft Word format. Include a PDF with your submittal so we may verify fonts, equations and figures. View our complete author guidelines at **aisc.org/ej**.